getech

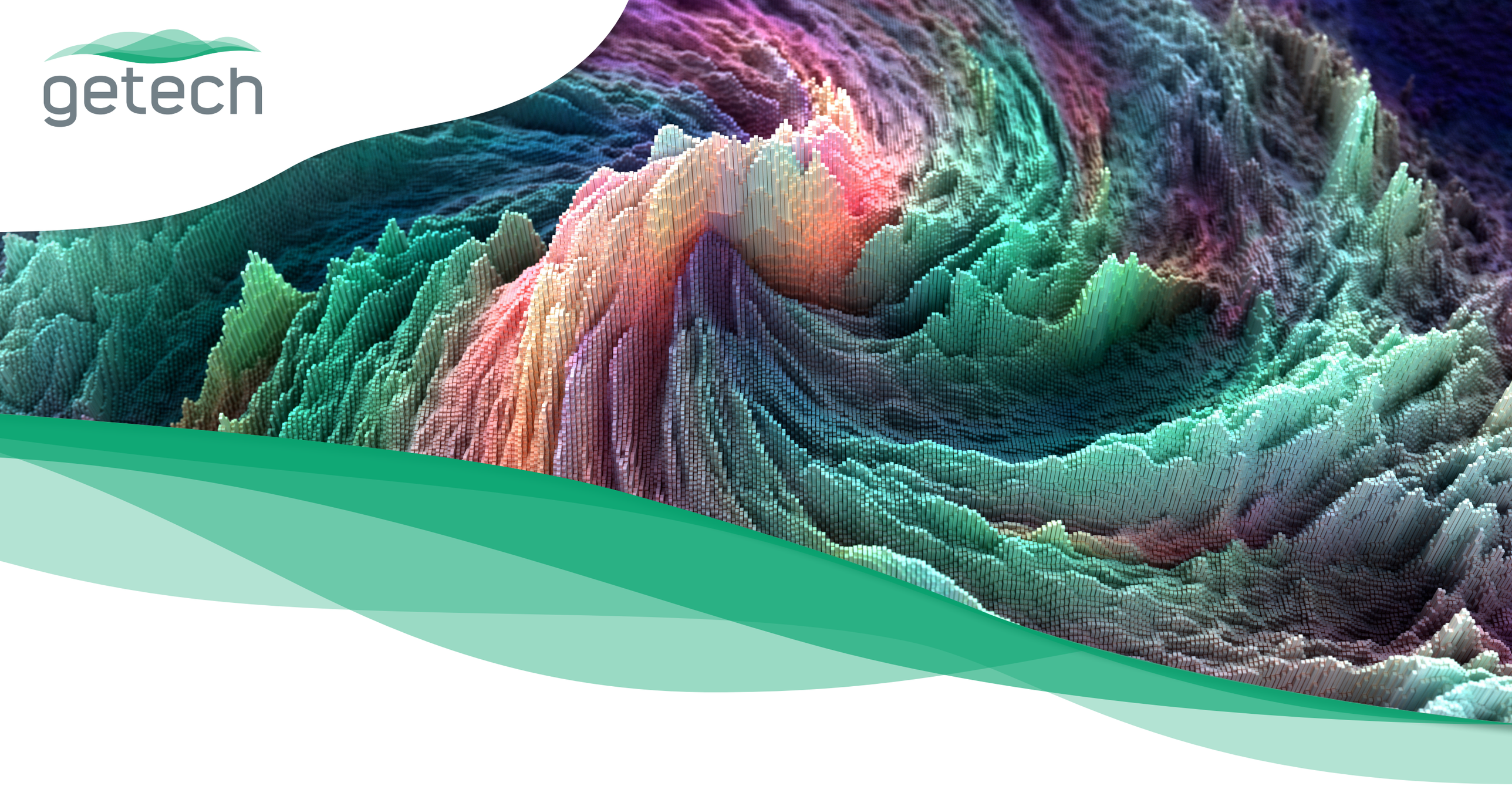

Thermal Mapping Updates 2021

Thermal Mapping

1. Executive Summary

Temperature and heat flow are key parameters for understanding the potential for source rock maturation in sedimentary basins. Knowledge of the thermal structure of the lithosphere in both a regional and local context can provide important constraints for modelling basin evolution through time.

The Globe 2021 Thermal Mapping Product represents the progress made at the end of the fourth year of the current programme of work. It includes updated grids of the depth to the Curie isotherm, predicted temperature at depth below surface and several relevant modelling input parameters. The product also includes a global heat flow compilation that has been used to generate a global grid of surface heat flow estimates, as well as providing important constraints on near-surface thermal properties, such as thermal conductivity and radiogenic heat production. The 2021 product release also includes substantial progress in our understanding and implementation of machine learning techniques to estimate surface heat flow from various geophysical and geological datasets.

This report is an accompaniment to the data and grids that are provided with the Thermal Mapping Product; it builds upon detailed reports from previous product releases and provides updates to data quality assessments and modelling methods that have been used throughout 2021.

1.1. Report structure

- Section 2: Data Types, Approaches and Curie Temperature Depth
- Section 3: Curie Temperature Depth from Surface Heat flow
- Section 4: Curie Temperature Depth from Terrestrial Magnetic Data
- Section 5: Curie Temperature Depth from Satellite Magnetic Data
- Section 6: Integration of Curie Temperature Depth Estimates and Temperature-Depth Prediction
- Section 7: Estimating Moho Temperature from Upper Mantle Density Inversion
- Section 8: Predicting Surface Heat Flow Using Machine Learning Techniques
- Section 9: Deliverables
- Section 10: References

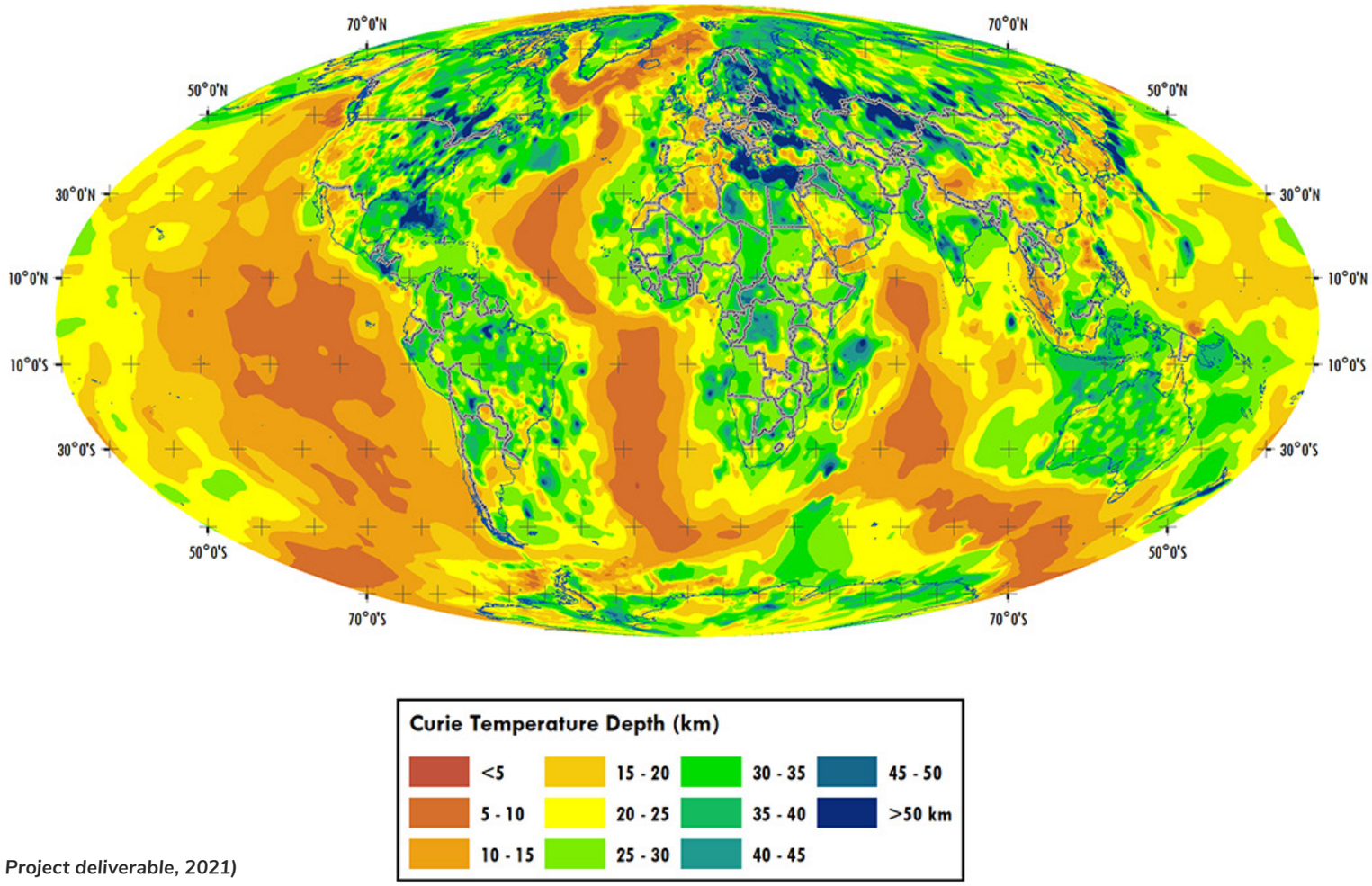

Figure 1.1.1: Getech's integrated Curie Temperature Depth grid (Thermal Mapping Project deliverable, 2021)

2. Data Types, Approaches and Curie Temperature Depth

Getech's approaches to mapping temperatures at depth are based on 1D, steady state models, for which we project up or down the geotherm from different reference surfaces or isotherms. For example, surface heat measurements can be used to project down the geotherm to any given depth or temperature within a physical model of the lithosphere. Magnetic methods can be used to estimate Curie Temperature Depth (CTD), the depth at which magnetic minerals lose their magnetisation due to temperature; this is ~580°C for magnetite, the dominant magnetic mineral in Earth's crust.

Getech integrate CTD estimates from both surface heat flow and magnetic approaches and project back up along the geotherm to predict temperature at various depths within the crust.

This general approach may also be extended to greater depths, where reference isotherms or isotherm depths may be constrained by upper mantle physical properties and Lithosphere-Asthenosphere Boundary (LAB) depth estimates.

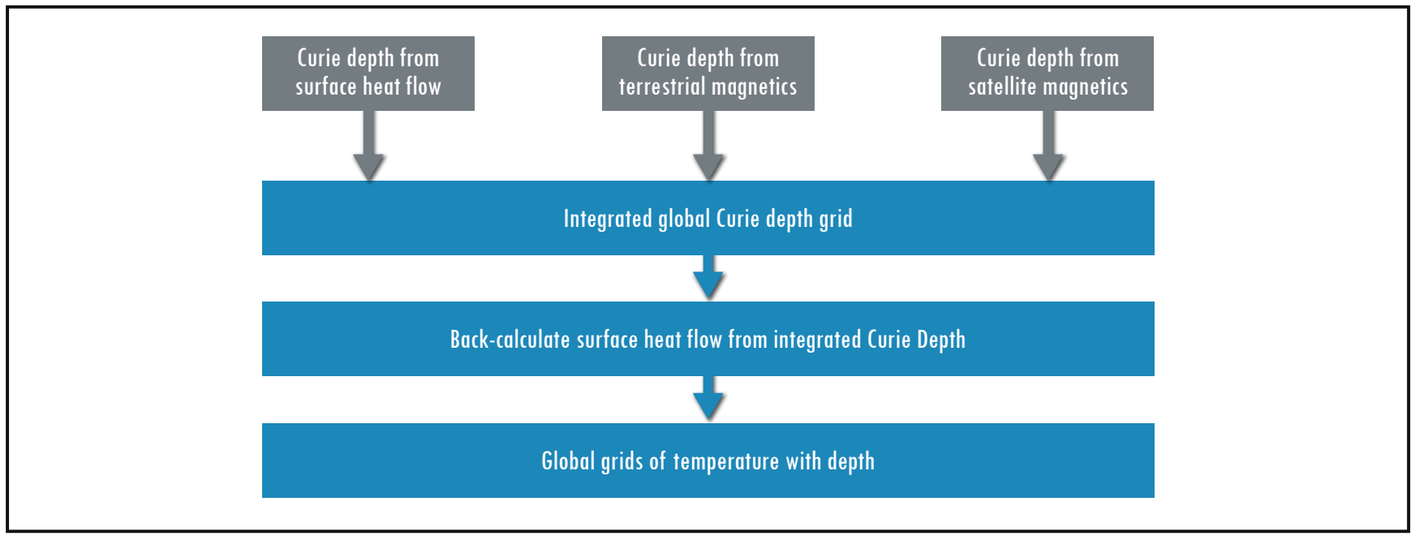

Figure 2.1.1: A generalised workflow for Getech's Thermal Mapping Project

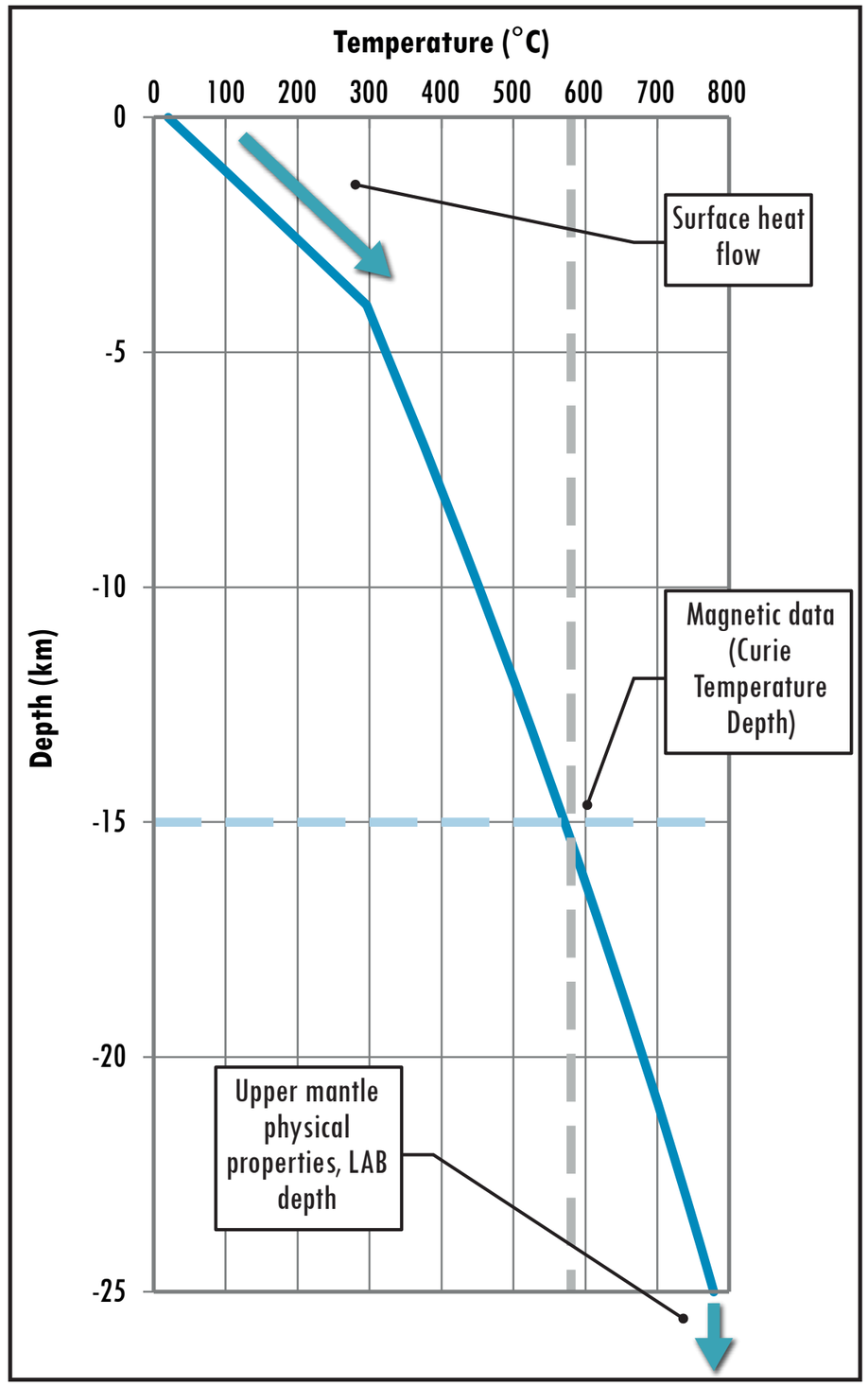

Figure 2.1.2 (Right): Different data types provide thermal constraint at different depth. We can project up or down the geotherm accordingly, using 1D, steady state models

3. Estimating Curie Depth from Surface Heat Flow Data

3.1. Methodology review

Prediction of CTD and temperature/heat flow at depth from surface heat flow is based on standard steady-state, 1D heat flow equations (e.g. Salem et al., 2014):

$$T(z) = T_0 - \frac{A}{2K}z^2 + \frac{Q_0}{K}z$$

These equations are used alongside a simple three-layer model that comprises an upper sedimentary layer, a crustal layer and a mantle layer. Thermal conductivity (K) and heat production(A) values are assigned to each layer and the surface heat flow (Q0) is constrained by Getech's Global Heat Flow Data compilation (Figure 3.1.1).

3.1.1 Thermal conductivity

Thermal conductivities for each model layer have been assigned following analysis of measurements within Getech's Global Heat Flow Database and literature review:

- Sediment: 2 $Wm^{-1}K^{-1}$ (onshore), 0.95 $Wm^{-1}K^{-1}$ (offshore, assumes unconsolidated sediments)
- Crust: 2.5 $Wm^{-1}K^{-1}$
- Mantle: 3 $Wm^{-1}K^{-1}$

Thermal conductivity is adjusted for temperature according to the empirical relationship of Sekiguchi (1984)

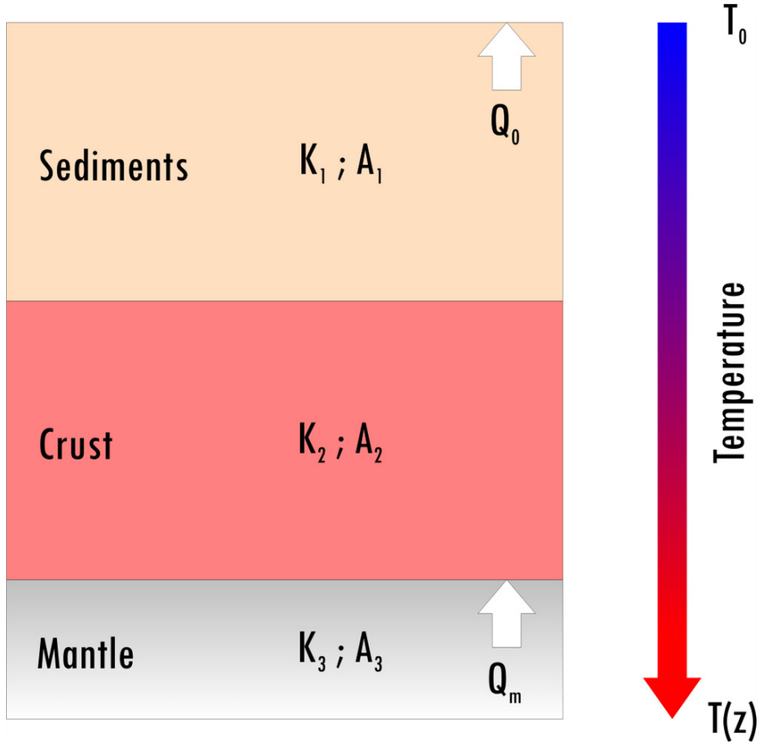

Figure 3.1.1: CTD and temperature-depth prediction from surface heat flow uses a three-layer physical model.

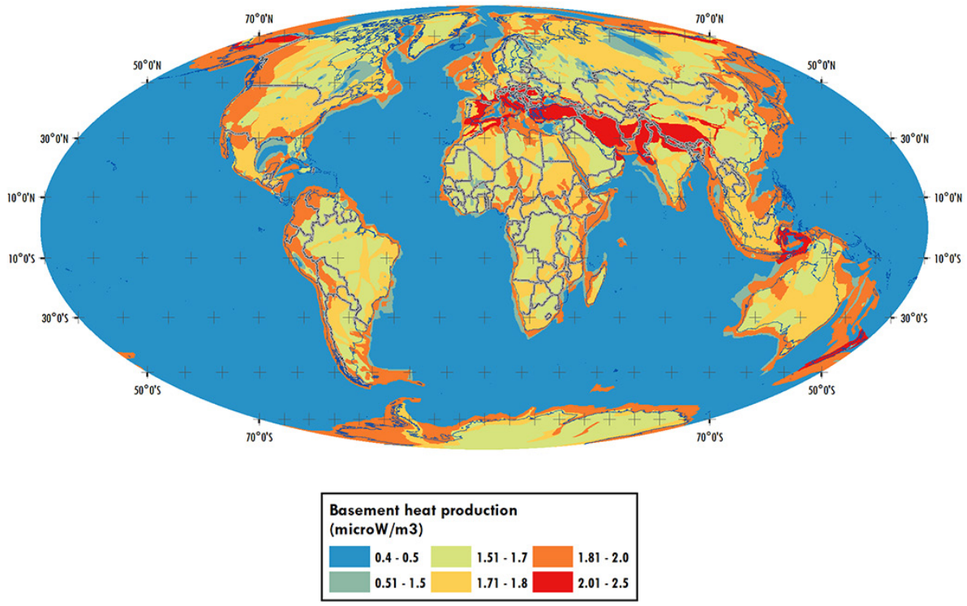

Figure 3.1.2: Basement heat production

3.1.2 Radiogenic heat production

Radiogenic heat production for sediments is assigned as 1.2 μW m^{-3}, after Hamza & Vieira (2012).

Radiogenic heat production for basement is based primarily on tectonic setting (Table 3.1.1, Figure 3.1.2).

Getech use the empirical relationship of Jaupart et al. (2016) to allow basement heat production to decay from basement depth to a depth of 10 km below basement, according to:

$$A = A_0 e^{-\frac{Z}{D}}$$

where D is 10 km. Below 10 km depth, crustal heat production is fixed at 0.25 μW m^{-3}.

In some areas where surface heat flow is low, standard heat production values for the sediments and crust are replaced with values that are calculated from crustal thickness and surface heat flow, such that mantle heat flow is 15 mW m^{-2}. This ensures that model-predicted temperature-depth converges to a value for CTD.

The mantle is assumed to have no heat production.

Tectonic Setting	Equivalent Basement A (μW m^{-3})
Craton	1.7
Mobile belt	1.8
Continent-continent collision	2.5
Ocean-continent collision	2
Attenuated continental	2
Transitional	1.5
Ocean-ocean collision	0.5
Oceanic	0.5

Table 3.1.1: Radiogenic heat production for basement, by tectonic setting

3.2. Onshore heat flow database development

For Globe 2021, Getech began the process of locating source publications for the Global Heat Flow database and evaluating them to assess measurement quality.

We have prioritised publications that contain high heat flow measurements, particularly those that conflict with nearby measurements from different sources.

We have located and reviewed 150 source publications and used these summaries to categorise 754 database records as follows:

- Survey contains some anomalous heat flow values (although mean heat flow for the survey is sensible) (108 records)
- Anomalously high heat flow that is unaccounted for (107 records)
- Anomalously high heat flow that may be attributed to the geological setting (408 records)
- Values differ from the primary source due to unit conversion (131 records)

An onshore subset of the Global Heat Flow Database has been derived to underpin a global surface heat flow grid (Figure 3.2.1); data selection is based on several criteria, including:

- Exclusion of anomalously high heat flow measurements (using categorisation above) and an upper limit of 200 mW m^{-2}.
- Identification and exclusion of statistically high or low values within low and high clusters, respectively (using ArcGIS Optimized Outlier Analysis tool).

The onshore database subset has been merged with selected offshore surface heat flow data (Section 3.3) and spatially averaged within 0.25° cells to generate an 'Interpreted' point dataset as input to final grid interpolation (Figure 3.5.1)

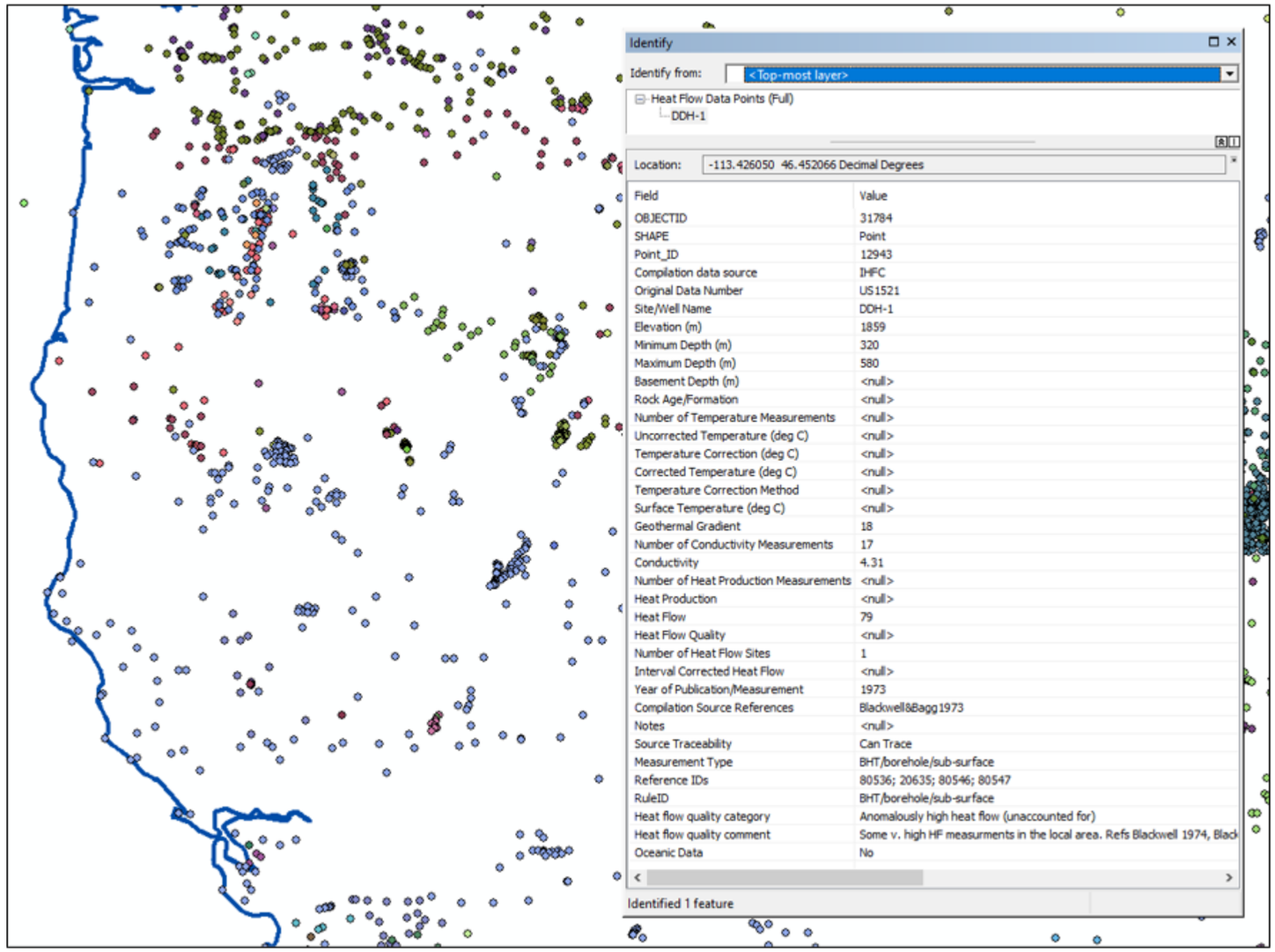

Figure 3.2.1: A screen capture example from the western United States (Oregon, northern California) of the onshore heat flow database and its attribution, symbolised according to source publication.

3.3. Prediction of CTD from Offshore heat flow data

3.3.1. Offshore heat flow data selection

Getech have reviewed the offshore surface heat flow data coverage within the Global Heat Flow Database and applied data selection criteria to input data for a final surface heat flow grid.

Data selection criteria follow the approach of Hasterok et al. (2011) and aim to filter out the effect of hydrothermal circulation through sediments and the influence of basement highs and exposures on lateral heat flow.

The following data are excluded for the offshore data coverage:

1. Data flagged in the IHFC database (which contributes to Getech's Global database) as representing regions with high transient thermal conditions related to lateral fluid flow, unstable bottom water temperature or sedimentary inversion (e.g. Landslides)
2. Data within 0.5° of the nearest seamount or LIP
3. Data with sediment less than 400 m thickness
4. Data where surface heat flow differs from heat flow predicted by the GDH1 thermal plate model (Stein & Stein, 1992) by more than 500 mW m^{-2}

To verify an improved offshore dataset, surface heat flow measurements have been assigned to 2.5 Myr age bins, using Getech's oceanic age grid. Mean-normalised standard deviation of heat flow for each age bin has been plotted with and without applying the above data exclusion criteria, with Criterion 4 being applied separately (Figure 3.3.1). Application of Criteria 1-4 to the offshore heat flow data set results in the greatest reduction in the standard deviation for all age bins. This is particularly significant for younger oceanic crust where the influence of rougher basement topography and hydrothermal circulation is greater.

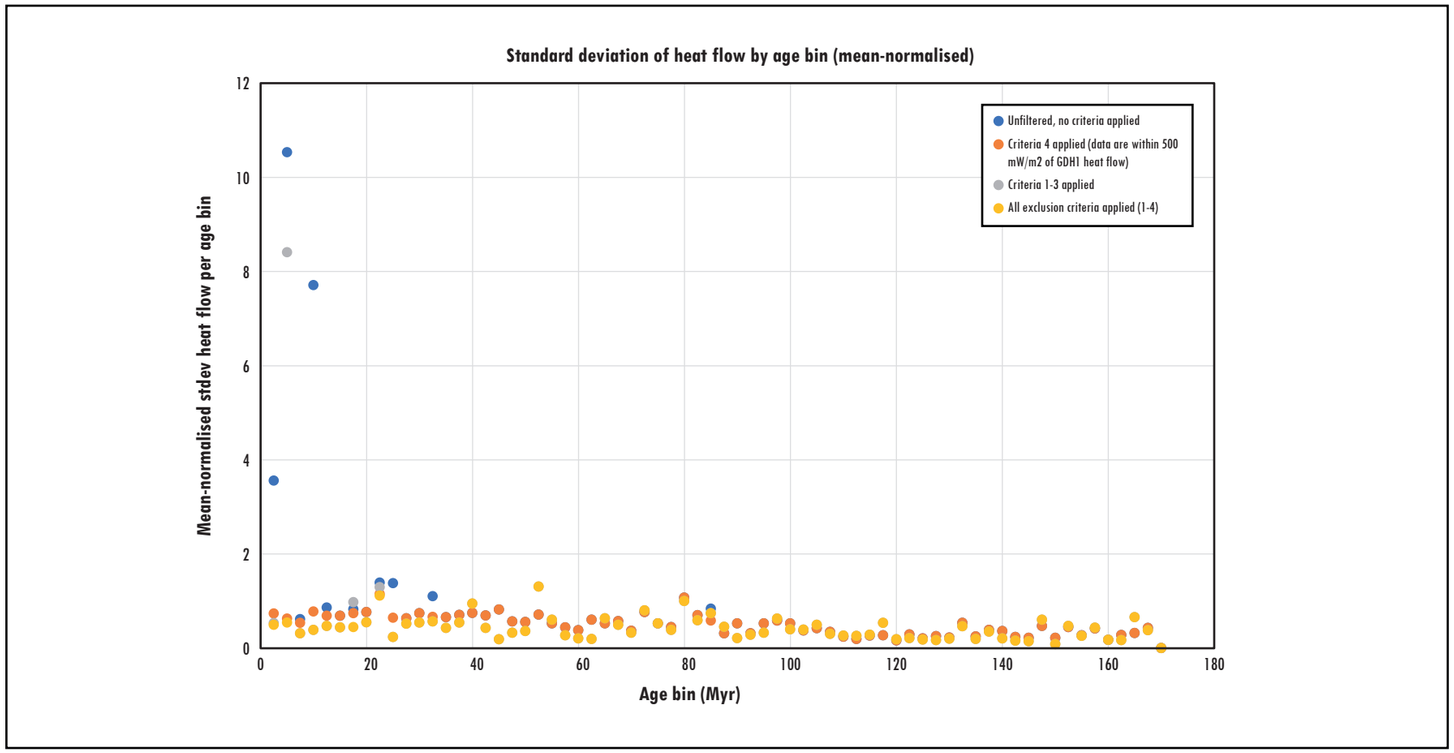

Figure 3.3.1: ***Mean-normalised standard deviation of heat flow by 2.5 My age bins. Blue: No heat flow data exclusion criteria applied; Orange: Criterion 4 only applied; Grey: Criteria 1-3 applied; yellow: Criteria 1-4 applied***

3.3.2. The influence of sedimentation rate on surface heat flow

- Sedimentation affects the heat flow observed at the surface. Deposition of cold (surface temperature) sediments pushes existing isotherms further below the surface and reduces the geothermal gradient, thus reducing the surface heat flow (Figure 3.3.2.1). Over time, the sediments act as a blanket to reduce surface heat flow, but the remaining thermal gradient at depth will act to limit the reduction in surface heat flow (Figure 3.3.2.2). If the sediments contain radiogenic material (e.g., clay), this will act as a near surface heat source and the reduction in surface heat flow will be lessened or the heat flow may possibly increase. When sedimentation ceases, heat flow will increase again.
- The impact of surface heat flow due to a simple sedimentation model has been described by equations presented by Jaupart & Mareschal (2011) and by Von Herzen & Uyeda (1963). These equations are expressed differently, but their results are the same; the expression of Von Herzen & Uyeda (1963) is given as it includes heat production. Simplified for surface heat flow we have:
- $$Q_0 = K\left\{a + \frac{1}{2U}\left(aU - \frac{\kappa A}{K}\right)\left[\left(1 + \frac{U^2 t}{\kappa}\right) erfc(X) - erfc(Y) + X\left(-\frac{\partial}{\partial X} erf(X)\right) - Y\left(-\frac{\partial}{\partial Y} erf(Y)\right)\right]\right\}$$
- where $X = \frac{Ut}{2(\kappa t)^{\frac{1}{2}}}$
- and $Y = \frac{-Ut}{2(\kappa t)^{\frac{1}{2}}}$
- *erf* is the error function and *erfc* is the complimentary error function
- *U* is the rate of sedimentation over time t
- a is the initial geothermal gradient
- A is the radiogenic heat production of the sediments
- K and κ are the conductivity and diffusivity of the sediments
- and $\kappa = \frac{K}{\rho C_p}$
- where ρ and C_p are the density and specific heat capacity of the sediments
- At the start of sedimentation, surface heat flow reduces rapidly, but this reduction lessens through the period of sedimentation (Figure 3.3.2.3). If the sediments include radiogenic material, the reduction in heat flow is lower. Despite the limitations of the model (no sediment compaction, constant sedimentation rate), this model can be used to adjust (increase) offshore surface heat flow values.
- In our model, the duration of sedimentation is the crustal age in oceanic areas and the age of adjacent ocean crust on continental margins. Sedimentation rate is taken as the distance between sea-bed and basement divided by this age. Radiogenic heat production is assumed zero and diffusivity of the sediments is taken as 0.1×10^{-6} m^2 s^{-1}.
- This value of diffusivity and the overall validity of the process is assessed by comparing adjusted heat flow with the GDH1 model following the approach of Hasterok et al. (2011).
- Over the whole globe, the application of this adjustment would result in a mean heat flow increase of 11%.

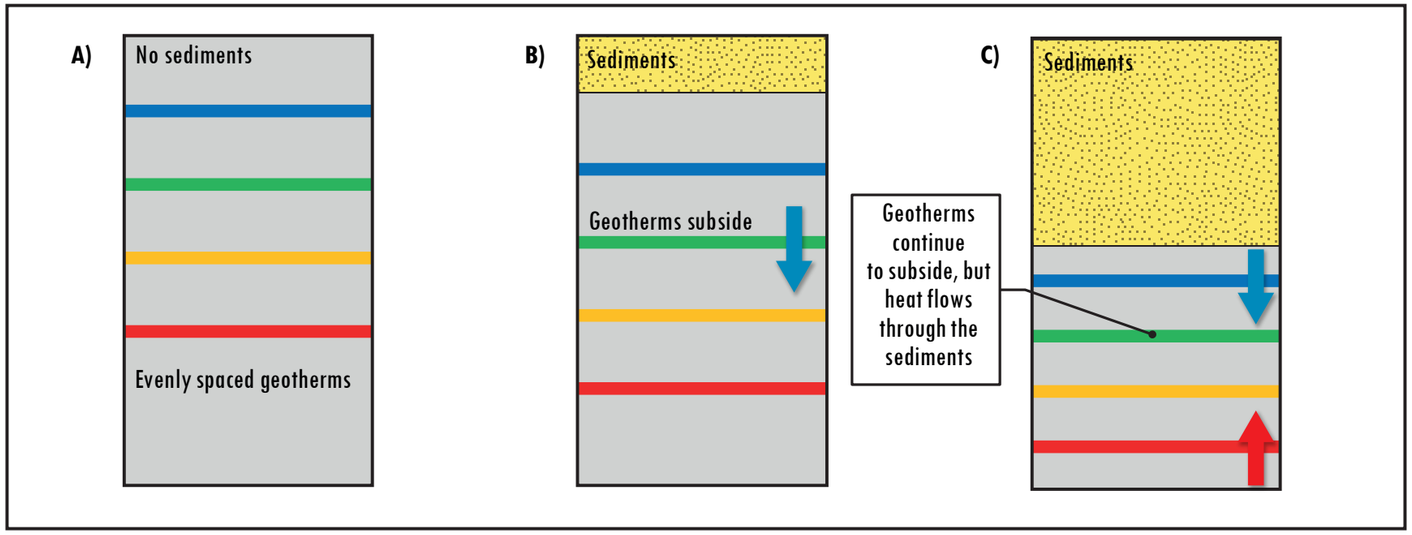

Figure 3.3.2.1: Effects of sedimentation on geotherms: a) no sediments, linear geotherm; b) sedimentation pushes isotherms down and reduces geothermal gradient; c) temperatures at depth tend to counteract subsidence effects.

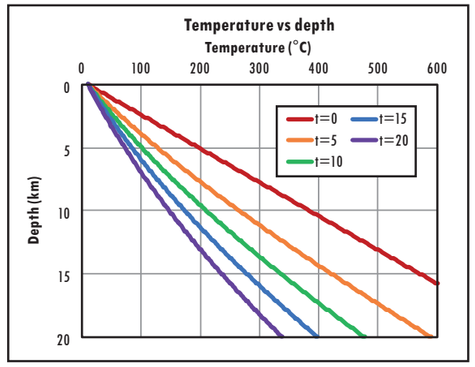

Figure 3.3.2.2: Example of how geotherms change through time from 0 to 20 Myr with constant sedimentation. Note that the rate of change of gradient reduces through time and the geotherms curve as the situation moves towards stability.

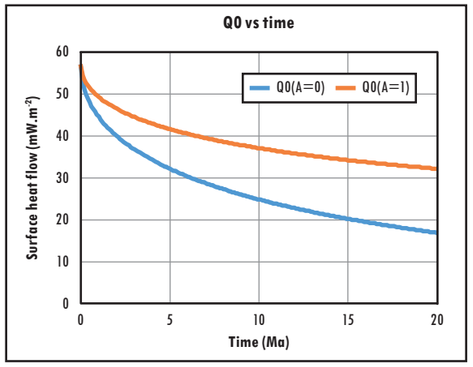

Figure 3.3.2.3: Example of surface heat flow through time for sediments with (orange) and without (blue) radiogenic heat production.

3.3.3. The influence of sediment compaction on surface heat flow

- Shallow marine sediments are observed to have very low thermal conductivity (often 0.8-1.1 $Wm^{-1}K^{-1}$) which increases with depth such that consolidated sedimentary rocks have values ~2.0 $Wm^{-1}K^{-1}$. Low conductivity at surface is related to high porosity, which is commonly modelled as decaying exponentially with depth (Figure 3.3.3.1).
- Given the low conductivity of water, conductivity increases with depth - based on a geometric mean of the conductivities of rock material and water (Figure 3.3.3.2). Average conductivity down to each depth (Av cond) gives a good indication of the thermal effect of the upper layers and the same average can be calculated for a simplified model (model k, Av model k). The illustrated model with conductivity 1.1 $Wm^{-1}K^{-1}$ down to 2 km and 2.0 $Wm^{-1}K^{-1}$ below 2 km gives a generally reasonable fit to the average conductivity based on the porosity curve.
- The geotherm for this model (TmodDep) is compared in Figure 3.3.3.3 with the geotherm based on the porosity model (Tdepth) and the two match well. Below 2 km, the temperature is ~40 °C hotter than for the constant conductivity model (Tkconst) for surface heat flow of 50 mWm^{-2}. Thus, this model can be approximately accounted for with a temperature shift (°C) of:
- $\Delta T \approx 40\ Q_0/50$ for depth (z) greater than 2 km, and:
- $\Delta T \approx 40\ Q_0/50\ z/2$ for depth (z in km) less than 2 km, where Q_0 is heat flow in mW m^{-2}.
- This model was not applied in the final deliverables due to uncertainties in the most appropriate porosity model.

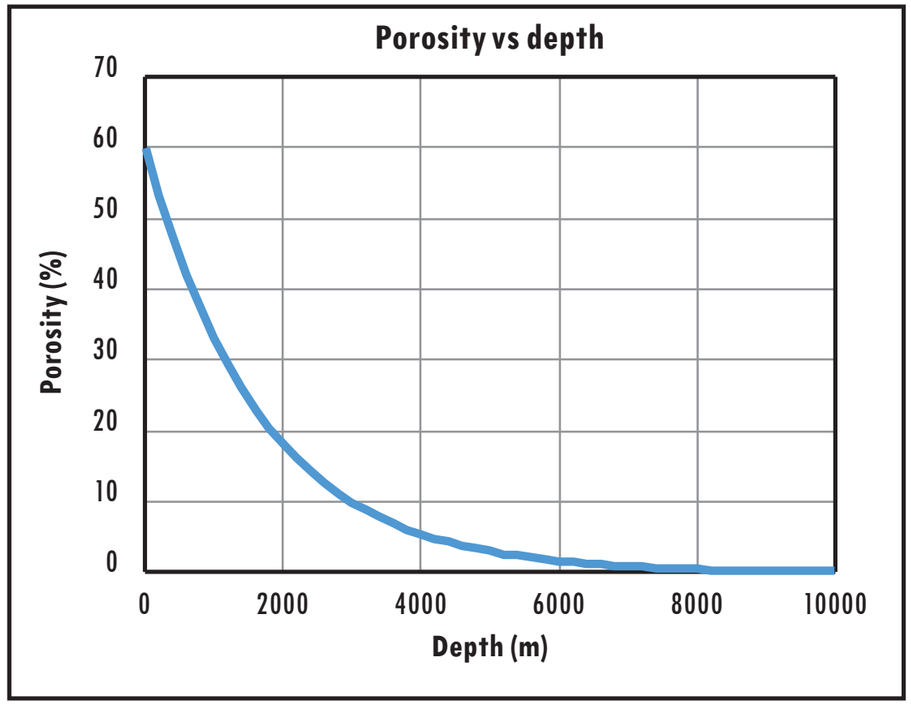

Figure 3.3.3.1: Typical porosity-depth curve.

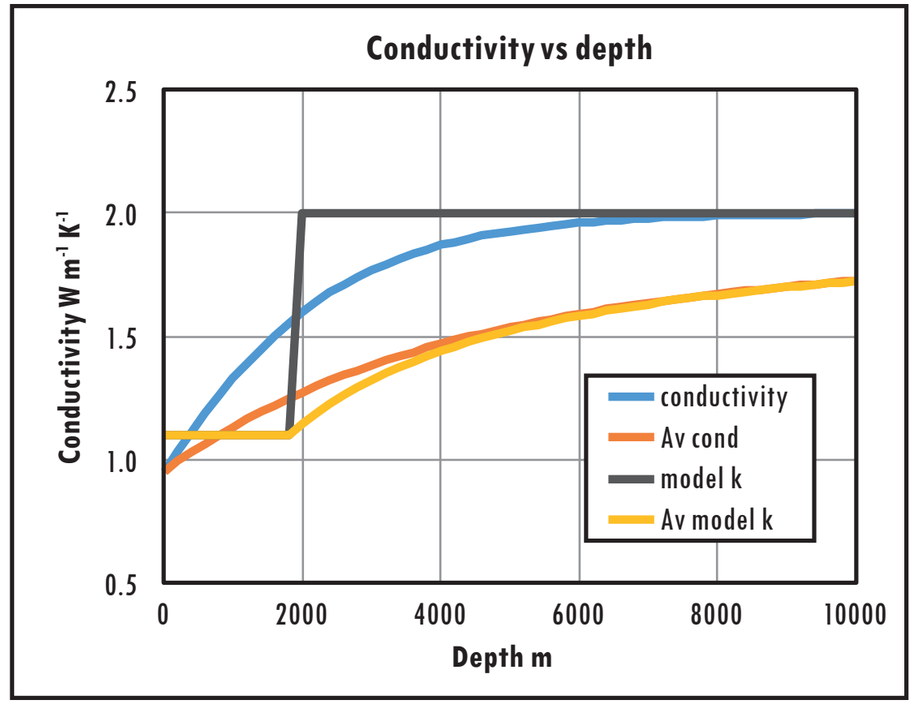

Figure 3.3.3.2: Thermal conductivity and average conductivity for porosity depth curve; conductivity and average conductivity for simple 2-layer model.

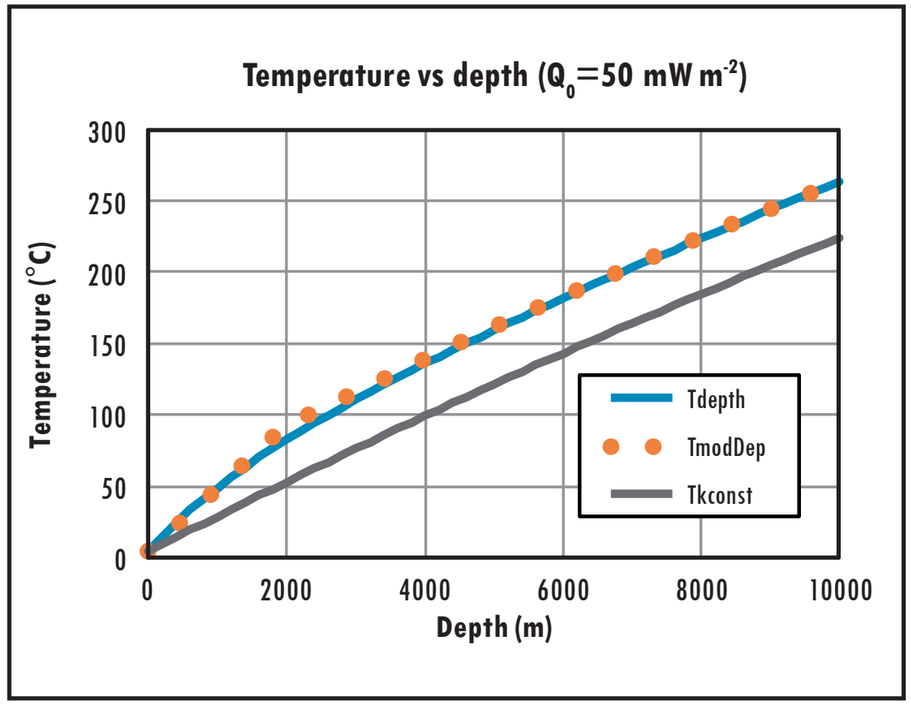

Figure 3.3.3.3: Temperatures at depth for porosity curve (Tdepth), 2-layer conductivity model (TmodDep) and equivalent for conductivity of 2 $Wm^{-1}K^{-1}$ (Tkconst).

3.4. Surface Heat flow and confidence estimation

3.4.1. Surface heat flow

After applying data selection criteria, onshore and offshore surface heat flow data have been compiled and spatially averaged onto a regular 0.25° x 0.25° grid, to generate an 'interpreted surface heat flow' dataset.

These spatially averaged data have been interpolated onto a regular 0.25° x 0.25° grid using the ArcGIS 'Topo to raster' tool (Figure 3.4.1).

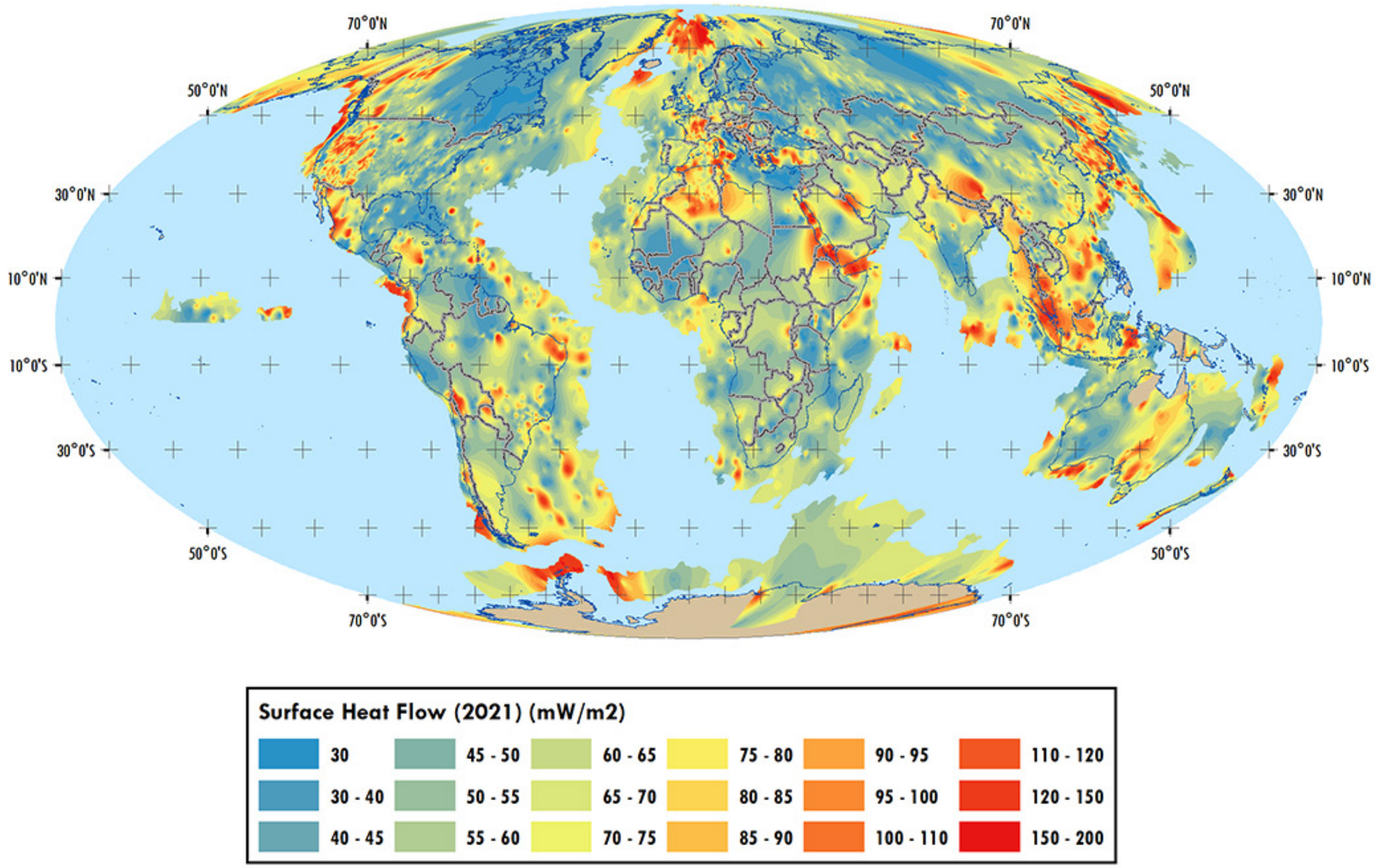

Figure 3.4.1: Global surface heat flow grid, interpolated from 'Interpreted' surface heat flow dataset using the ArcGIS Topo to Raster tool. Areas with poor data coverage have been masked out of the final grid.

3.4.2 Surface Heat flow confidence estimation

- Surface heat flow data are inherently variable in their quality and distribution.
- Getech have generated confidence polygons based loosely on crustal type and data coverage, scoring each onshore polygon according to the following categories:
  - Heat flow data quality (i.e., measurement type and consistency)
  - Heat flow data coverage
  - Tectonic complexity
  - Existence of volcanic activity or know shallow heat sources)
  - Occurrence of recent high sedimentation or denudation
- These scores have been used to categorise confidence in heat flow data (and therefore CTD estimated from surface heat flow, Figure 3.4.2) as follows:
  - High confidence
  - Medium confidence
  - Low confidence
  - Sparse/no surface heat flow data
  - Offshore heat flow data compilation

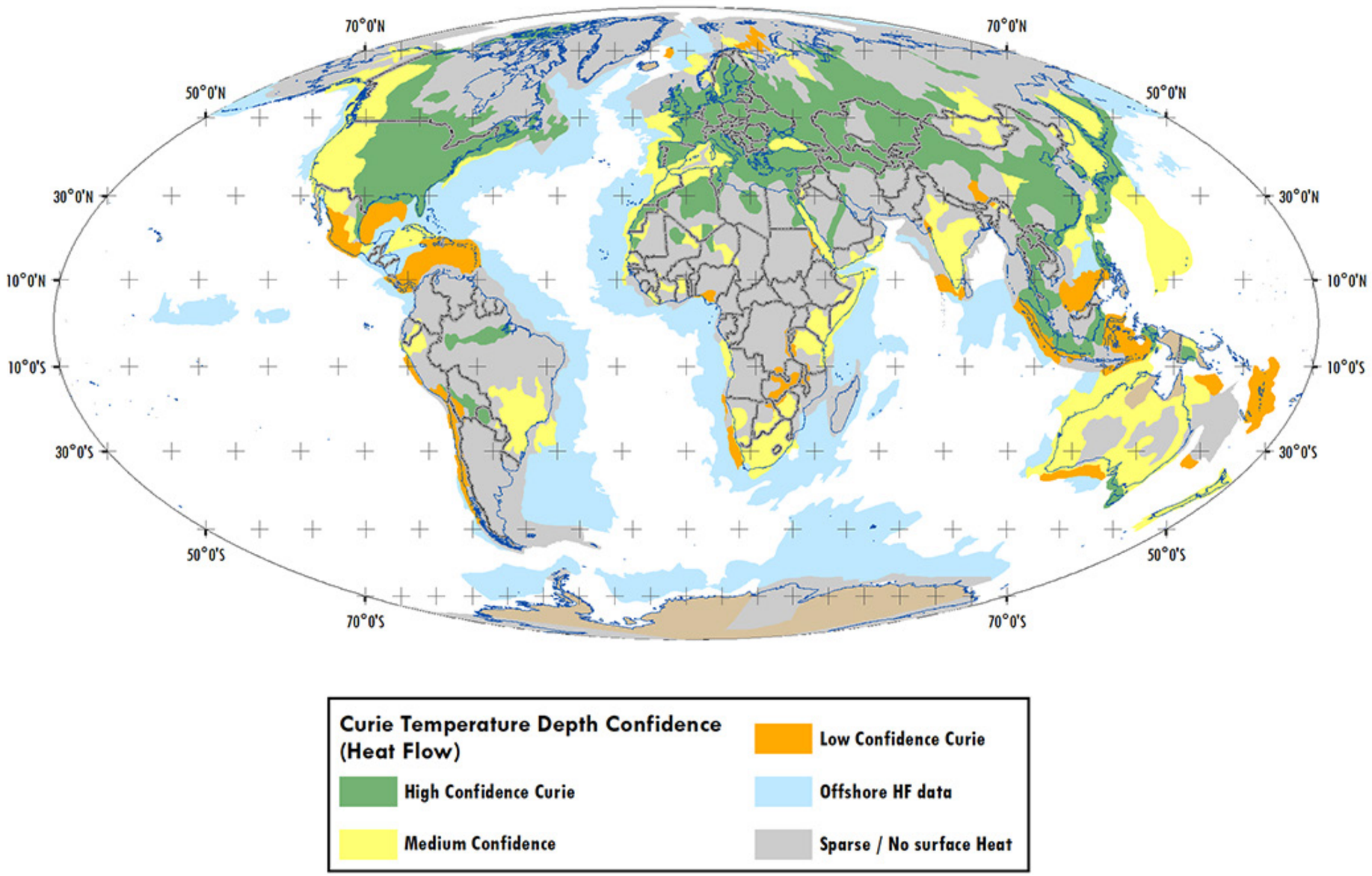

Figure 3.4.2: ***Heat flow confidence***

3.5. Results

CTD from surface heat flow has been predicted from Getech's surface heat flow grid and our simple three-layer crustal model. The results are shown in Figure 3.5.1. This CTD grid is used alongside heat flow confidence estimates (Section 3.4.2) as input for the final CTD grid integration (Section 6).

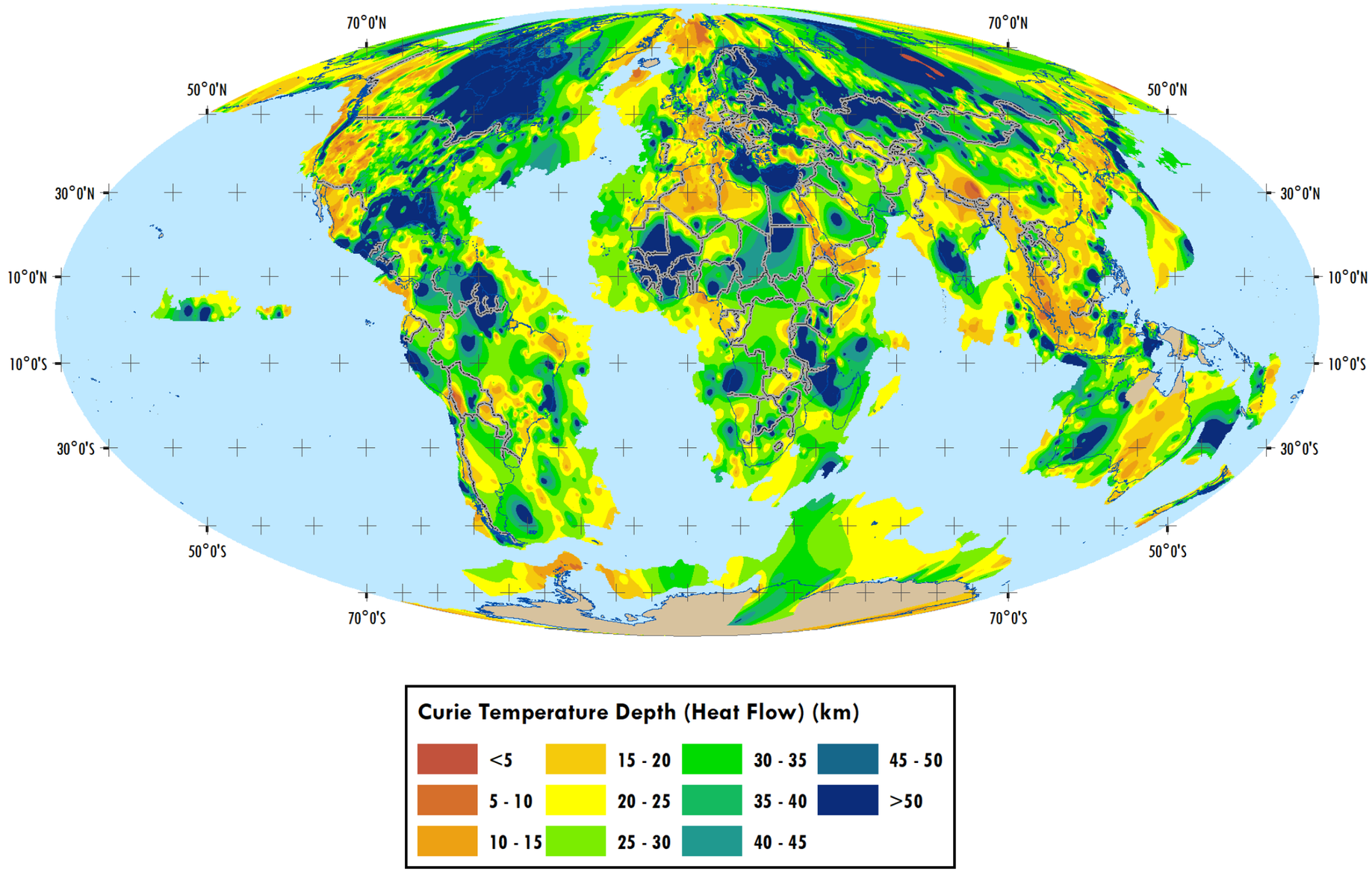

Figure 3.5.1: CTD predicted from surface heat flow

4. Estimating Curie Depth from Terrestrial Magnetic Data

4.1 Data

The magnetic data used in this project are from Getech's Global Magnetic Data Compilation (Figure 4.1.1), the result of 30 years of compiling, processing and integrating airborne, shipborne and ground magnetic surveys into a single 1 km grid of total magnetic field. It includes reprocessed public-domain data sets along with proprietary continental-scale compilations.

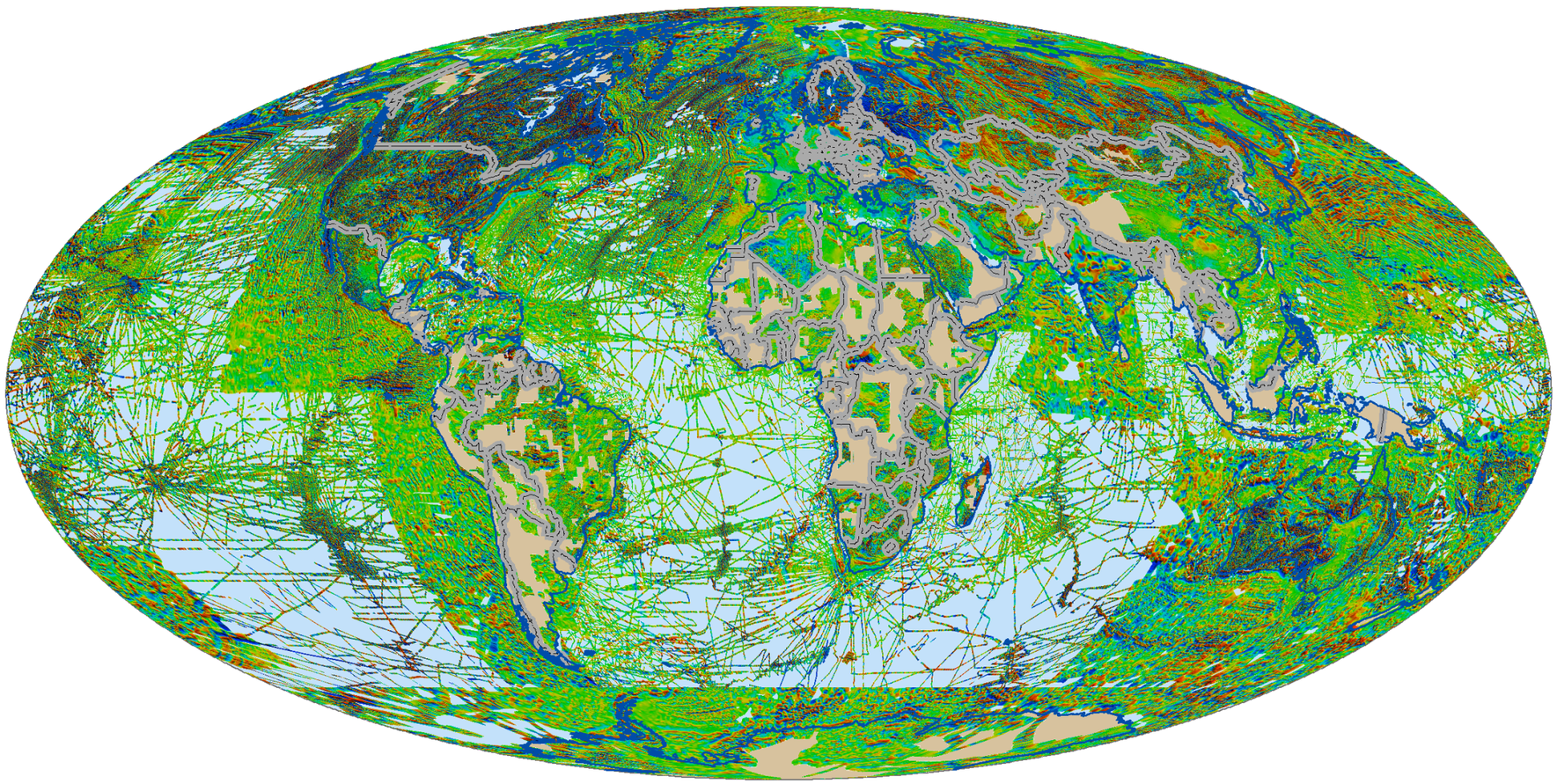

Figure 4.1.1: ***Getech's global magnetic data compilation***

4.2 The de-fractal method

To calculate the CTD from magnetic data, we applied the de-fractal magnetisation method of Salem et al. (2014). This method models the azimuthally averaged power spectrum of windows of magnetic data, to estimate depth to the base of magnetic material indicated by a reduction in the power at long wavelengths compared to a model where magnetisation continues down to infinity. This approach represents a significant development over various other spectral methods, which have been applied over the years (e.g., Connard et al., 1983). Previous methods make the assumptions that a) the magnetic layers are flat, and b) the magnetisation is random (uncorrelated). Our research indicates that the latter assumption is likely to be reasonable for older cratonic units of the crust, which have been heavily modified over a long period of geological time, but is unlikely to hold for younger geological units, particularly oceanic crust.

Fractal magnetisation is considered a more realistic distribution (e.g., Pilkington et al., 1994). The de-fractal method assumes that, rather than random, the crustal magnetisation is fractal and adjusts the power spectrum according to a fractal index. The observed power-density spectrum is defined by Blakely (1996) as:

$$\phi(k_x, k_y) = A(k_x, k_y)\phi_M(k_x, k_y)(e^{-kz_t} - e^{-kz_b})^2$$

Where $\phi_M(k_x, k_y)$ is the power-density spectrum of magnetisation, and $A(k_x, k_y)$ is a function that depends on the vector directions of magnetisation and ambient field. The final term controls the shape of the spectrum and is related to the depth to the top (Z_t) and bottom(Z_b) of the magnetic layer. Salem et al. (2014) show that power spectra of a randomly magnetised model and a fractal magnetised model with the same geometry are related by:

$$\phi_F(k_x, k_y) = \phi_R(k_x, k_y)k^{-\alpha}$$

where $\phi_F(k_x, k_y)$ is the observed fractal power spectrum, $\phi_R(k_x, k_y)$ is the randomly magnetised power spectrum, k is the radial wavenumber and α is the fractal index. The fractal index is related to the fractal parameter of magnetisation (β) by:

$\alpha = \beta - 1$

Setting β =1 yields results very similar to the randomly magnetised approach. Higher values of β represent increasingly correlated magnetisation (Figure 4.2.2). The basis of the de-fractal method is to convert an observed power spectrum into the equivalent power spectrum that would have been observed had the magnetisation in the area been randomly distributed. Once this has been done, conventional approaches using random magnetisation can be applied.

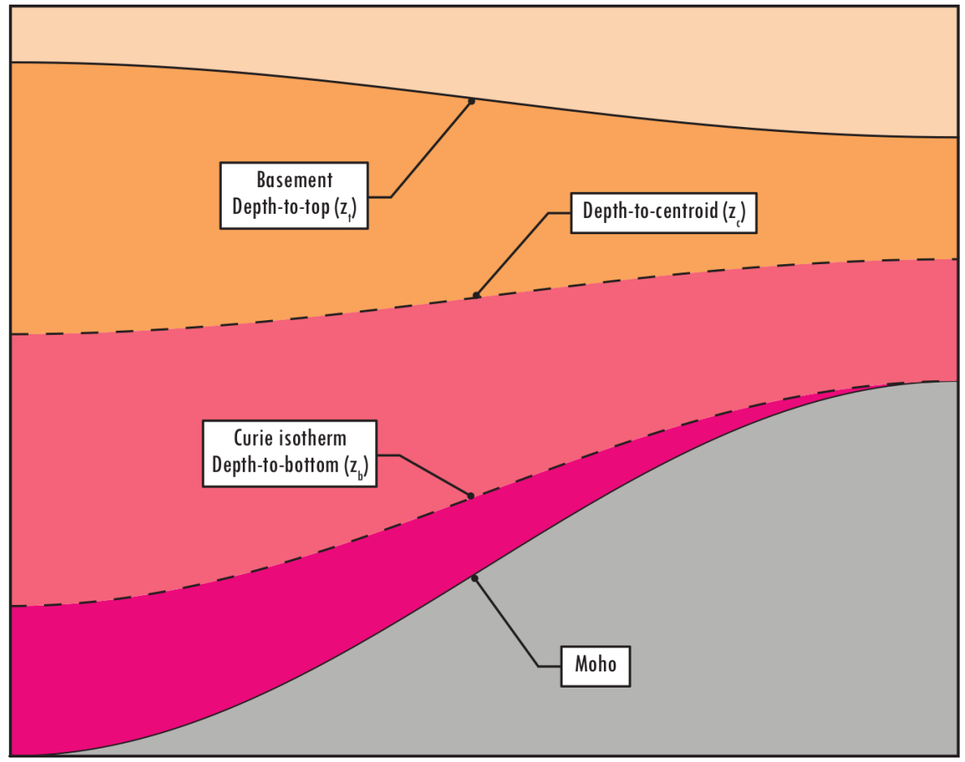

Figure 4.2.1: ***Nomenclature used in the calculation of CTD from terrestrial magnetic data***

4.3 Fractal Index

The selection of an appropriate Fractal Index has a significant effect on the final calculated CTD. As part of Globe, the crustal architecture has been remapped, utilising data from a wide range of sources, including available geological mapping and seismic data, global compilations of gravity and magnetic data, as well as interpretations from structural analyses, and plate modelling. For each crustal type, an appropriate Fractal Index value has been derived (Figure 4.3.1). A range of Fractal Indices were tested, and synthetic spectra compared to the observed spectra. A good fit between the observed and synthetic spectrum should give confidence that the Fractal Index is appropriate.

Depths to the top (Z_t) of the magnetic layer have been calculated using the method of Spector and Grant (1970) and for the centroid (Z_c) using the method of Tanaka et al. (1999). Once these are known, it is possible to calculate the depth to the bottom (Z_b) of the magnetic layer. These methods require analysis of wavelength bands that are likely to represent the signals from the top and centre of the magnetic layer, from the radially-averaged power spectra. Once this has been decided, the depths can be estimated from the gradient of the spectra across these wavelengths.

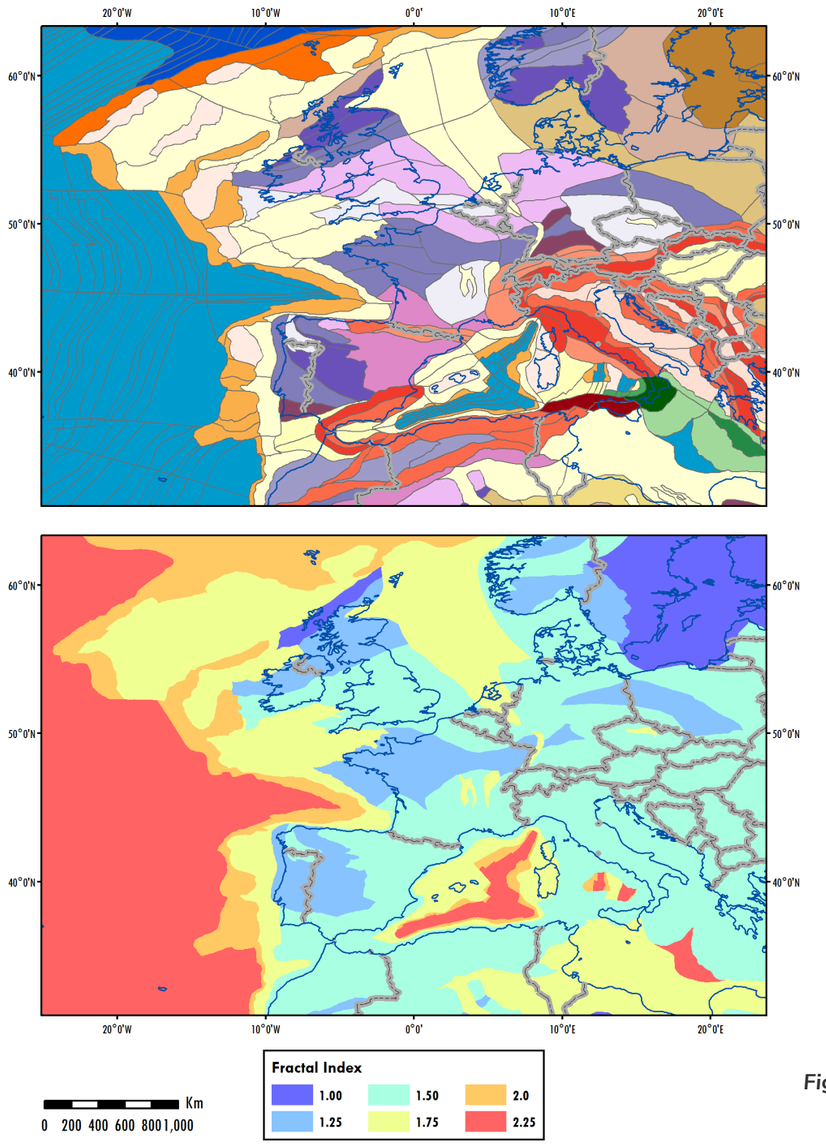

Figure 4.3.1: Getech's re-mapped crustal architecture (above) is used to map optimised Fractal Indices (bottom) which are provided as an input to the calculation of CTD from terrestrial magnetic data.

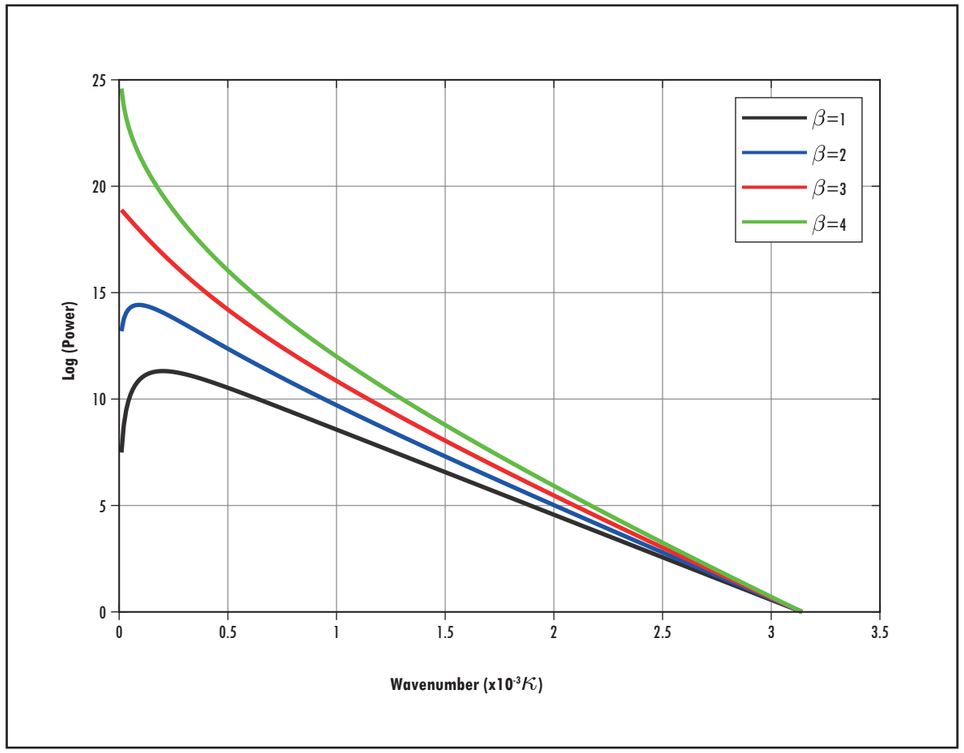

Figure 4.3.2: A layer with random magnetisation should appear as the black line, with a drop in power in the smallest wavenumbers associated with the base of the layer, and a subsequent slope associated with the top of the magnetic layer. As the magnetisation becomes more fractal (higher beta), the shape of the spectrum is modified.

4.4 Application

The wavelengths used to obtain estimates for z_c and z_t are allowed to change slightly, dependent upon the spectral data in each window. To calculate z_c from the scaled spectrum, a broad wavelength band between 30 and 128 km is used. Within this, the depth is estimated using a fixed number of points as shown below:

Window size	Z_c search window	Number of points	Z_t search window	Number of points
100 km	30 – 128 km	6	From 10 km to min. Z_c wavelength	3
200 km	30 – 128 km	12	From 10 km to min. Z_c wavelength	6
300 km	30 – 128 km	24	From 10 km to min. Z_c wavelength	12

The fixed number of points caused stability in the calculation and ensures the calculated gradient is representative of a significant part of the spectrum. The number of points increases as the window size increases as more wavenumbers are sampled in the larger window sizes. This ensures that the length of the wavenumber band used is the same for all windows. There will be several possible positions to estimate z_c within the broad band and the final chosen depth is the one that outputs the deepest solution. This has been chosen as potential problems that affect the correct estimation of the depth include overlapping onto the low-wavelength spectral peak, or overlapping into shorter wavelengths, which generally shallow the gradient if the window includes the part of the spectrum which describes depth to top z_t . Both effects lead to a shallowing of the estimated depth.

Once the minimum and maximum wavelengths have been selected for the calculation of z_c, then the minimum wavelength can be used as the maximum wavelength for use in the search for a band calculating z_t from the defractal spectrum. This prevents the two depth estimation wavelength bands from overlapping.

The CTD is calculated from a moving window of magnetic data. The choice of this window size is often a compromise. Larger window sizes will better sample the long wavelengths used to calculate the CTD; however, small-scale variations could be lost as each resulting depth is derived from a large geographical area. Smaller window sizes may better represent these small-scale variations in CTD; however, as the long wavelengths in the data will be represented by fewer points in the Fourier domain, there is a higher liability that the gradient will not be adequately represented and will be more susceptible to noise.

4.5 Results

Three moving window sizes of 100, 200 and 300 km have been applied to the magnetic data. An example for North America is shown in Figures 4.5.1a-c. Li et al. (2017) proposed stacking the results of different size windows to reduce noise in the final result. This approach has proven successful here, however stacking the 100 km window results with the others for the deepest sources leads to an artificially shallow CTD.

An approach was devised where the three window sizes are stacked where the CTD obtained from the 300 km window is shallower than 25 km, and only the 200 and 300 km windows are stacked where the 300 km result shows CTD ≥25 km. The results of this method are shown in Figure 4.5.1d, and the final global CTD grid from terrestrial magnetic data in Figure 4.5.2.

It has been commonly understood (e.g. Wasilewski et al., 1979) that mantle rocks in situ (as distinct, say, to chemically altered mantle rocks in the crust) are non-magnetic. In recent years, this has been questioned (e.g. Ferré et al., 2014), but it should be noted that where the CTD lies within the mantle, the depth to the base of the magnetic layer may actually represent the Moho. At temperatures above the Curie isotherm, magnetic minerals lose their ferrimagnetism, hence the base of the magnetic layer can be assumed to be at the CTD, provided the CTD lies within potentially magnetised material.

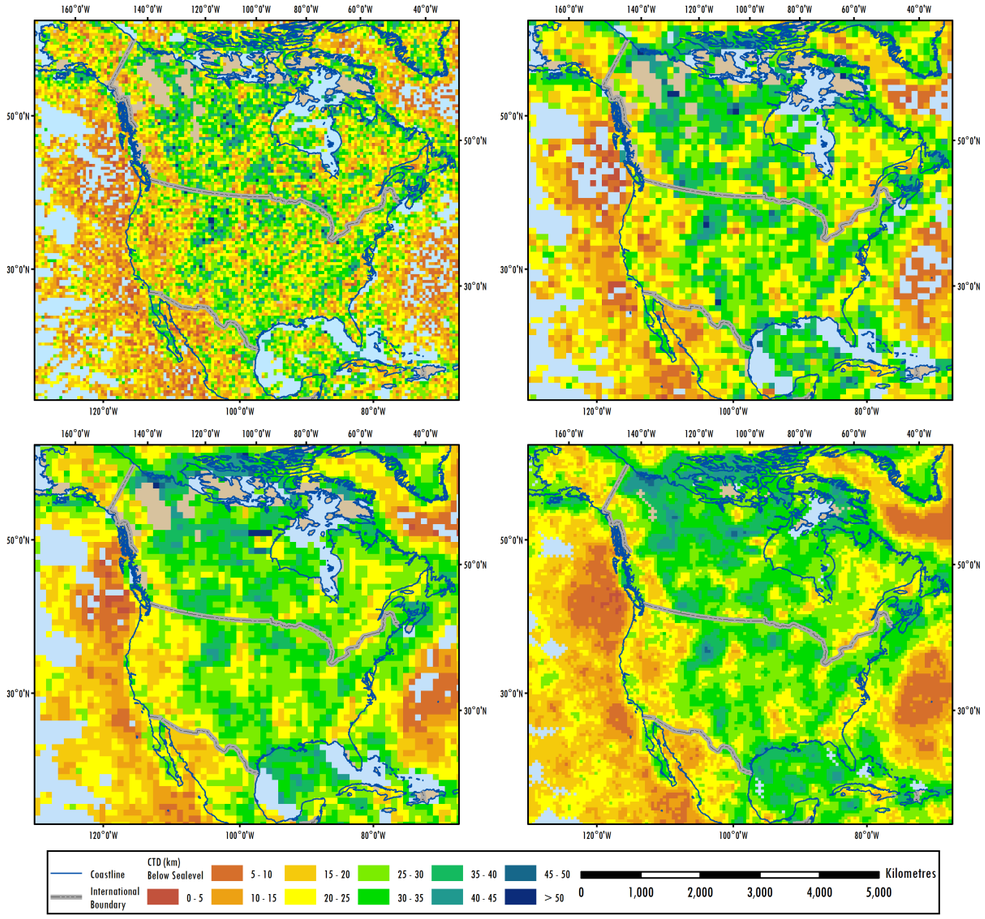

Figure 4.5.1: Example of window size for North America. (a) 100 km window, with 50 km step. (b) 200 km window with 100 km step. (c) 300 km window with 100 km step. (d) Final stacked result.

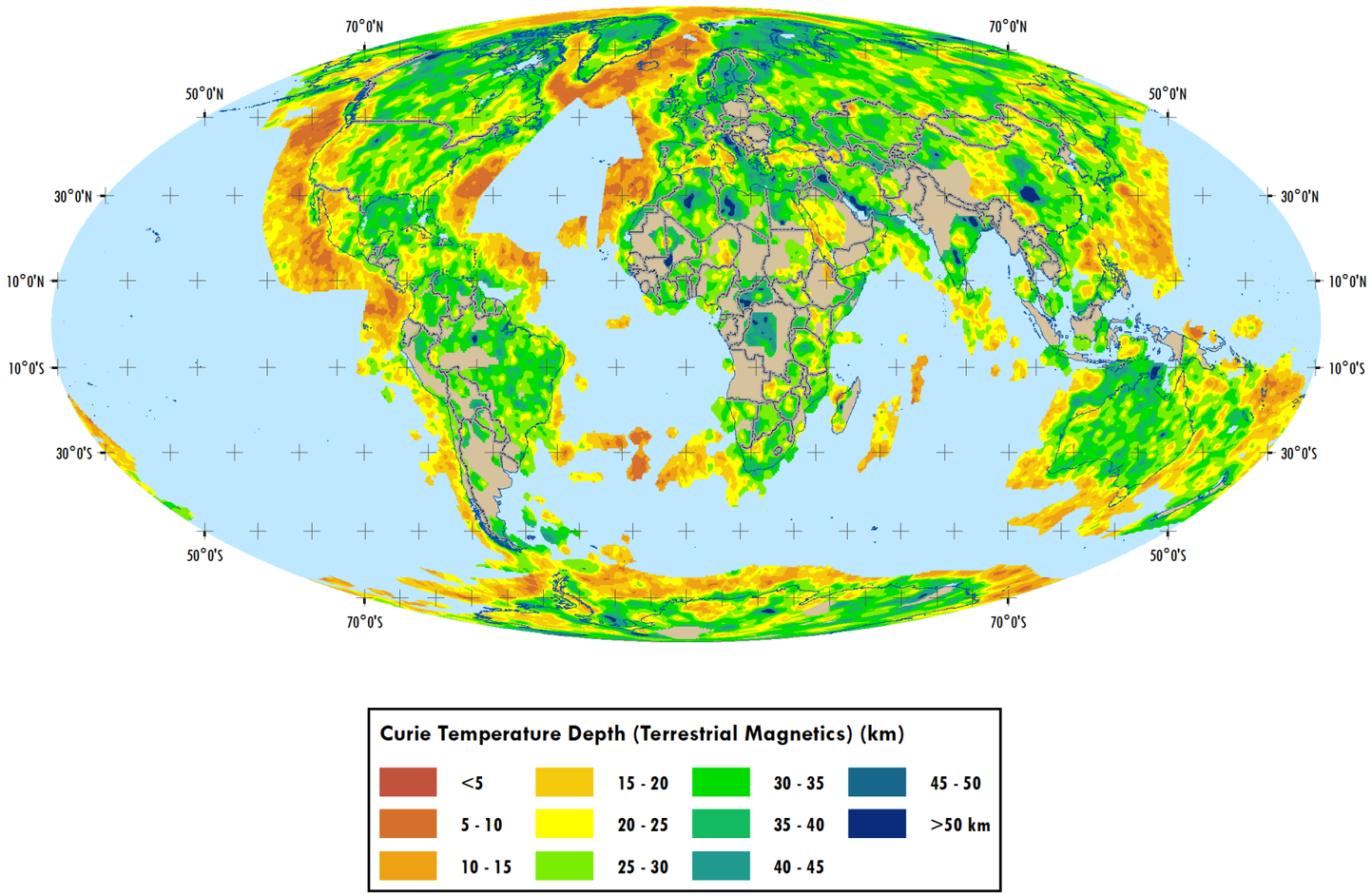

Figure 4.5.2: The Curie Temperature Depth calculated from terrestrial magnetic data.

4.6 Confidence

To calculate CTD from terrestrial magnetic data, the data need to have suitable spatial coverage. This allows the data windows used in the interpretation to adequately sample the long-wavelengths needed to map the centroid depth. In addition to this, the resolution of the data needs to be high enough that the wavelengths used to map the depth to the top of the magnetic layer are also sampled, and not aliased by the line spacing or gridding resolution. The terrestrial magnetic confidence overlay is therefore dependent upon the underlying resolution of the magnetic data (Figure 4.6.1).

Where line data or locations are available the confidence overlay reflects the line spacing. Where Getech has been provided with a gridded data set only, an estimation of the line spacing has been made depending upon whether the available gridded product is likely to have been derived at maximum resolution from the underlying line data, or whether it has been down sampled grid from a higher resolution product. In the case of the latter, an estimate of the line spacing is made that is equivalent to the resolution of the available grid.

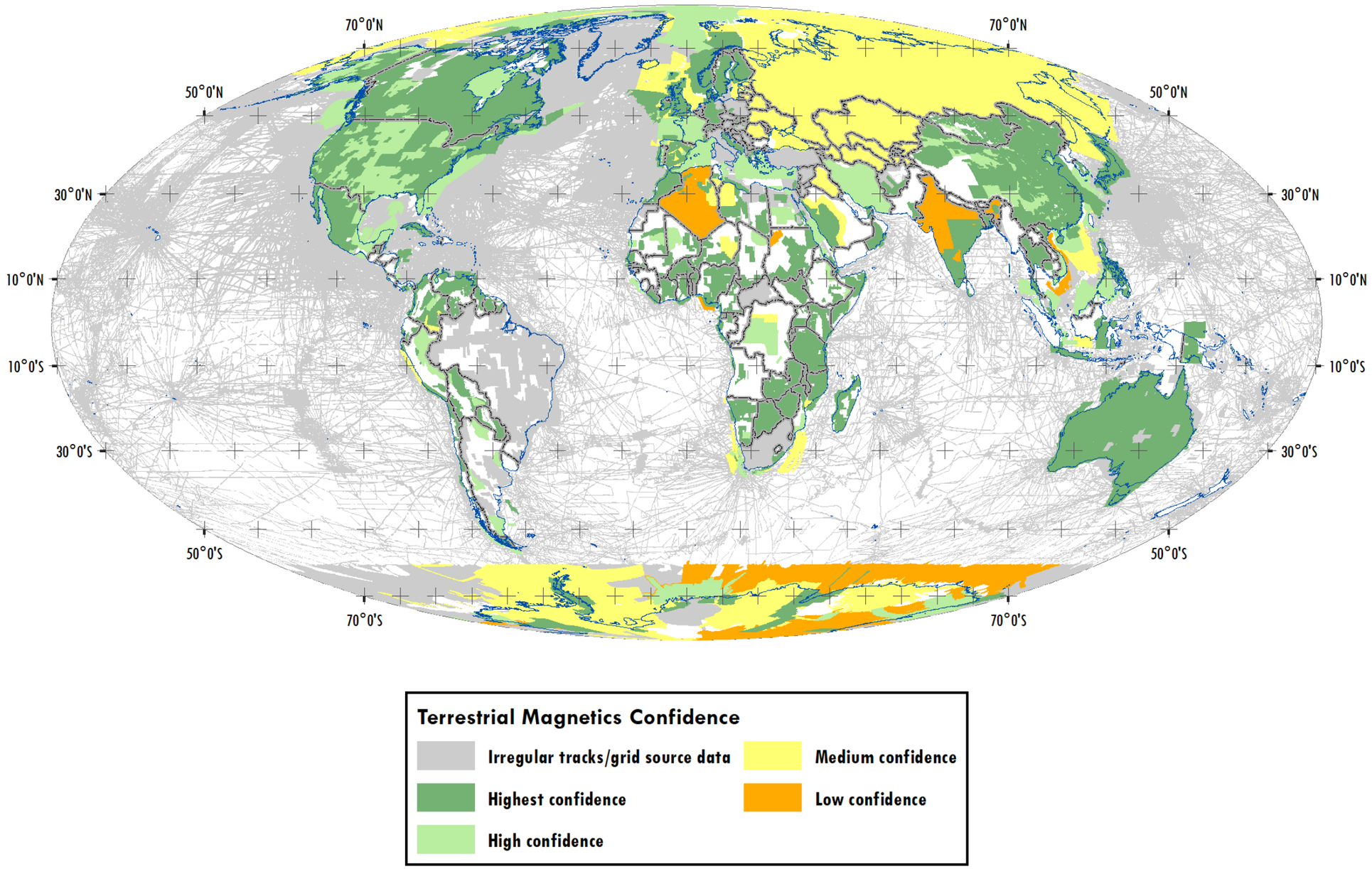

Figure 4.6.1: Confidence overlay for the terrestrial magnetic data.

5. Estimating Curie Depth from Satellite Magnetic Data

5.1 Data

Previous estimates of Curie Temperature Depth (CTD) from satellite magnetic data (e.g., Fox Maule et al., 2005) used the MF series of magnetic models based on the CHAMP satellite. Here, the CTD has been calculated from the LCS-1 model (Figure 5.1.1). As well as utilising the latest four years of CHAMP measurements (September 2006 – September 2010, when the satellite orbit was lowest and solar activity was reduced), the LCS-1 (Olsen et al., 2017) model includes data from two satellites from the Swarm mission between April 2014 and December 2016.

In addition to the extra data, the LCS-1 model has been generated using an L1 norm model regularization, as opposed to the L2 norm applied to MF7. The advantage of this is to remove the dominance of the contribution from high-amplitude features, and hence the model should possess locally higher amplitude features, but importantly more reliably represent the signals from low-amplitude regions. With LCS-1, Olsen et al. (2017) compared the magnetic field with Australian terrestrial data and found reliable results down to ~250 km wavelength.

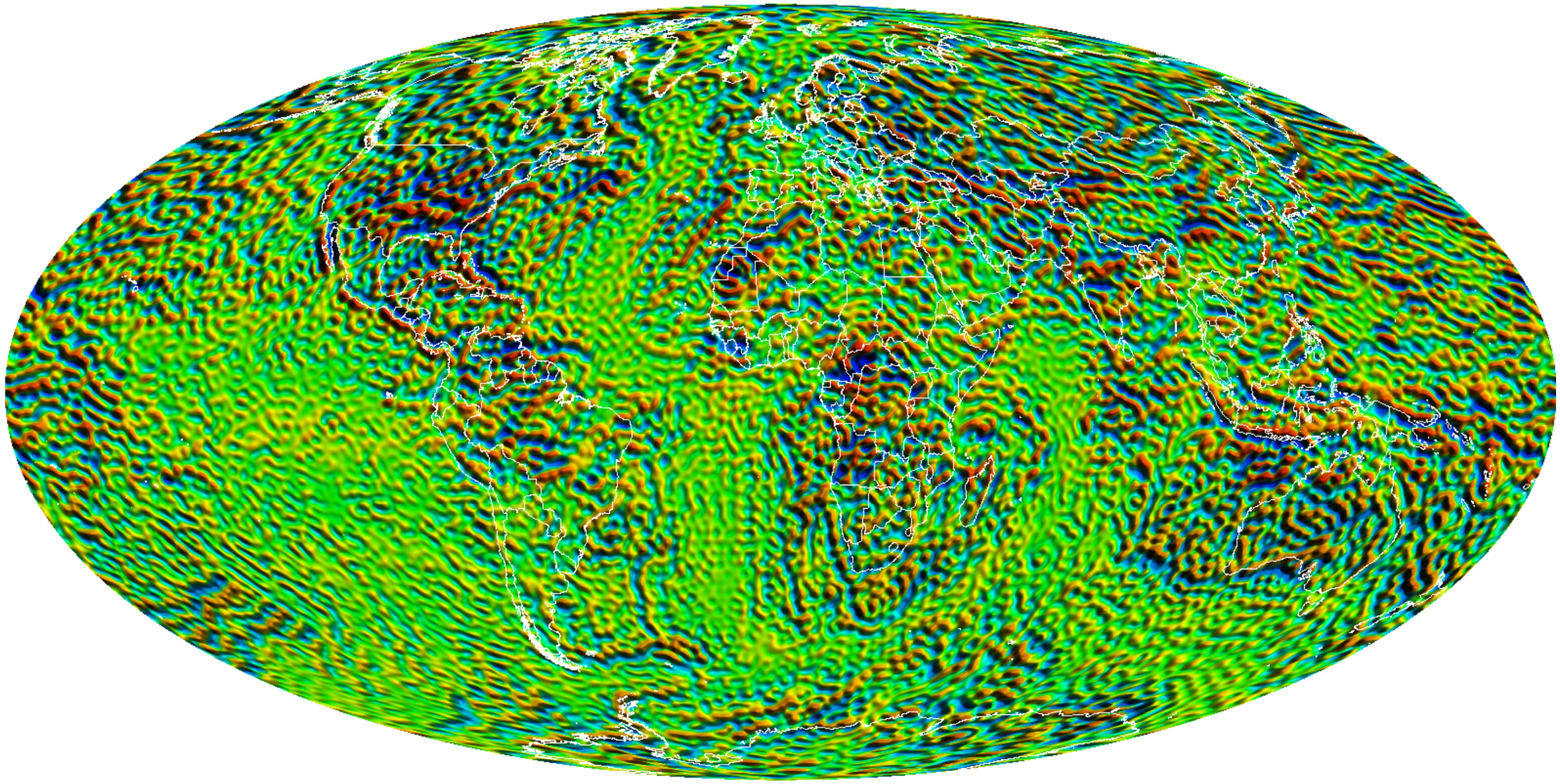

Figure 5.1.1: ***LCS-1 satellite magnetic data.***

5.2 Methodology

As the magnetic signal measured at the satellite is heavily attenuated due to the altitude, only the longest wavelengths of the field are recovered. This means it is not possible to apply the typical spectral methods applied to terrestrial magnetic data, as the relative separation of the top and base of the magnetic layer are relatively small compared to the distance to the satellite (Figure 5.2.1). Therefore, CTDs from satellite data must be calculated using a different approach. Fox Maule et al. (2005) applied an inversion for a magnetic layer in the crust to estimate CTD for Antarctica. Here, we use a simpler approach, where we assume that the amplitude of the shorter satellite magnetic wavelengths represents the variation in the thickness of a thin (relative to satellite altitude) magnetic layer.

To produce the best spatial resolution of the resulting thickness map, a minimum data window size is required, however smaller window sizes can restrict the longest wavelengths that can be utilised. A 1° x 1° mesh was selected, and at each point the data were projected into a 675 x 675 km window using a Lambert Equal Area projection. The radially averaged power spectrum was calculated for each window, and the 'anomaly amplitude' was taken to be the square root of the radially averaged power represented at each wavenumber band. We used the first four wavenumbers (wavelengths between 1600 and 178 km). Beyond this there are artefacts in the signal, which is to be expected as these wavelengths are shorter than 250 km, which is the estimated shortest reliable wavelength present in the LCS-1 data set (Olsen et al., 2017).

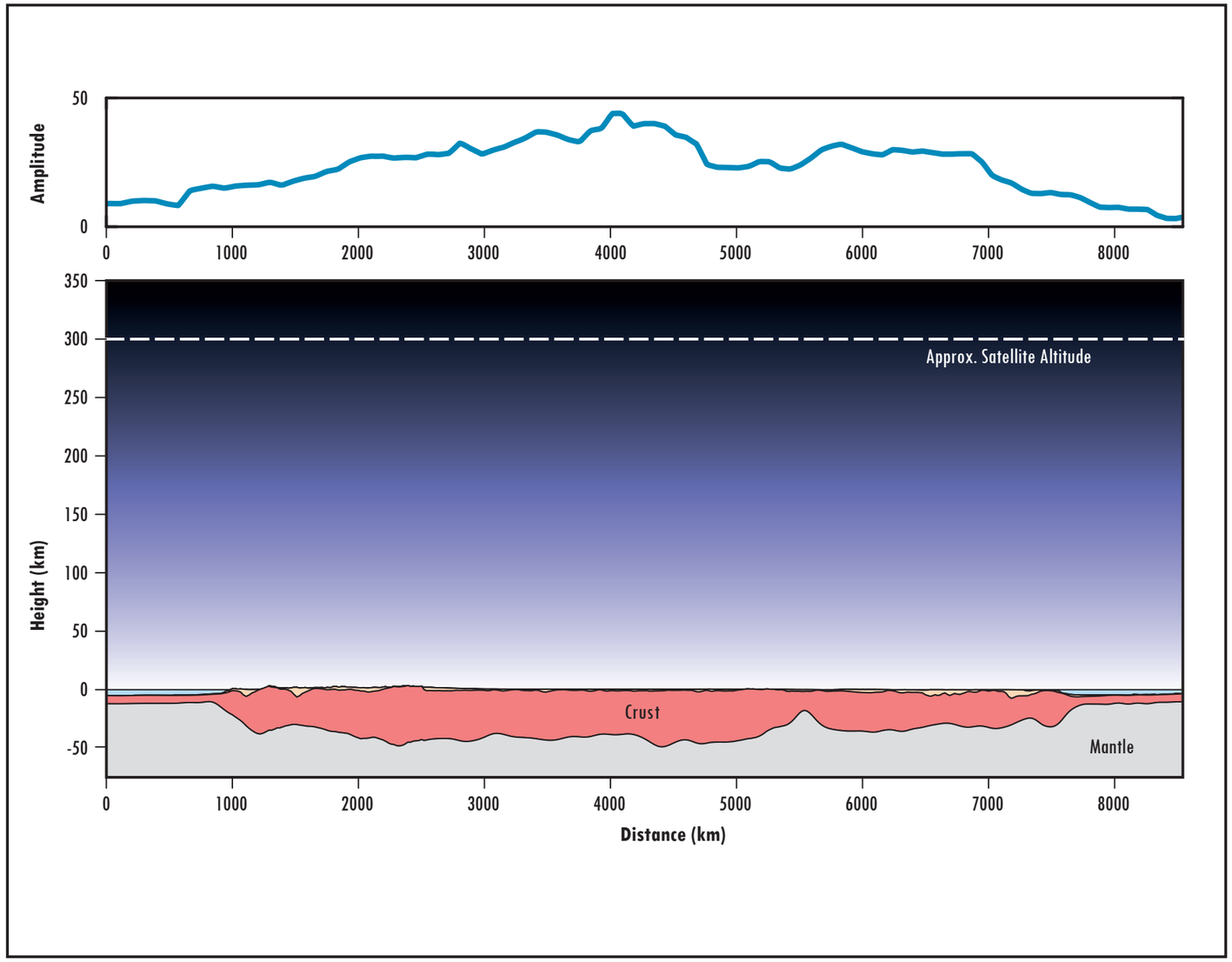

Figure 5.2.1: Illustration of the relative satellite height, compared the to the thickness of the magnetic crust. This requires different methods to be used compared to the interpretation of terrestrial magnetic data. The magnetic anomaly amplitude is related to magnetic layer thickness, and can be converted to CTD once corrections for latitude and magnetisation have been made.

5.3 Corrections

Latitude effects the amplitude of the magnetic field due to an increase in inducing field strengths at high latitudes, and geometrical effects related to the change in the field vector from horizontal at the equator, to vertical at the pole. Maus and Haak (2002) defined theoretical equations for induced and remanent magnetisation and show that amplitude increases with latitude by a factor of 3.27 from the equator to the poles for induced magnetisation, and 1.22 for remanent magnetisation. Therefore, it is important to identify the ratio of remanent to induced magnetisation. A least-squares fit approach to the observed anomaly amplitudes was applied separately for continental and oceanic crust. The results show a remanent contribution of ~21% for continental crust, and ~70% for oceanic crust (Figure 5.3.1). These values are then used to correct the amplitudes, in order to remove the latitude effects from the result.

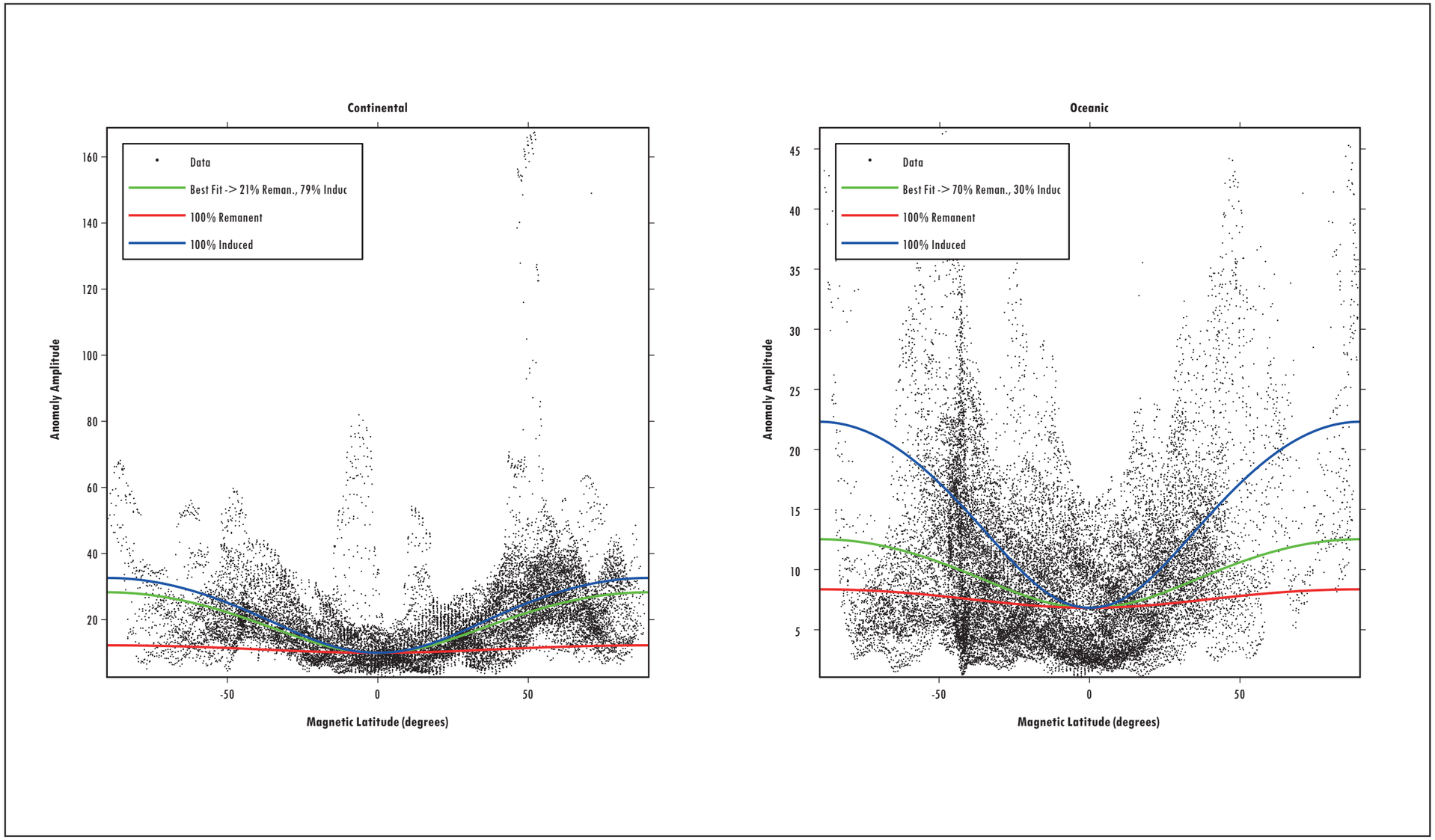

Figure 5.3.1: Identifying the ratio of remanent to induced magnetisation for continental (left) and oceanic (right) areas. The data are then subsequently corrected to remove latitude bias from the final result.

Once the latitude effects have been removed from the data, the resulting amplitudes can be scaled to estimate the thickness of the magnetised layer. Plotting the observed amplitudes against the CTD from the terrestrial magnetic interpretation shows a large degree of scatter (Figure 5.3.2). To improve the result, large-scale variations in strength of crustal magnetisation must be considered when relating the amplitude to magnetic layer thickness, and then CTD. This has been done by analysis of the spectra from the terrestrial magnetic interpretation. The DC shift in the spectrum is related to several variables, but will largely be representative of an estimate of magnetisation. When sampled to the satellite points, there is a definite relation between the scatter observed and the magnetisation (plotted in colour on Figure 5.3.2). For continental areas, where the terrestrial magnetic data coverage allows the magnetisation to be estimated, a function relating satellite amplitude and magnetisation to the magnetic layer thickness has been derived. In oceanic areas, where the terrestrial data coverage is insufficient for the magnetisation to be reliably estimated, a linear function is used, assuming a constant crustal magnetisation.

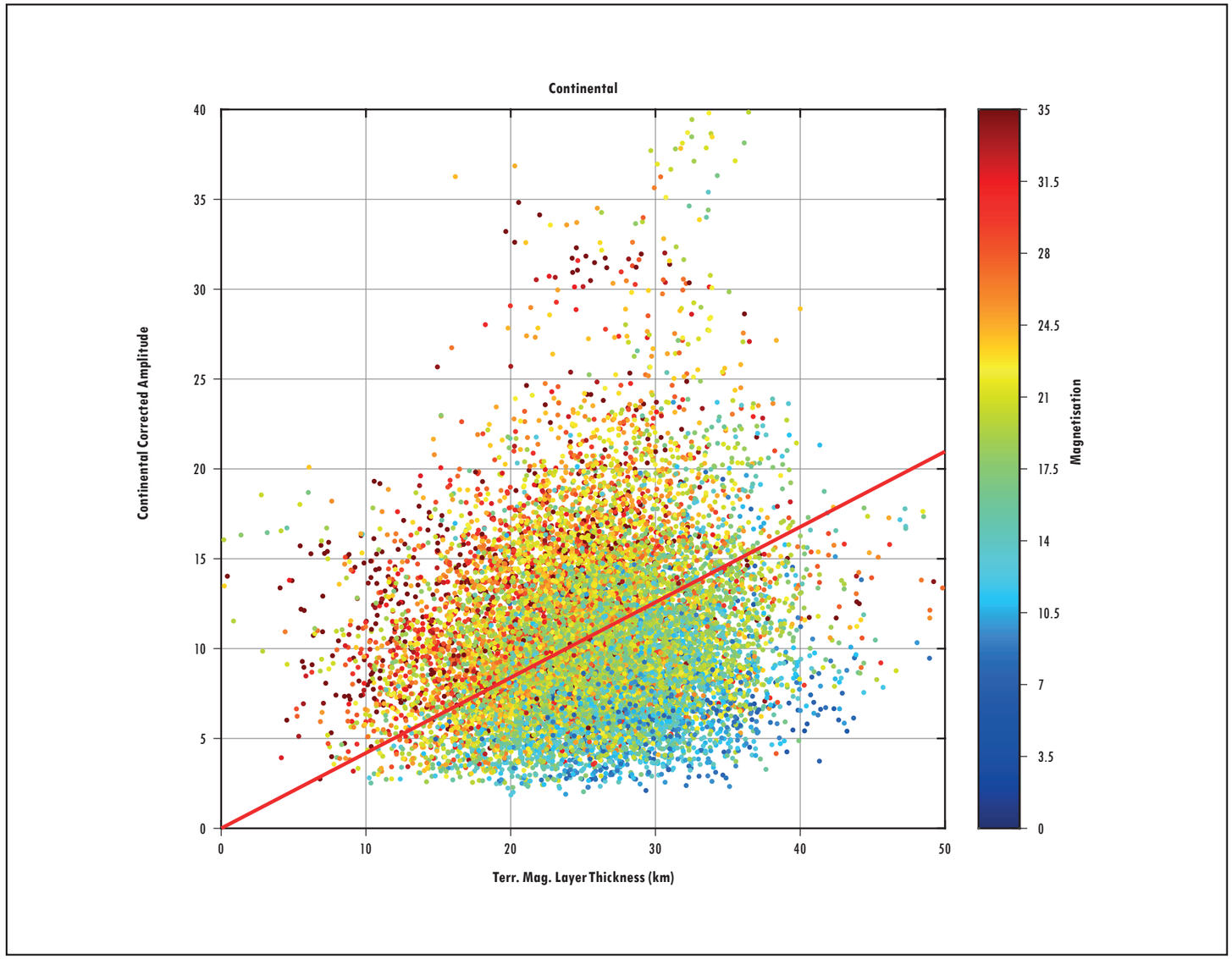

Figure 5.3.2: The relation between the latitude-corrected amplitude and the magnetic layer thickness is not linear, and the crustal magnetisation has to be included in the function.

5.4 Results

Once the magnetic layer thickness is calculated, it can be converted to CTD by adding the basement depth. Some local high-amplitude anomalies that cannot be fully accounted for using the magnetisation model are still present in the data and are required to be removed as they are unlikely to truly reflect variations in the magnetic layer thickness. Therefore, where the calculated CTD is deeper than 45 km, and deeper than the depth-to-Moho, the points have been removed and interpolated. The final estimate of CTD from satellite magnetic data (Figure 5.4.1) has been low-pass filtered at 675 km wavelength to reflect the window size.

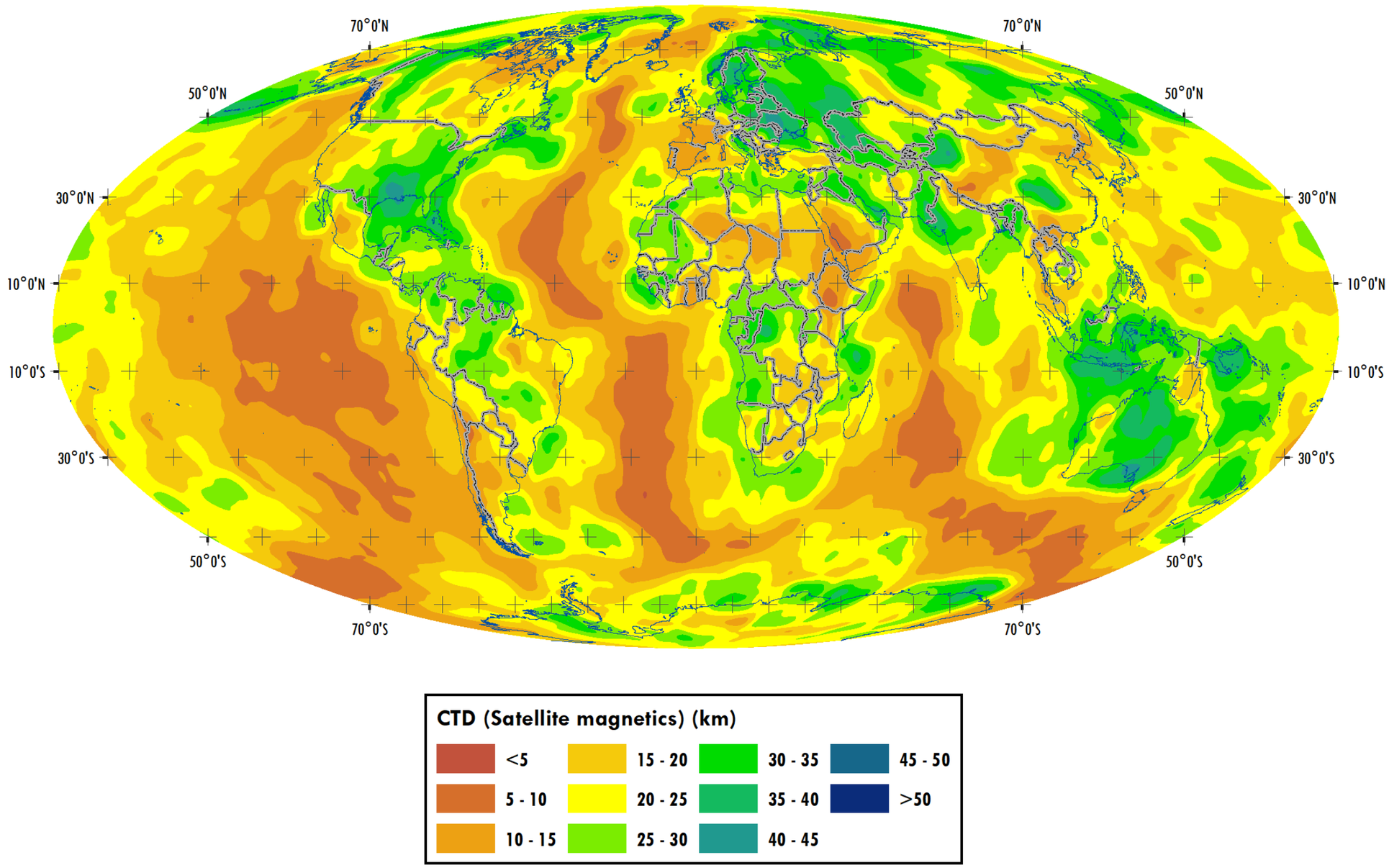

Figure 5.4.1: The Curie Temperature Depth calculated from satellite magnetic data.

6. Integrated Curie Temperature Depth and Prediction of Temperature at Depth

6.1. CTD Grid Differences

Each of the three approaches for estimating CTD has its own characteristics:

- The heat flow approach predicts temperatures from surface or near-surface observations based on estimates of physical properties; thus, the temperature estimates are liable to become less accurate with depth, but incorporation of surface heat flow values into estimates of radiogenic heat production should restrict values to realistic limits. Results are only produced in areas with heat flow observations; where heat flow data density is high, the filtering applied should limit the effect of small-scale variability and make results more robust, but where data are sparse, these effects will be aliased into the results.
- The terrestrial magnetic approach is the only one of the three methods that aims to detect the CTD directly by recognising where the rocks become non-magnetic. The results are limited to areas where there is continuous coverage of consistently processed magnetic data. The approach assumes a fractal distribution of magnetisation, although the ability to vary the fractal index means that this assumption is generally close to correct. The resolution is limited by the window size, which is 100 km or bigger.
- Satellite magnetic results are available globally due to the near-polar orbits of magnetic satellites. The results, however, are of low resolution due to the large window size (675 km) used in the magnetic thickness estimation. Very large depths have been limited, but spurious large-scale variations may still remain.

The quality of results from terrestrial magnetic data and from heat flow data are dependent on the quality of available data; satellite results should have consistent quality. Therefore, it will be expected – and is observed – that there will be mismatches between results, especially near the edges of coverage of each data type.

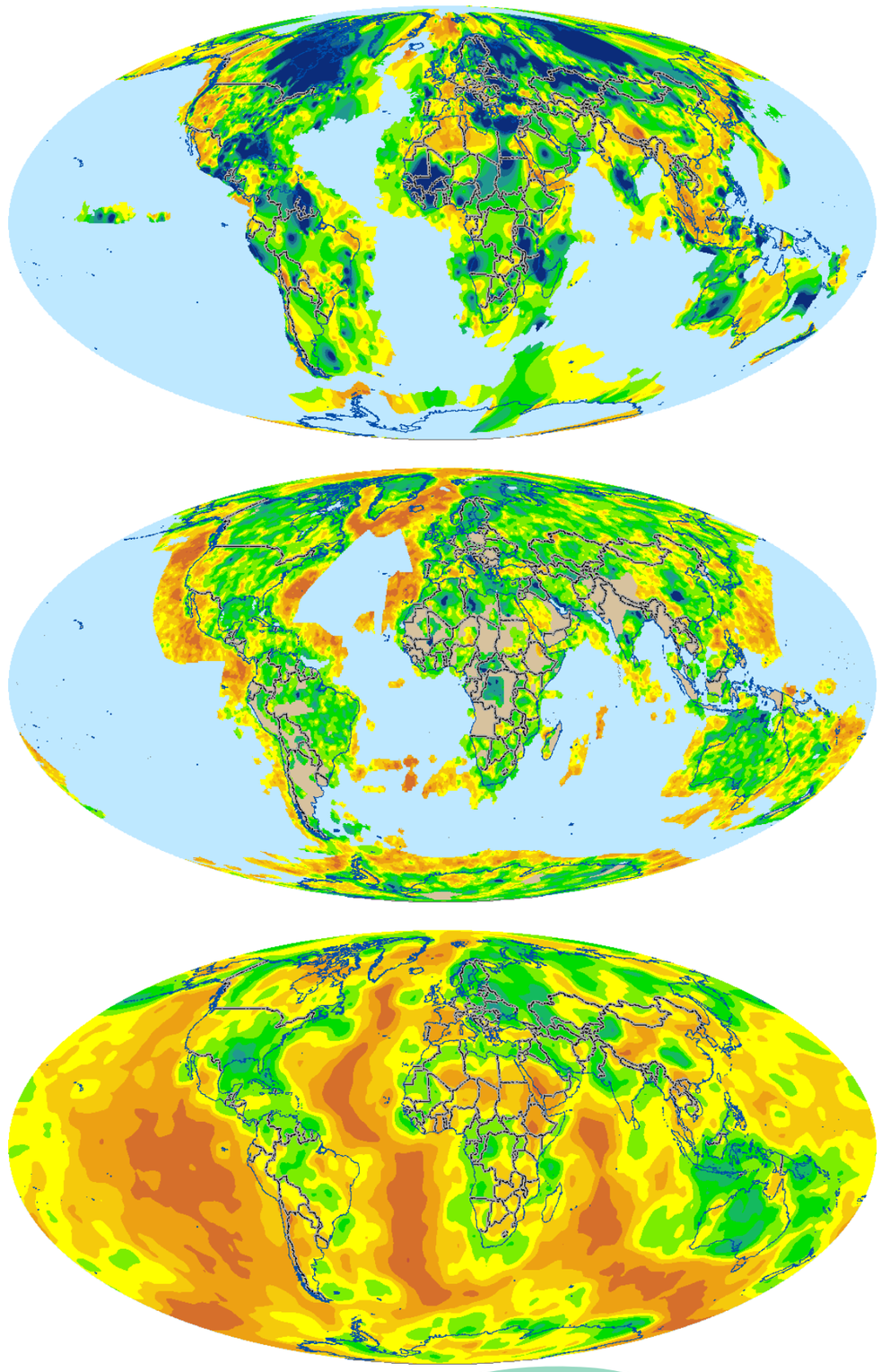

Figure 6.1.1: ***CTD from (top) surface heat flow, (middle) terrestrial magnetic data, and (bottom) satellite magnetic data***

6.2. CTD Grid Hierarchy

The three different approaches to calculating CTD (heat flow, terrestrial magnetic and satellite magnetic data) need to be combined into a single integrated grid, prior to calculating the temperature-at-depth layers. This has been done depending upon the confidence of the result for each method at that point, globally. For the 2021 delivery of Globe, the integrated CTD grid is constructed using the following priority system:

1. Heat Flow (High Confidence)
2. Terrestrial Magnetics (High Confidence)
3. Heat Flow (Medium Confidence)
4. Terrestrial Magnetics (Medium Confidence)
5. Heat Flow (Offshore)
6. Satellite Magnetic
7. Interpolation

Once the polygons were selected based on the confidence overlays, small polygons (<10 sq.degrees) were removed and replaced by the surrounding data type, to avoid rapid changes in the source data type, and reduce unnecessary areas of blend. A 1° buffer was applied to each coverage polygon, and the data were merged using a cosine blending function to ensure a smooth transition between the various grids within the blended areas.

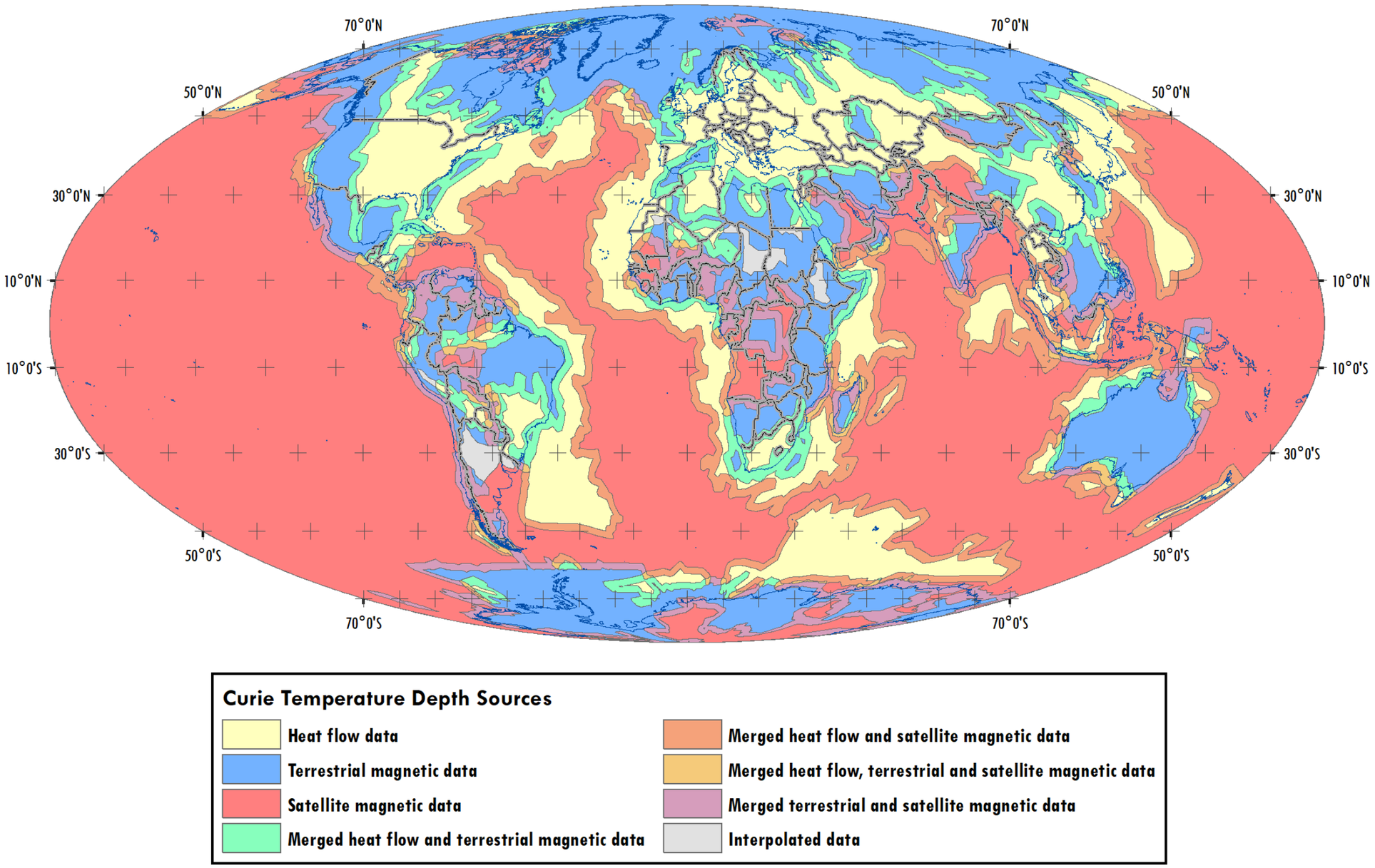

Figure 6.2.1: Overlay showing the input data sources to the final integrated CTD map.

6.3. Final Integrated CTD

In the final product, it was necessary to introduce some small areas of interpolation instead of the satellite magnetic data (which has full and consistent coverage), as these were resulting is unrealistic rapid changes in the CTD. The final integrated CTD map is shown in Figure 6.3.1. This map has full global coverage and has subsequently been used to generate temperature-at-depth maps, described in the next section.

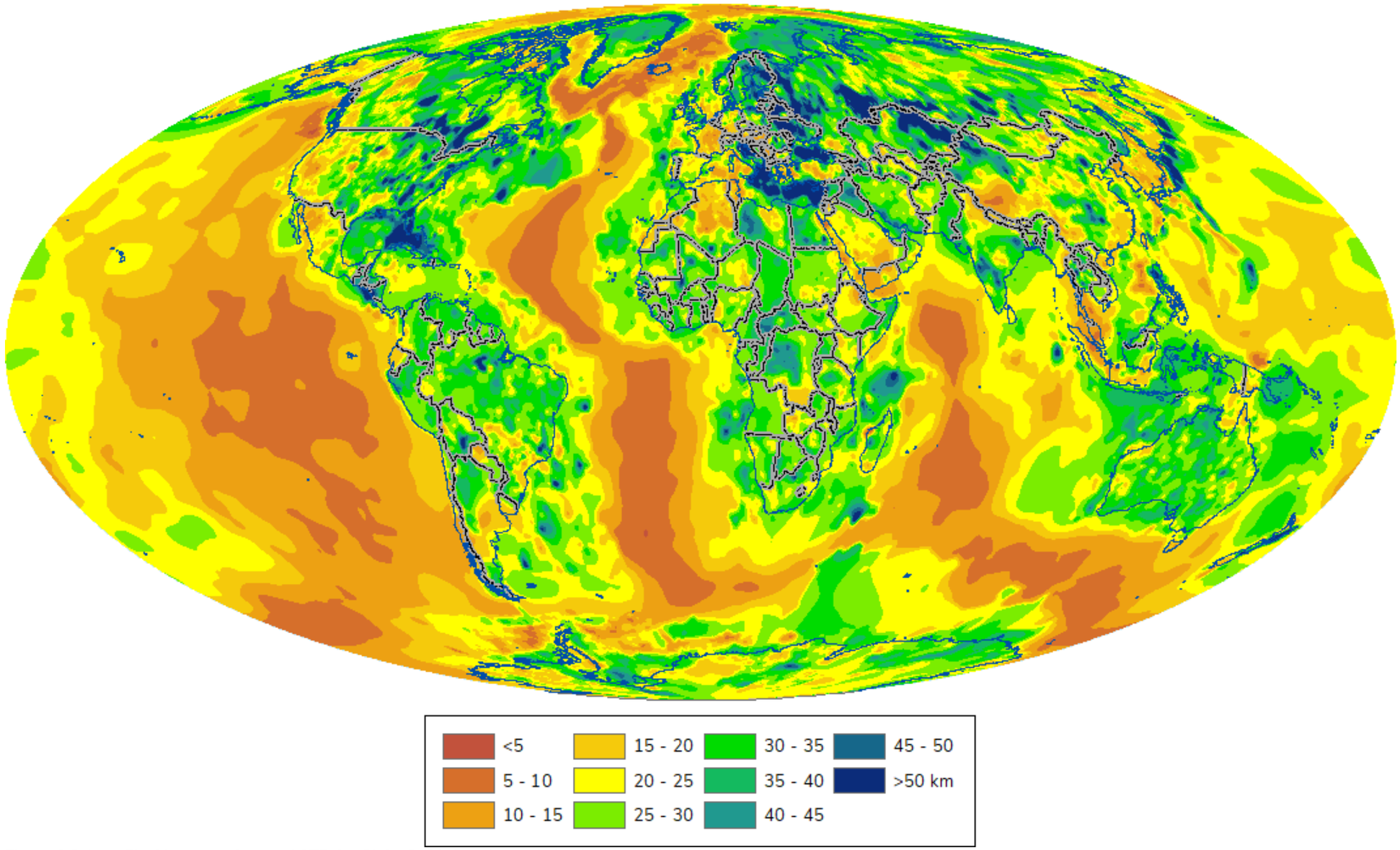

Figure 6.3.1: Final integrated map of CTD for Globe 2021. Depths are in km below sea level

6.4. Prediction of Temperature with Depth: Globe 2021

After generating a globally complete, integrated CTD grid (Section 6.3, Figure 6.3.1), an automated iterative trial and error approach has been used to back-calculate the equivalent surface heat flow value that will generate the integrated CTD value for each grid cell, assuming the same physical model that was adopted in Section 3.

The resulting globally complete surface heat flow grid has then been used as input to calculate grids of temperature at a series of depths, as well as the temperature and heat flow at basement (for subscribers of the Globe Depth to Basement module). These temperature grids (Figures 6.4.1-6.4.10) correspond to the following depths below surface (where we define surface as the topographic surface onshore and the sea floor offshore):

- 2 km
- 4 km
- 6 km
- 8 km
- 10 km
- 15 km
- 20 km
- 25 km
- 30 km
- 35 km

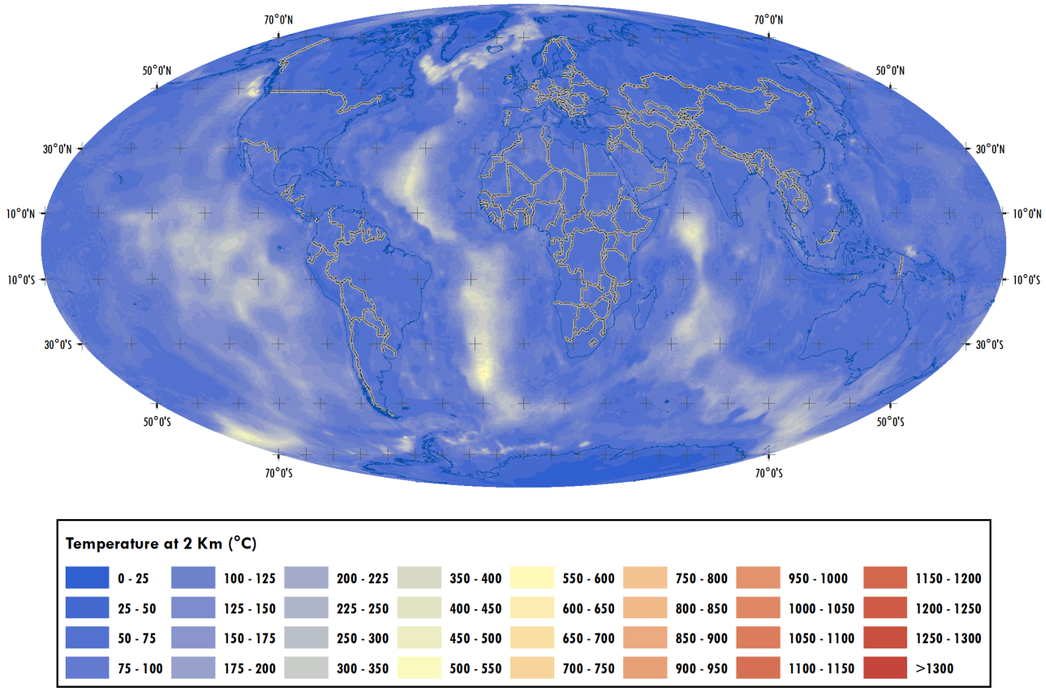

Figure 6.4.1: Temperature at 2 km below surface

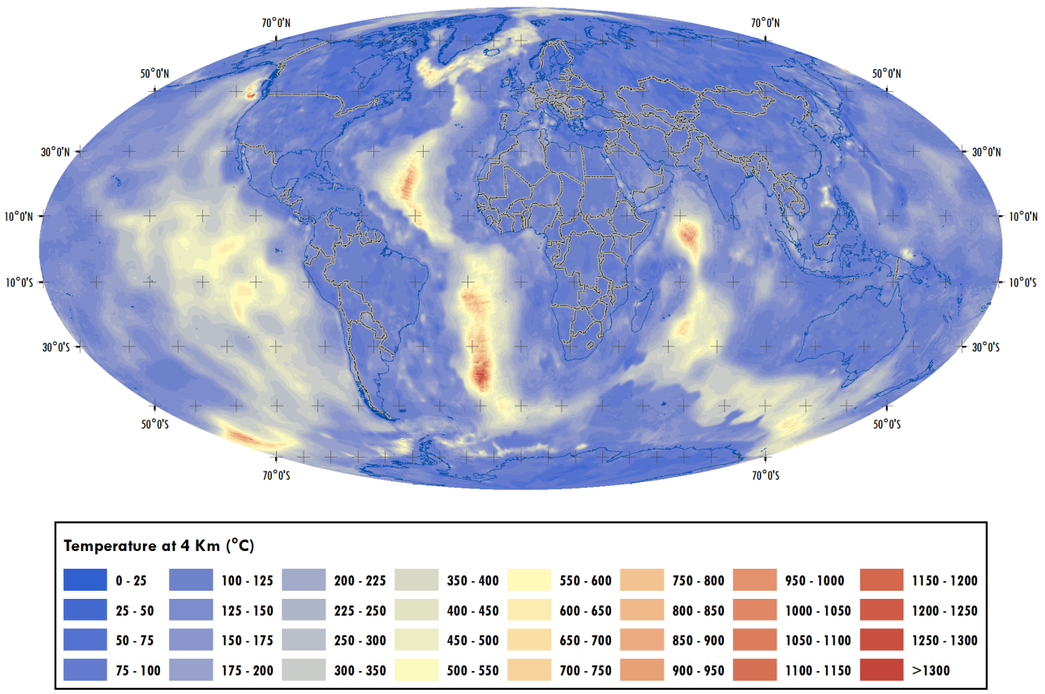

Figure 6.4.2: Temperature at 4 km below surface

Figure 6.4.3: Temperature at 6 km below surface

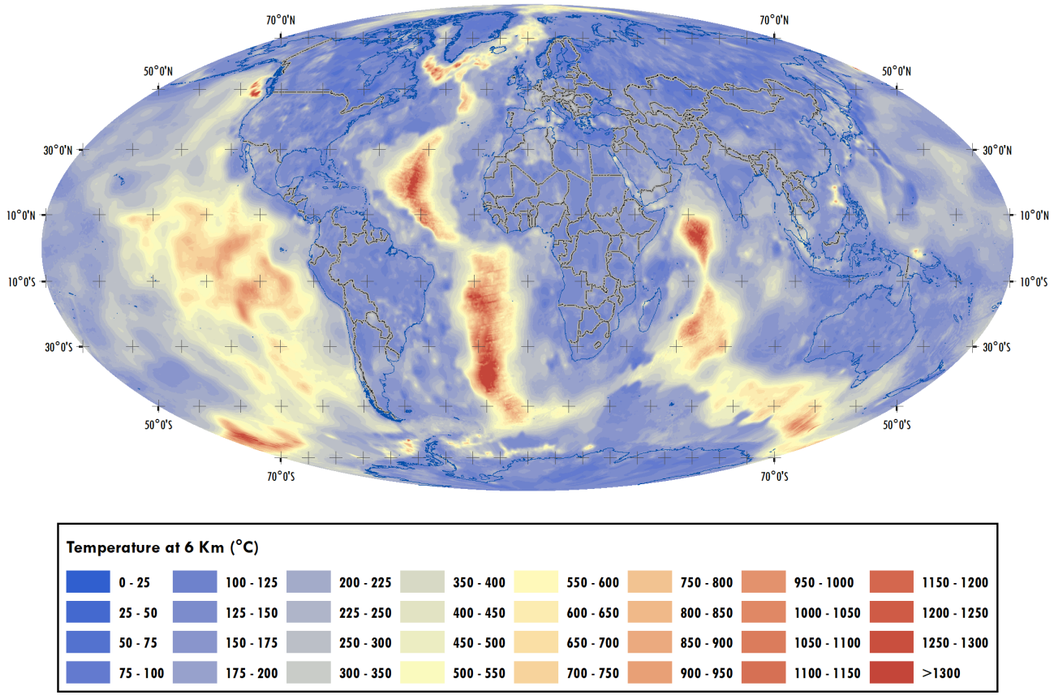

Figure 6.4.4: Temperature at 8 km below surface

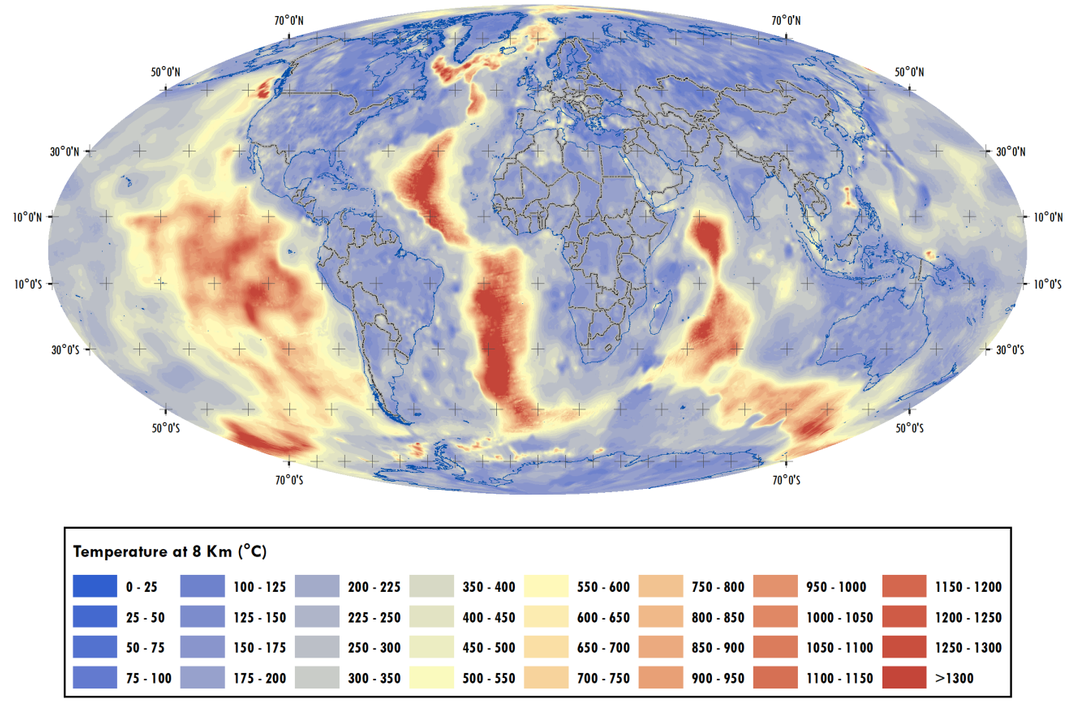

Figure 6.4.5: Temperature at 10 km below surface

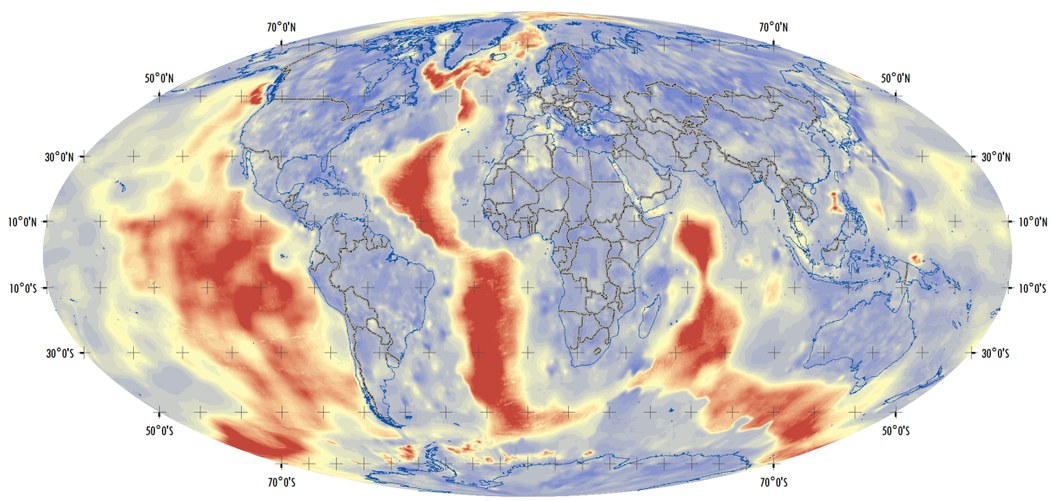

Figure 6.4.6: Temperature at 15 km below surface

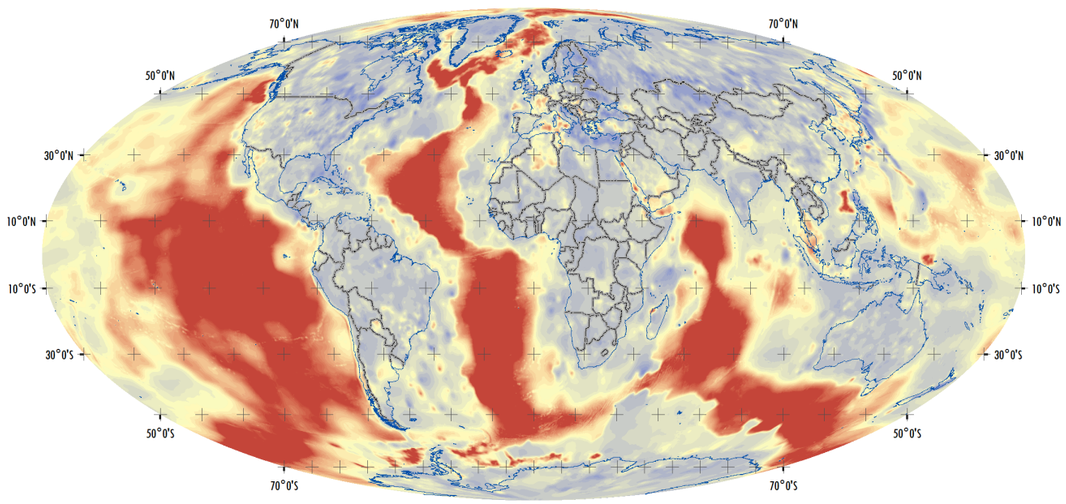

Figure 6.4.7: Temperature at 20 km below surface

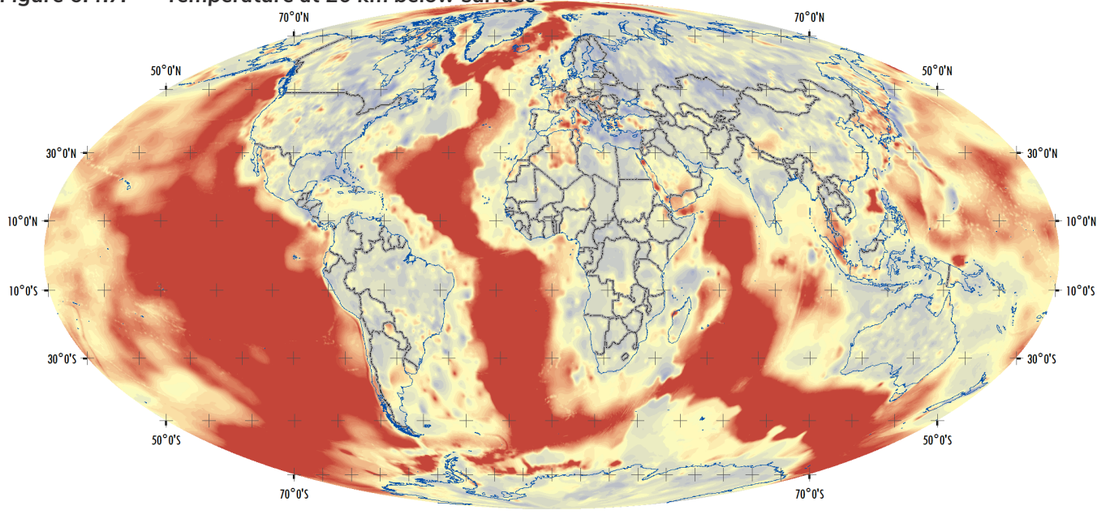

Figure 6.4.8: Temperature at 25 km below surface

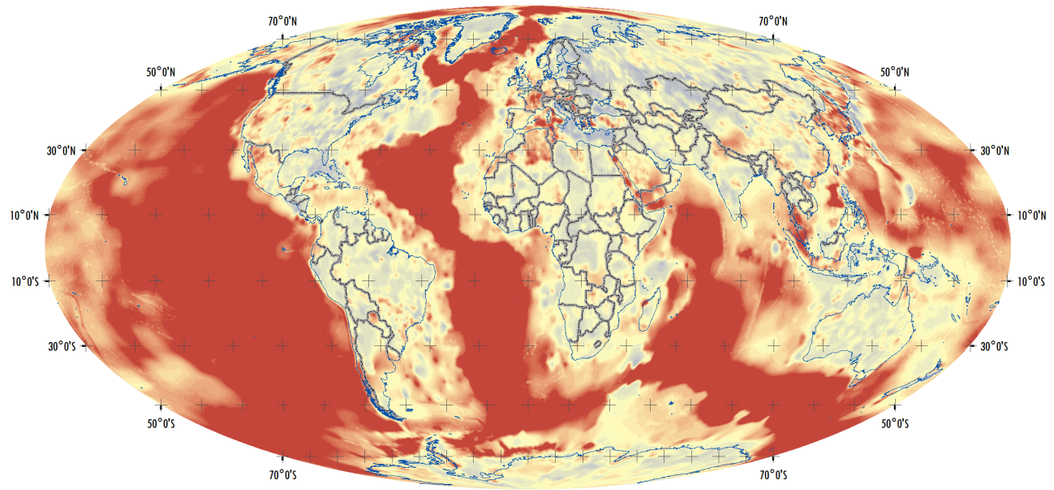

Figure 6.4.9: Temperature at 30 km below surface

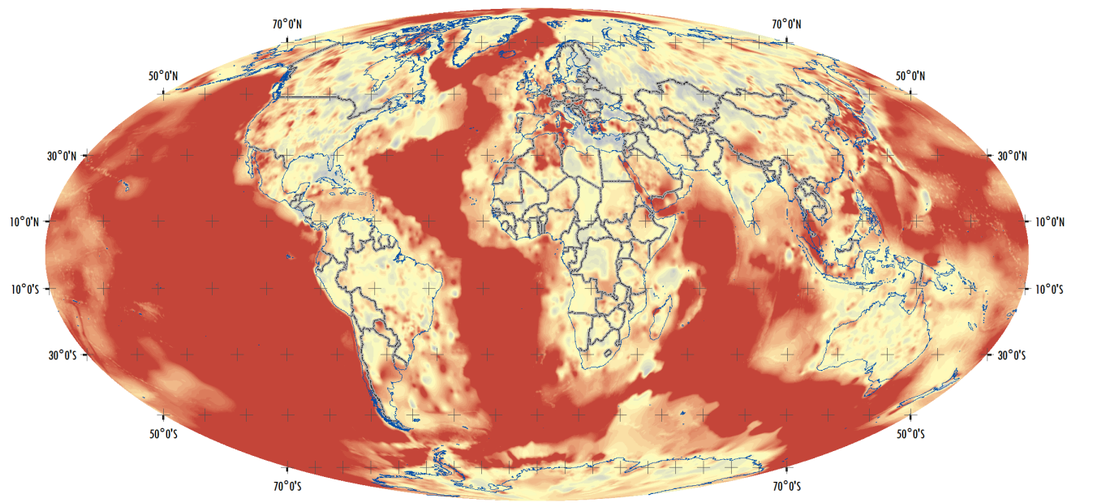

Figure 6.4.10: Temperature at 35 km below surface

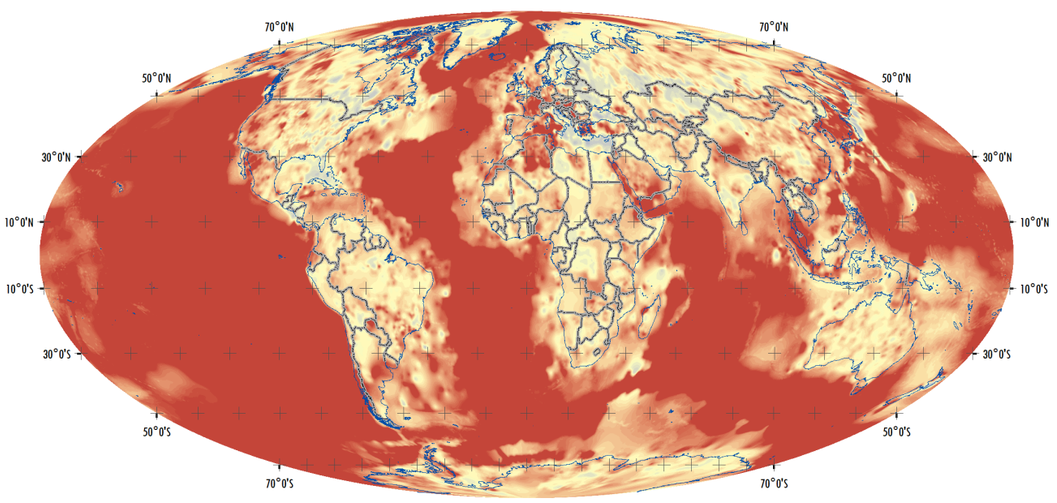

7. Estimating Moho Temperature from Gravity Inversion

7.1 Introduction

Getech's Globe contains several layers where temperature will be one of a number of variables to affect the data. Layers such as topography/bathymetry, sediment thickness and crustal thickness will influence the subsurface heat flow but will not necessarily have a direct relationship with it. The aim of this section of the project was to attempt to use the layers from Globe to produce a proxy data set that has a more direct relationship with temperature. The depth-to-basement and depth-to-Moho layers can be used to build a model of the subsurface, and together with simple density model forward modelled gravity responses can be compared to the observed data.

Assuming the lithosphere-asthenosphere boundary (LAB) as an isotherm of around 1330°C, it is possible to interpret the long-wavelength discrepancies as density variations in the uppermost mantle. Taking pressure into account, and assuming minimal variations in composition, it is possible to interpret these anomalies as temperature variations.

In order to calculate the density of the Upper Mantle, the following layers were used as the input to the 3D inversion (Figure 7.1.1):

- The digital elevation model (DEM)
- Getech's Global Depth-to-Basement model infilled with basement depths from CRUST1.0
- Getech's Global Depth-to-Moho model infilled with Moho depths from CRUST1.0
- The Lithosphere-Asthenosphere boundary (LAB) from LITHO1.0

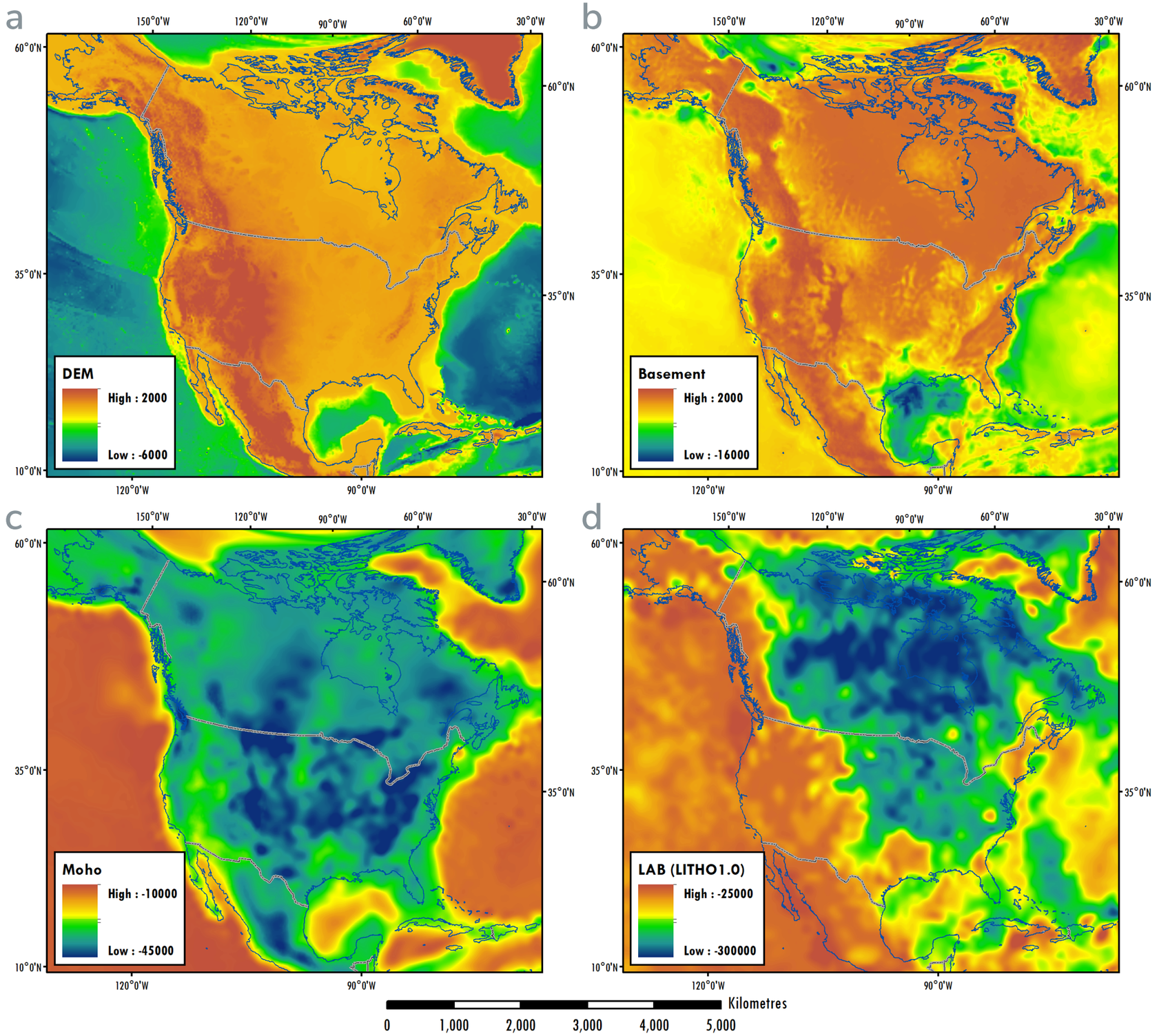

Figure 7.1.1: ***Input data to the inversion for Upper Mantle density. (a) Digital Elevation Model (DEM). (b) Getech's Global Depth-to-Basement. (c) Getech's Global Depth-to-Moho. (d) LAB depths from LITHO1.0***

7.2 Methodology

1. Starting model is produced using the following densities:

- Water = 1.03 g/cm^3
- Sediments = 2.4 g/cm^3
- Continental crust = 2.825 g/cm^3
  - Assumes:
    - Upper continental crust = 2.75 g/cm^3
    - Lower continental crust = 2.9 g/cm^3
- Oceanic crust = 2.9 g/cm^3
- Mantle = 3.3 g/cm^3

2. Calculate the pressure of the layer between the LAB and base of the model (410 km) based on the effect of the overburden (accounting for the differences in the acceleration with depth).

3. Assuming a starting density of 3.3 g/cm^3 and an LAB temperature of 1330°C, calculate the density of this layer between the LAB and the base of the model.

- Kroll et al. (2012) show the thermal expansion coefficient is given by:
  - $$\alpha(T) = (6 \times 10^{-10}T^3 - 2 \times 10^{-6}T^2 + 0.0039T + 1.727) \times 10^{-5}$$
- Bai et al. (2014) show the lithospheric mantle density is affected by thermal expansion by:
  - $$\rho_T = \rho_0[1 - \alpha(T)(T - T_0)]$$
  - ρ_0 = mantle density with normal temperature (T_o) and normal pressure (ρ_0).
  - $\alpha(T)$ = thermal expansion coefficient at temperature, T.

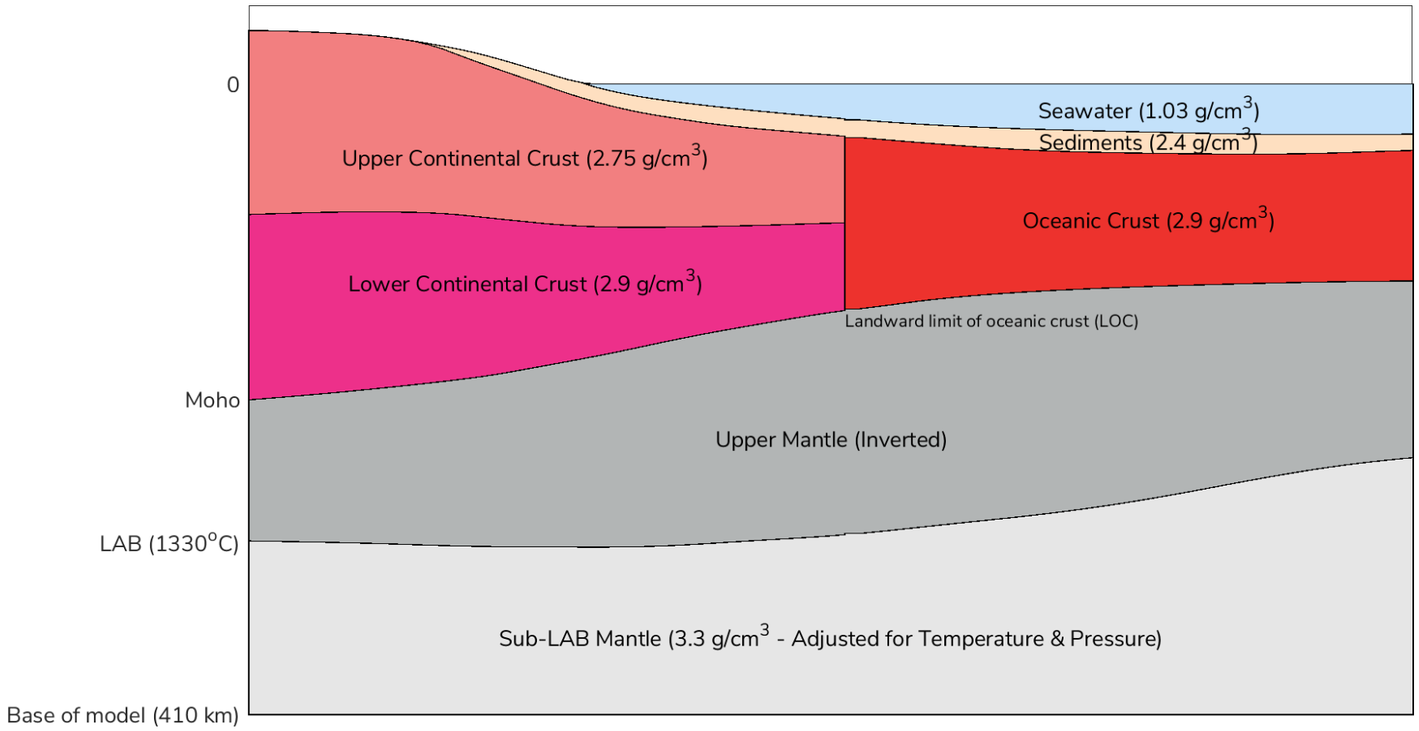

Figure 7.2.1: Schematic illustration of the model set-up

The compressibility coefficient β is the reciprocal of the bulk modulus and is a measure of the relative volume change due to pressure compression. It is affected by temperature by:

$$\beta_T = \frac{1}{(127.97 - 0.0232(T - 300))}$$

The density difference $\Delta\rho_P$ caused by pressure change at temperature, T is:

$$\Delta\rho_P = \rho_0\beta_T[P(z) - P_0]$$

4. Using this layer, the layer above between the Moho and LAB is inverted to minimise data misfits by producing a laterally varying density layer.

5. The pressure at the Moho is calculated and the density effects of this pressure removed from the model.

6. The remaining density anomalies are interpreted as being due to temperature variations, and a temperature map of the upper mantle (below the Moho) produced.

7.3 Results

This approach makes several assumptions, such as a uniform mantle composition, and that the simple density model for sediments and crust is accurate. In reality, density variations caused by these factors are going to lead to anomalous allocations of density in the upper mantle as the inversion attempts to fit the data using the simple model. To mitigate this, only the long wavelength anomalies are analysed, so that short wavelength differences between the modelled and observed data are not interpreted as Upper Mantle anomalies. Once the inverted density layer is corrected for pressure it is interpreted as temperature anomalies and presented in Figure 7.3.1.

The value of this approach, and its usefulness as a deep temperature indicator has been assessed alongside several other proxies for subsurface temperature in a machine learning approach in the following section.

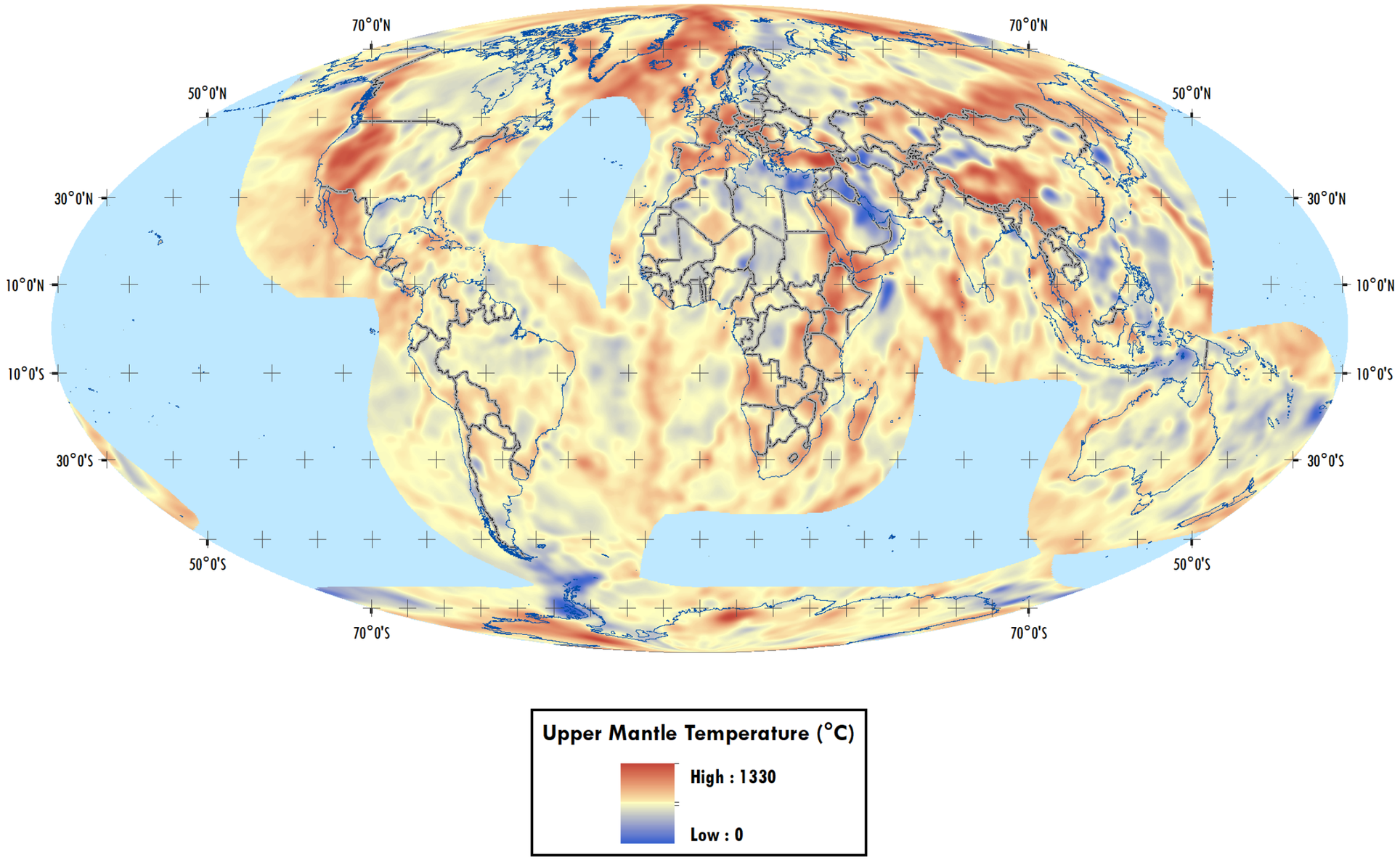

Figure 7.3.1: Upper mantle temperature, based on inversion of gravity data

8. Predicting Surface Heat flow Using Machine Learning Techniques

8.1. Machine Learning: Review of Globe 2020 Work

As part of the Globe 2020 thermal mapping report, we presented some preliminary work using random forest regression machine learning methods to fill in gaps in our heat flow data compilation for the western United States. The random forest method, a version of which is built into ArcGIS Pro, uses decision trees to predict the nature of a data point from a series of explanatory variables. For example, to identify the colour and shape of a symbol (Figure 8.1.1a, below) we can form a decision tree from a random subset of its properties, features such as size, colour, line weight, height. In the left and right trees, the small green diamond is correctly identified from useful properties such as size, shape and colour. In the central tree and incorrect prediction is made as variables such as height and line weight are used. By generating a forest of hundreds of decision trees, we can overcome the limitations as the average or majority prediction wins. This method is covered in more detail in the Globe 2020 report.

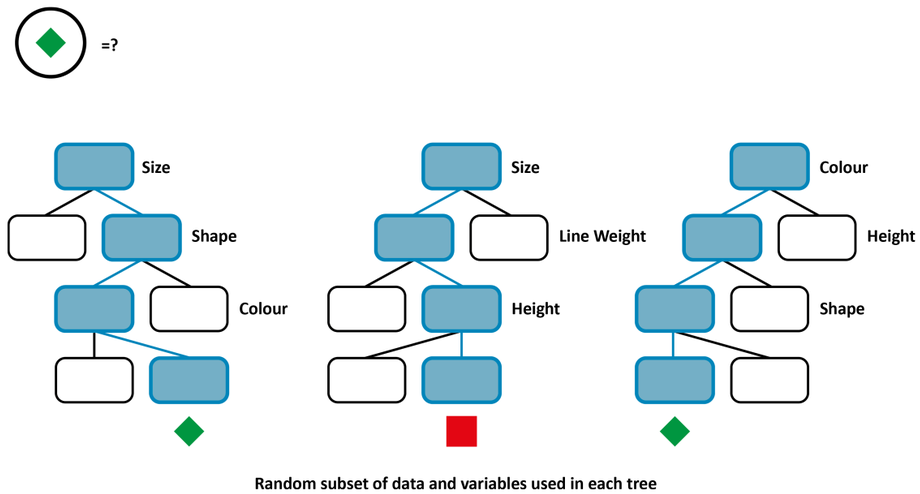

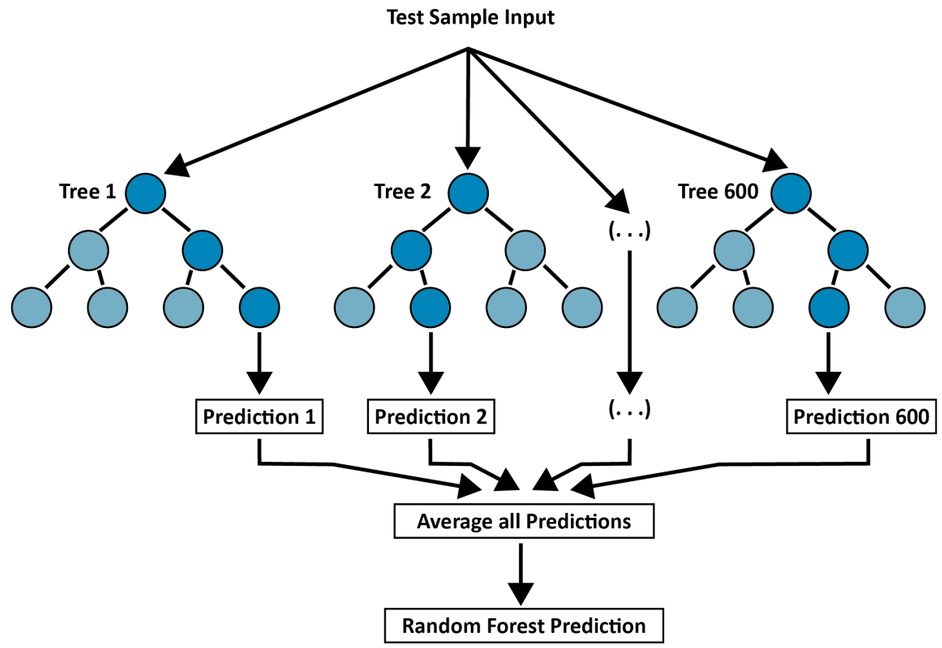

Figure 8.1.1: How multiple decision trees allow the random forest algorithm to make a prediction for each data put input. a). Three trees with three tiers, each assigned different variables randomly. Note how a tree given relatively unhelpful (centre) explanatory variables does not arrive at an accurate prediction, b). Using hundreds of trees helps to eliminate bias, establish the most useful explanatory variables, and make accurate predictions.

Getech's interpreted heat flow database (orange points) shows heat flow measurements on a 0.25° grid, and for the western United States has a very high density of points. The western United States also has a wide array of high-quality explanatory variables, so made an ideal test ground for the random forest machine learning method. We set out to predict heat flow values for locations where no data are present (small dots). We trained the random forest algorithm using explanatory variables such as depth-to-basement, depth-to-Moho, distance to nearest volcano, Pn velocity from US array data (a proxy for Moho temperature), and Curie Temperature Depth. After training, the same model was tested using a portion of the real data reserved for testing, then used to predict heat flow at each point on the 0.25° grid.

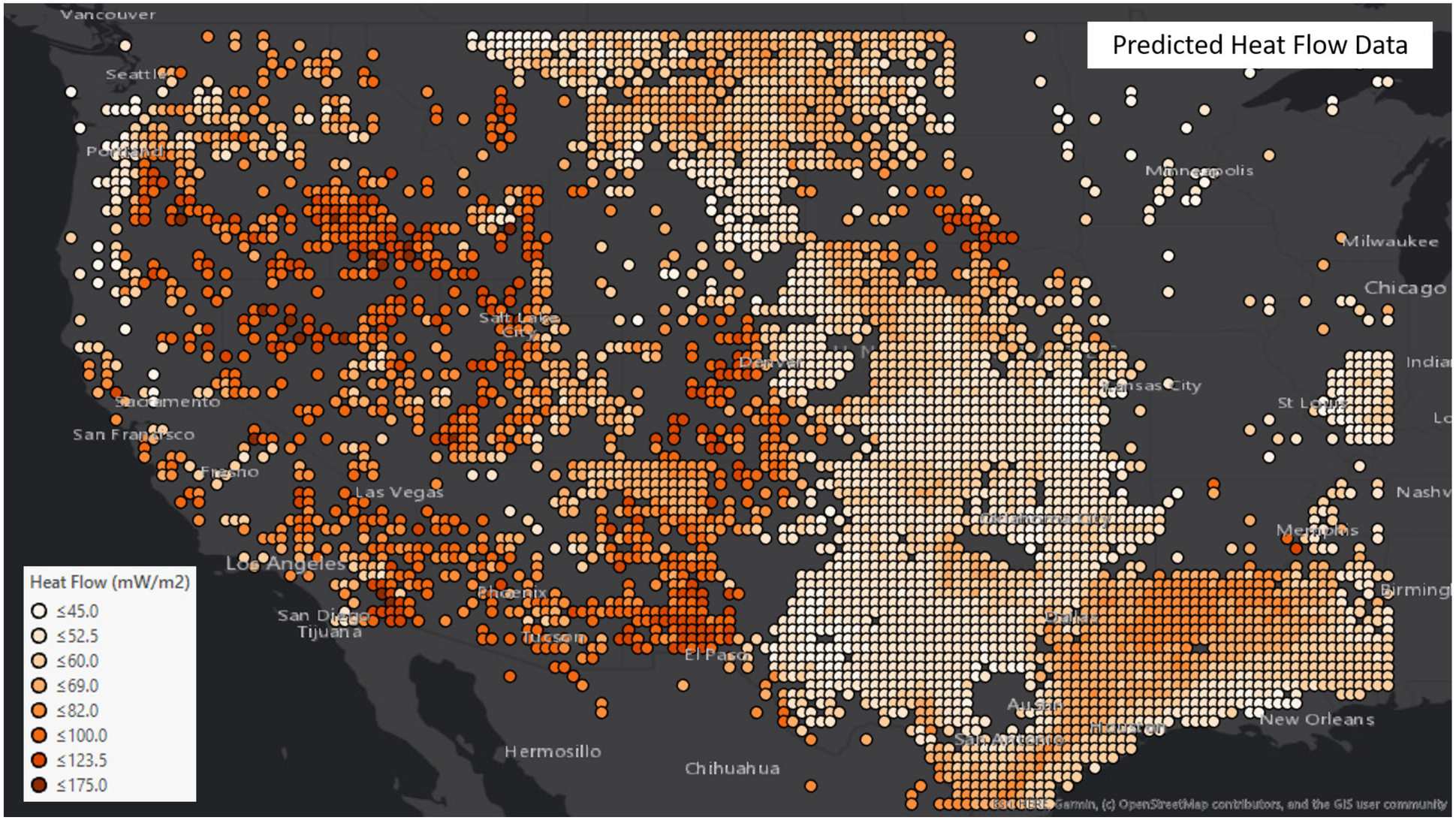

Figure 8.1.2: Filling gaps in a geospatial data set, in this example from central and western United States. Shades of orange are a measured continuous variable sampled on a 0.25-degree grid. Small blue dots are locations with explanatory variables but no measurements of the continuous variable and potential to be predicted.

The results of applying the random forest method are shown below. Some simple statistics are provided by the algorithm to help assess the result. The predictions for the retained testing data were found to be correlated to the known values with an R-squared value of 0.6. For the 2021 product, we aimed to expand upon this analysis, test further methods and find additional diagnostics to validate the result. In this section of the report, we present global results for predicting heat flow from random forest classification and regression techniques, and repeat the analysis of temperature with depth with this new global heat flow data set.

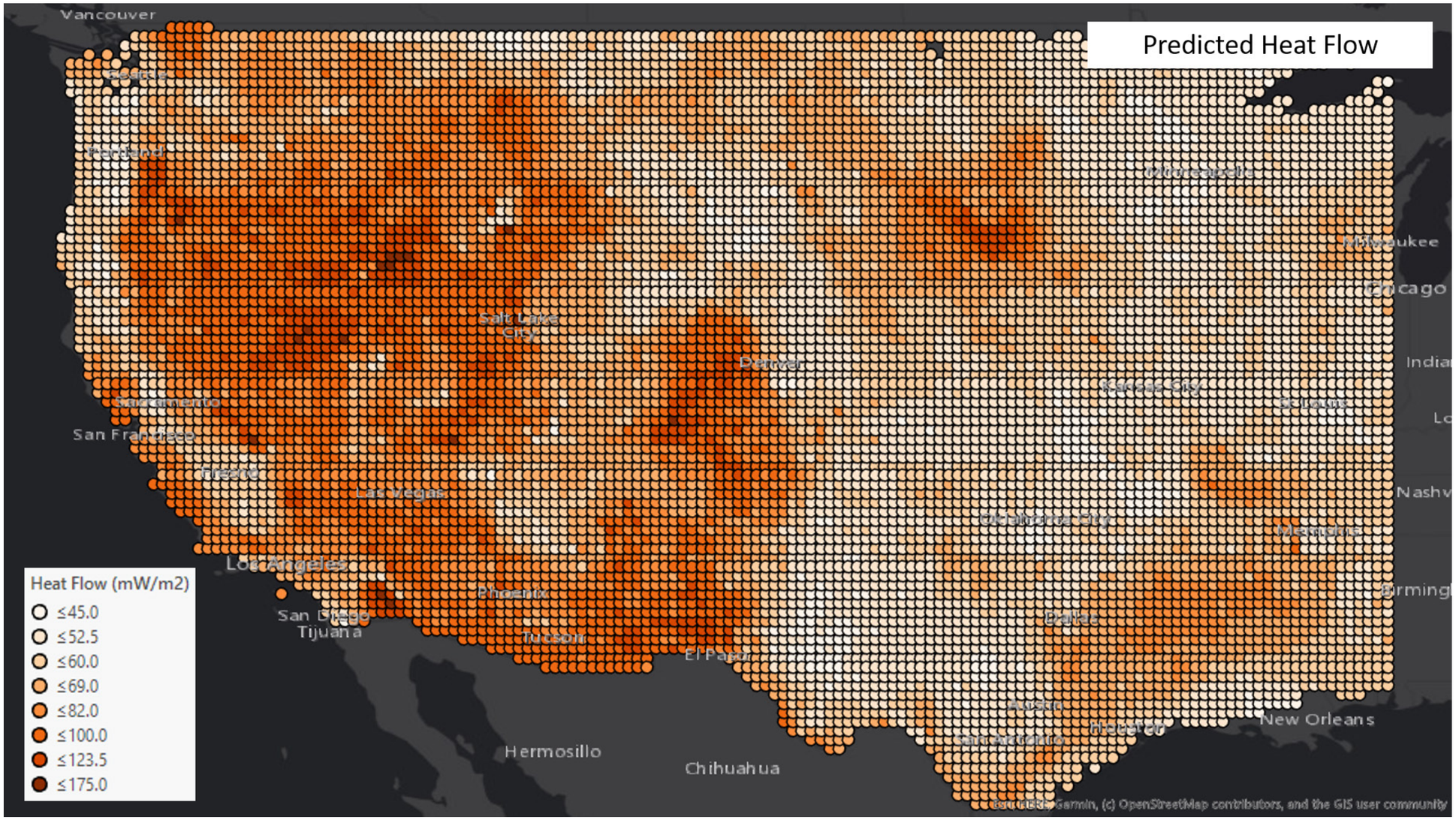

Figure 8.1.3: Predicted heat flow values from the random forest regression model.

8.2. Machine Learning: Classification Problem

As part of the Globe 2020 thermal mapping report, we presented a machine learning method for filling gaps in the North American heat flow database using the random forest method in ArcGIS Pro. This method used proxy data and the actual surface heat flow data to train a model to predict the known data, which then, after fitting the real data, to predict in areas where the proxy data are known but the heat flow data are unknown. This method proved effective, but issues on the accuracy and validity of the method were clear. For this 2021 release of Globe, we have further investigated this method and expanded the work to all continental areas of the globe. This presentation is intended to explain the methods and particularly focuses on validating the prediction to provide the user with an understanding of the quality but also the limitations of the predictions.

In this first section, we treat the heat flow prediction as a classification problem. This method considerably simplifies the problem by grouping the measured heat flow into five grades, A to E, with A being the highest heat flow values and E being the lowest. The advantage here is that the random forest algorithm in classification mode allows for additional diagnostics, which can be used to understand the accuracy and precision of the models which should also be similar for the regression problem. The negative side of this approach is that generalised categories may not be so useful for assessing temperature/time conditions in petroleum exploration, as exact heat flow values are not predicted. In geothermal exploration, identifying anomalously high heat flow locations could be useful, and as such, this classification problem might be an ideal solution.

We graded the heat flow values on an A-E scale according to a five category natural breaks method in ArcGIS.

Categorising the data in this way:

- Simplifies the machine learning problem and allows access to further diagnostics
- Should prove beneficial for geothermal exploration, where high heat flow areas are key targets
- May not be so useful for petroleum exploration where time is a key component as well as heat flow

By using a random forest algorithm in categorisation mode rather than a regression model (see Thermal Mapping 2020 report) we can access further diagnostics to assess how well a model can predict a category rather than attempt to produce an accurate value.

This method allows us to produce a confusion matrix, which, for the training data, plots the model predicted category against the true category. We can see how often the model predicts the correct category and how often the model is incorrect and how far off it is.

Grade	Range
E	<53.9 mW.m^{-2}
D	54.0 - 65.4 mW.m^{-2}
C	65.5-79.5 mW.m^{-2}
B	79.6 - 98.8 mW.m^{-2}
A	>98.9 mW.m^{-2}

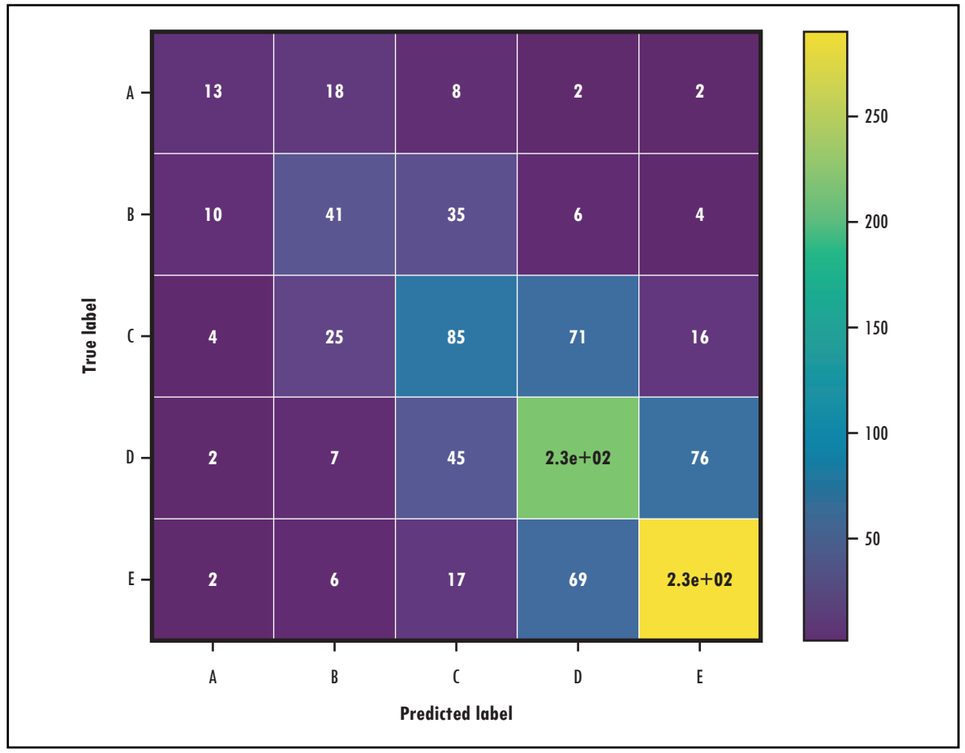

Figure 8.2.1: ***Example confusion matrix for a five-category classification. The vertical axis show the 'true' category of the data, and the horizontal axis shows the model predicted category.***

Validating the Random Forest method by grouping heat flow measurements into Categories.

The confusion matrix (left) compares the predicted heat flow category (x-axis) with the actual heat flow category (y-axis). For a perfect prediction, all values would lie along the central axis of the matrix.

In this example, heat flows in categories D and E are generally predicted very well, whilst the higher categories are predicted less well.

This example is for our real heat flow data set, so it is worth noting that, in machine learning terminology, this is an unbalanced data set (there are more measurements in categories D and E than categories A, B, and C). This can often lead to the densely populated categories being over predicted.

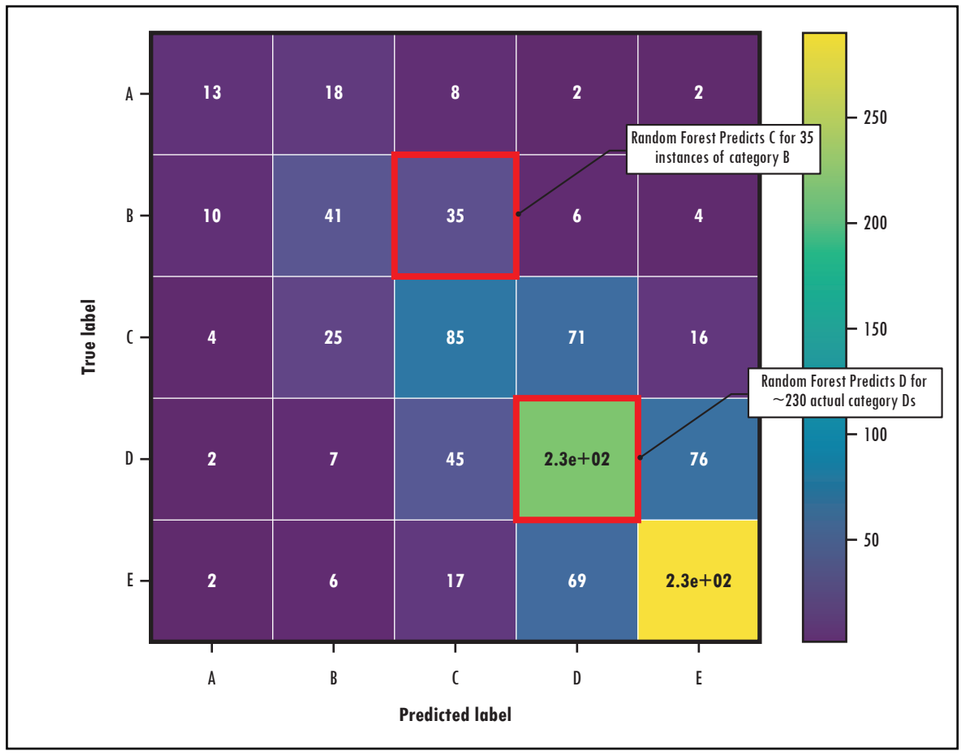

Figure 8.2.2: ***Reading the confusion matrix. Along the diagonal the model predicts the true category accurately. Values off the diagonal are where the model makes an incorrect prediction.***

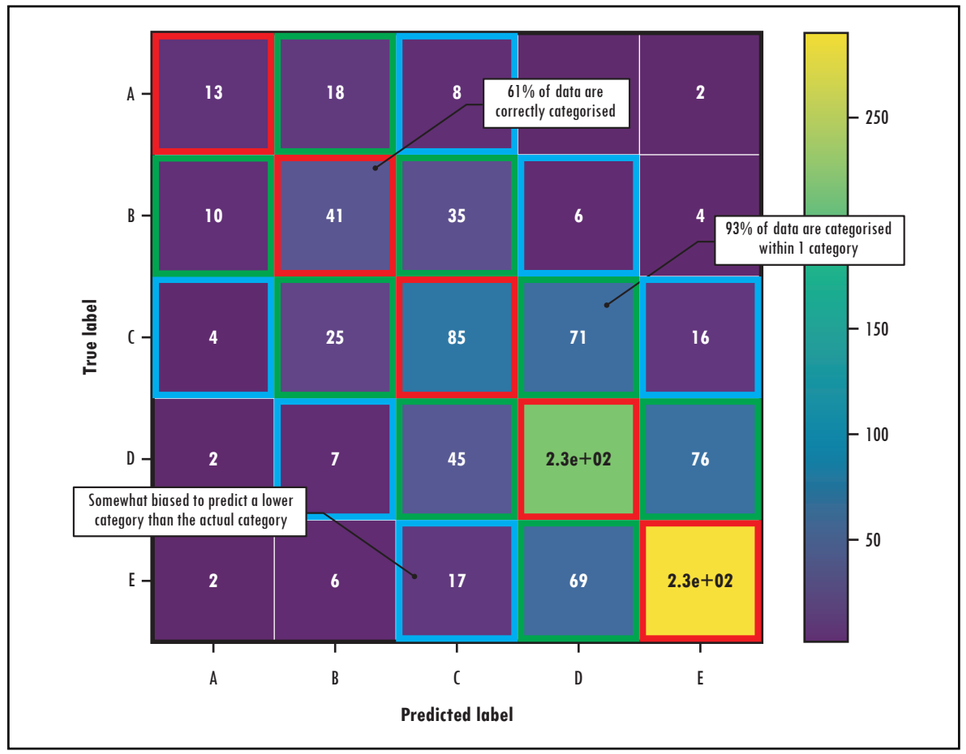

Figure 8.2.3: ***Reading the confusion matrix. Along the diagonal the model predicts the true category accurately. Values off the diagonal are where the model makes an incorrect prediction.***

Interpreting the confusion matrix

Along the main diagonal of the matrix (highlighted in red) our random forest classification model correctly predicts the category of that data point. The next diagonal (highlighted in green) are locations where the prediction is out by one category.

- 61% of data are correctly categorised
- 93% of data are categorised within 1 category
- Somewhat biased to predict a lower category than the actual category

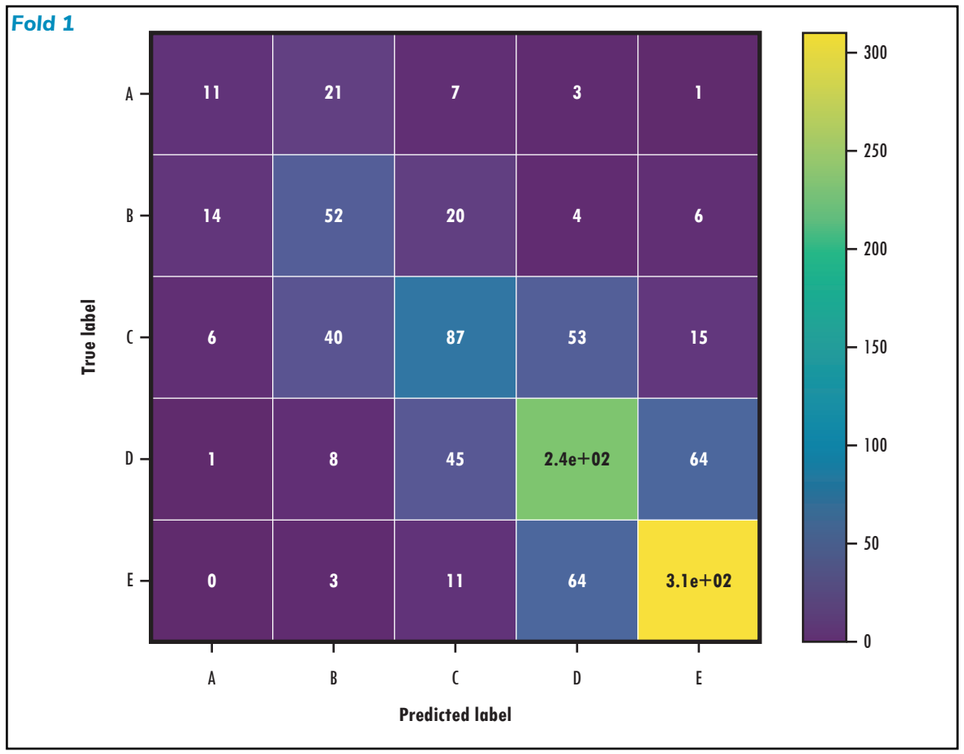

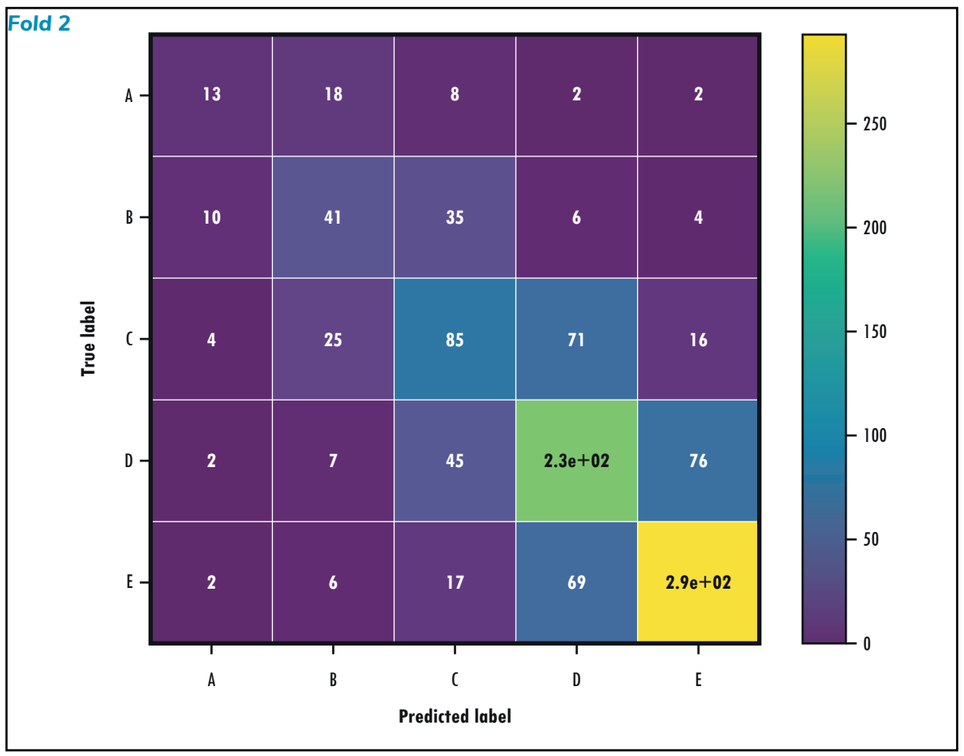

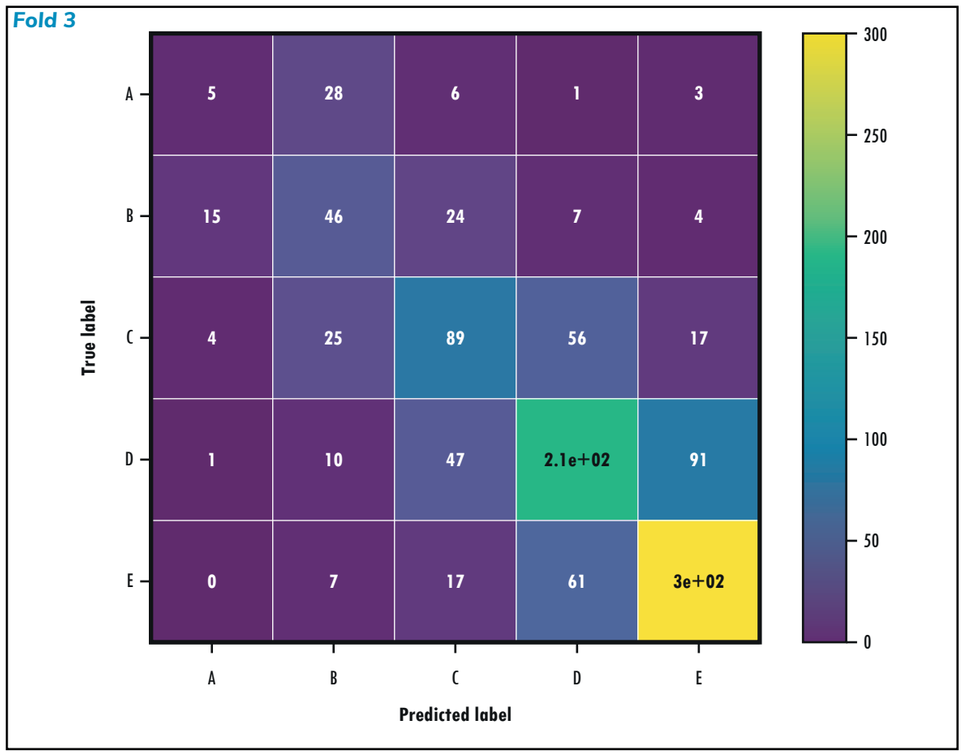

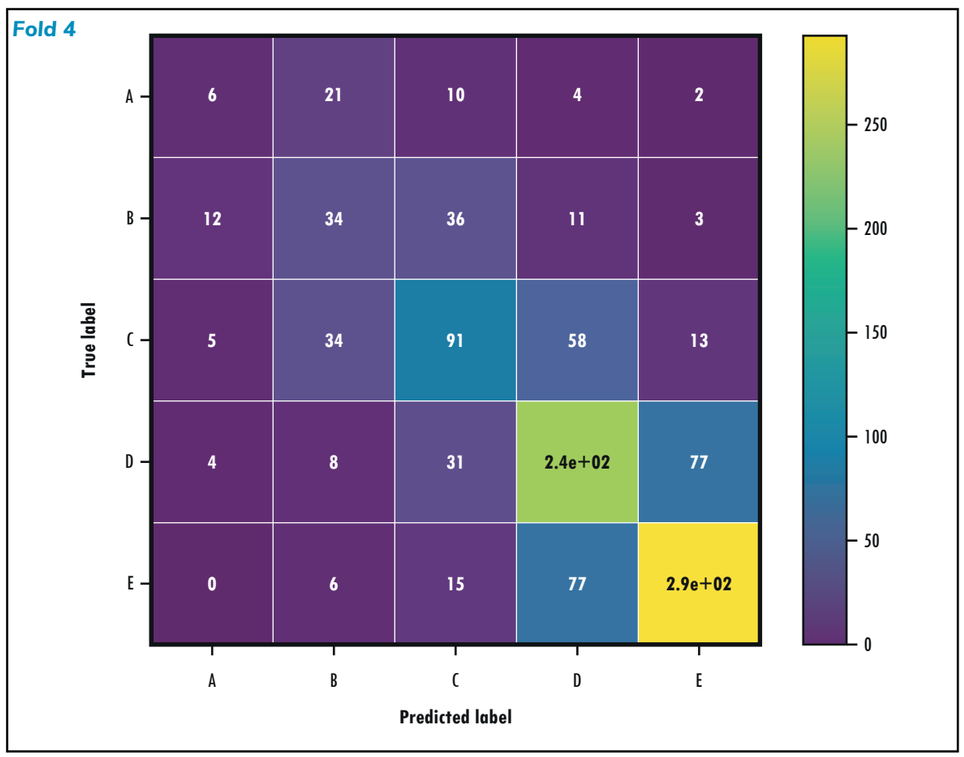

Evaluating with the k-fold technique.

The k-fold technique repeats an analysis k times with a different 1/kth of the data reserved for testing in each instance. When k=4, the data set is divided into four quarters, with three used for training and one for testing. The experiment is repeated four times so each quarter is reserved for testing once.

Each fold produces a unique random forest algorithm with its own diagnostics. Here we compare the confusion matrices for four folds using the example from the previous slides.

We see broadly similar patterns for each fold, suggesting that the model is fairly robust and the metrics are reliable.

Data sets of this type are known as unbalanced data set. Categories C, D and E have more data points in those categories than A and B. Consequently, these categories may be better predicted as there are more training data.

Figure 8.2.4: Confusion matrices for the four folds evaluating the same data set.

Working with unbalanced data sets

Some additional metrics are available to assess the classification model, which are useful in this case as we've seen that the number of data points in each category is inconsistent. By assessing the metrics category by category, we can understand how the model deals with individual categories, particularly useful where, in the case of geothermal exploration, we may be most interested in the high value (category A) heat flows.

- Positive result – the algorithm correctly predicts the category in the real data.
- Precision - the number of positive results divided by the total number of predictions calculated independently for each class.
- Recall - the number of positive results divided by the number of actual calculated independently for each class.
- F1 Score – 2 x (precision x recall) / (precision + recall).
- Support – number of samples in a given category.

Table 8.2.2 below shows some advanced metrics for the classification case shown on previous slides. It further demonstrates the unbalanced nature of the data we are working with. Categories D and E are better predicted, perhaps owing to the fact there are more samples to train on in these categories.

- Positive result – the algorithm correctly predicts the category in the real data.
- Precision - the number of positive results divided by the total number of predictions calculated independently for each class.
- Recall - the number of positive results divided by the number of actual calculated independently for each class.
- F1 Score – 2 x (precision x recall) / (precision + recall).
- Support – number of samples in a given category.

	Precision	Recall	F1-score	Support
A	0.32	0.26	0.29	43
B	0.41	0.53	0.46	96
C	0.50	0.43	0.46	201
D	0.66	0.67	0.66	363
E	0.78	0.79	0.79	385
Accuracy			0.64	1088
Macro Ave	0.54	0.54	0.53	1088
Weighted Ave	0.54	0.64	0.64	1088

Table 8.2.2: ***Precision and recall metrics for the four fold random forest classification problem.***

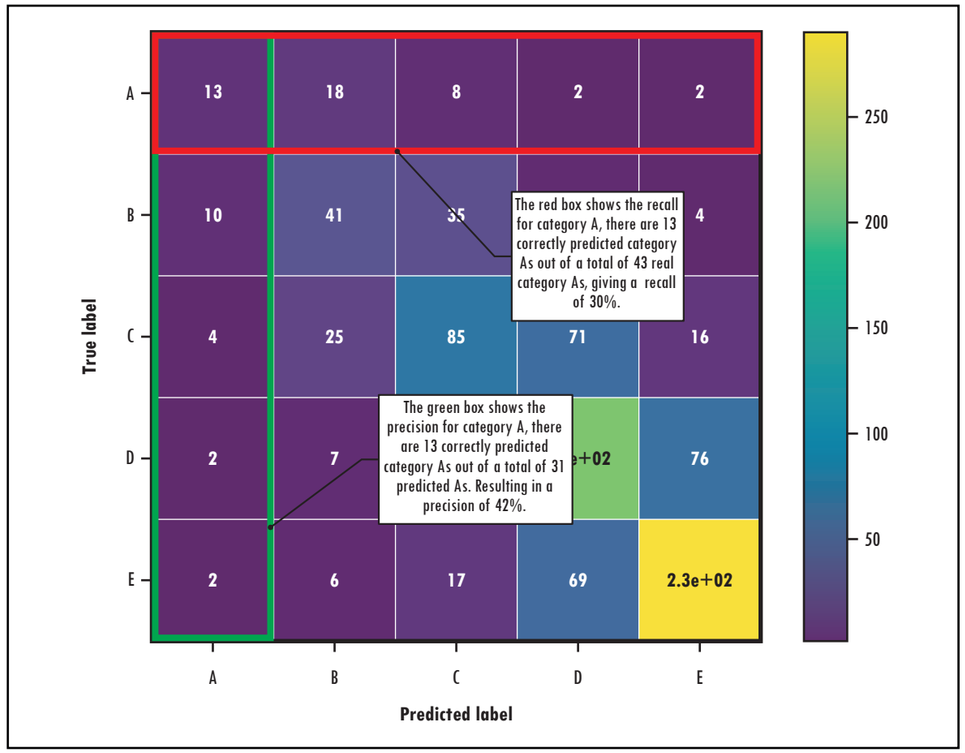

Figure 8.2.5: ***Precision and recall example on the five class confusion matrix.***

The green box shows the precision for category A, there are 13 correctly predicted category As out of a total of 31 predicted As. Resulting in a precision of 42%.

The red box shows the recall for category A, there are 13 correctly predicted category As out of a total of 43 real category As, giving a recall of 30%.

8.3. Machine Learning: Regression Problem

By treating the heat flow prediction model as a classification problem, we showed that it is possible to predict heat flow given proxy data (crustal thickness, crustal type and depths to discontinuities such as Moho and lithosphere-asthenosphere boundary). We also have a sense of the quality of that prediction with >60 % of data points being correctly predicted and >90% of points falling within one category. Whilst this method has some advantages, identifying areas of anomalously high heat flow for geothermal exploration, for example, categorising heat flow may not be applicable for petroleum exploration. The analysis does give us some confidence in the quality of the regression prediction; the Globe 2020 report presented a 'headline accuracy' (the r^2 value for the testing subset of the data) number for each trial model, but limited further options for analysis. The regression problem will provide estimates of the heat flow, rather than just a categorisation, but by using similar parameters to the classification problem we have a better understanding of the quality of the result. (I. Kakadiaris, pers com. 2021)

For the regression problem, we generated one database of heat flow measurements (Getech's 2020 interpreted heat flow database) and sampled the value for each of the explanatory (proxy) variables (see next slide) at each location; this is our training data. To make predictions, we generate a second grid of explanatory variables, on a regular 0.25° grid, regardless of whether there is a heat flow measurement or not. Once the model is trained, this allows for a prediction at all locations where the explanatory variables are present. We experimented with upwards of 20 combinations of training data to generate our preferred models. In the following section, we present the results from a complete, global model where all available data are used to train the model and then predict across the globe on a 0.25° grid. We also predict 'continent by continent', training a unique model for each continent based upon the data located on that continent and often supplemented with relevant data from continents with a similar crustal architecture. Our preferred model is a mosaic of these continent-by-continent predictions and is also covered in the following slides.

In our preliminary work on random forest modelling (Globe 2020), we identified a number of variables we could use to predict heat flow (this work was solely focussed on the Western United States, where USArray data was available). Using the results from last year, we selected variables which:

- Are available globally
- Were useful in the random forest algorithm during the preliminary investigations last year
- Do not conflict with each other (e.g. two instances of depth-to-basement from different sources)

Column	Data	Type	Explanation	Unit
1	ObjectID	Integer		
2	Shape	Geometry		
3	Continent	Text		
4	Crustal Type	Text	Categorical variable indicating the composition of the crust	
5	CTD_SMag	Float	Curie temperature depth calculated from satellite magnetic data	km
6	CTD_TMag	Float	Curie temperature depth calculated from terrestrial magnetic data	km
7	D2B_SeaLevel	Float	Depth to basement relative to sea level	km
8	D2M_SeaLevel	Float	Depth to Moho relative to sea-level	km
9	CThick	Float	Crustal thickness from basement to Moho	km
10	SThick	Float	Sedimentary thickness	km
11	Topo	Float	Topography	km
12	MohoT	Float	Temperature at Moho	°C
13	D2LAB	Float	Depth to lithosphere-asthenosphere boundary	km
14	LAB Vp	Float	P-wave velocity at the lithosphere-asthenosphere boundary	ms^{-1}
15	LAB Vs	Float	S-wave velocity at the lithosphere-asthenosphere boundary	ms^{-1}
16	POINT_X	Float	Longitude	degrees
17	POINT_Y	Float	Latitude	degrees

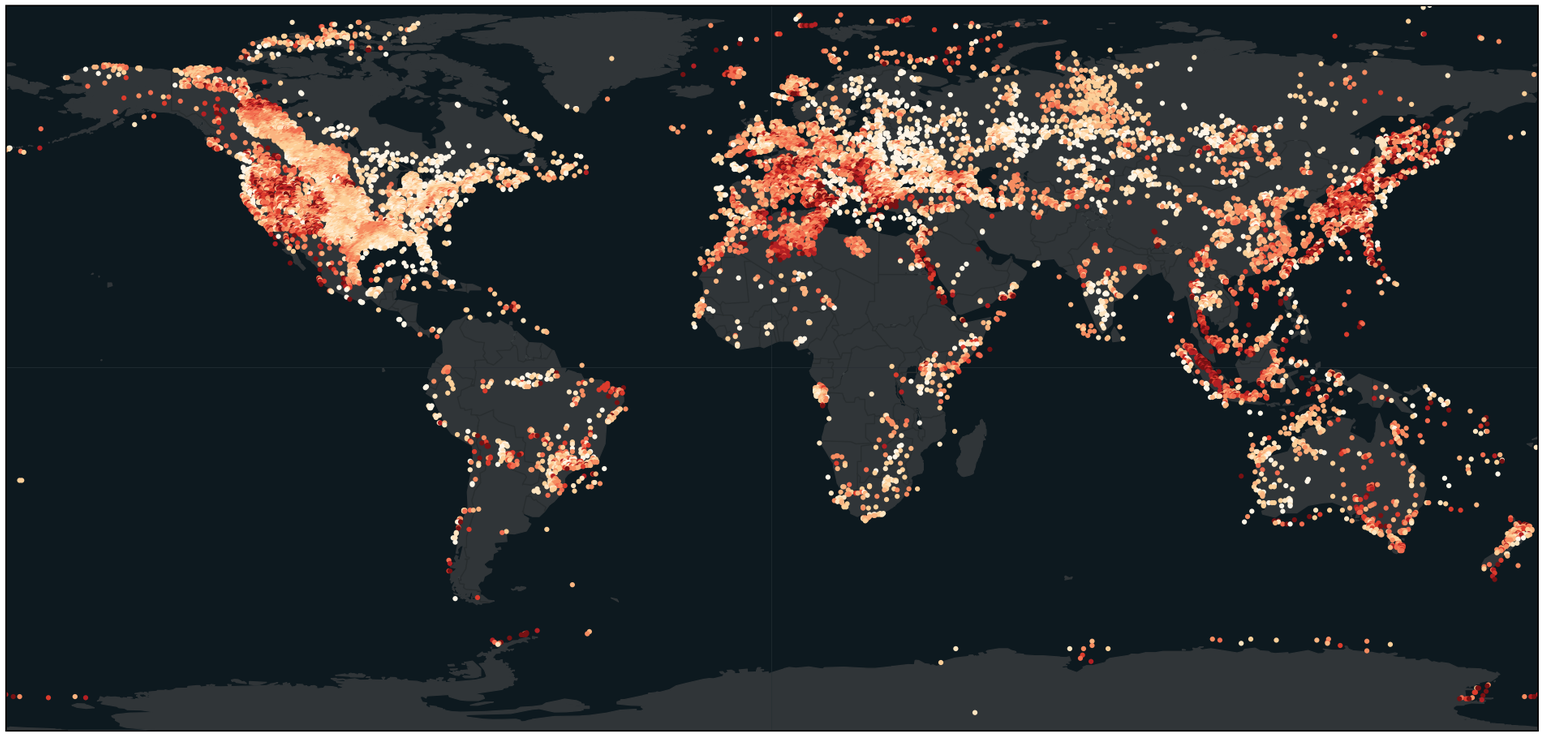

Figure 8.3.1a: Training data (heatflow measurements) from Getech's interpreted heat flow database, shown on global extent.

The actual (Figure 8.3.1a) and trained (Figure 8.3.1b) data for Model 020. Measurements taken from Getech's interpreted heat flow database and symbolised using a 9-class method with roughly an even number of records in each class.

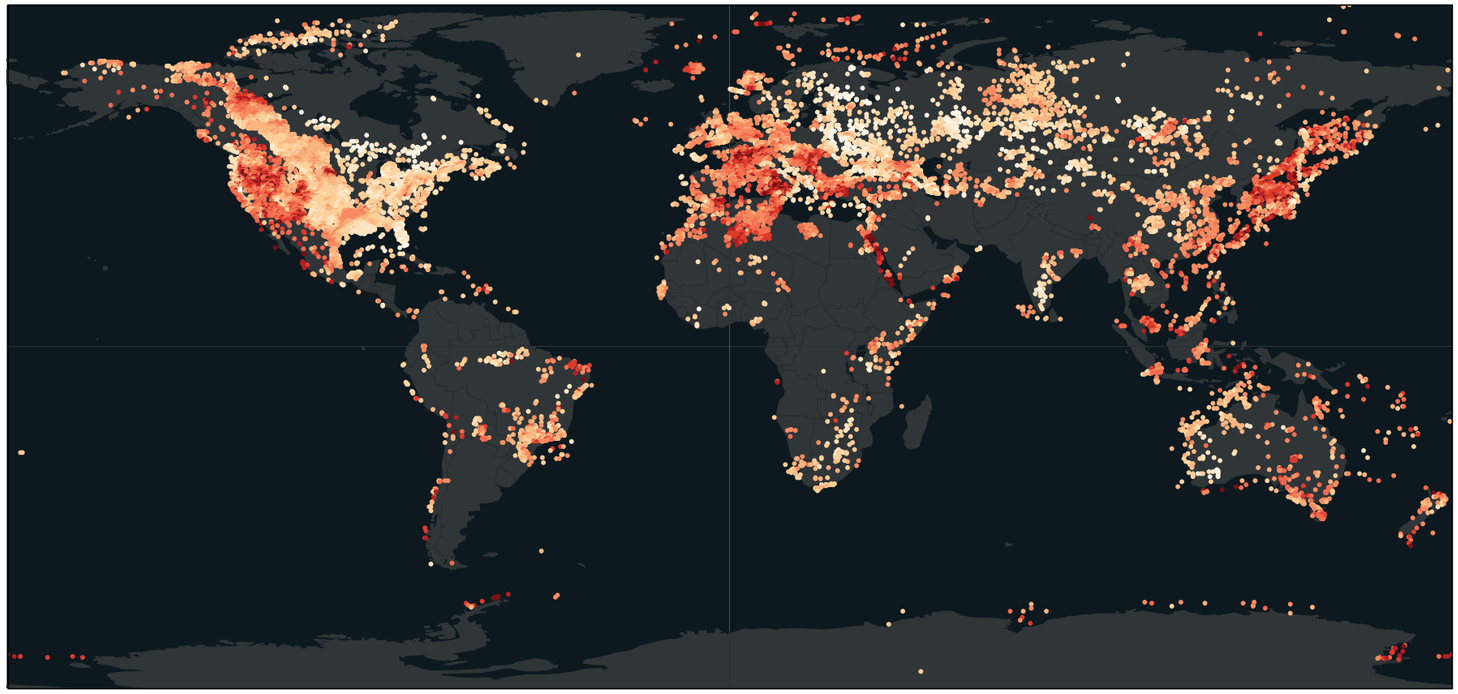

Figure 8.3.1b (below): Random forest regression predicted heat flow for the same set of points (trained data).

Global Extent

The signed error (residual error) is calculated by subtracting the random forest prediction from the observed heat flow. This slide shows the signed error for the global train and test data. Red points are underpredictions by the algorithm and blue points are overpredictions of the algorithm.

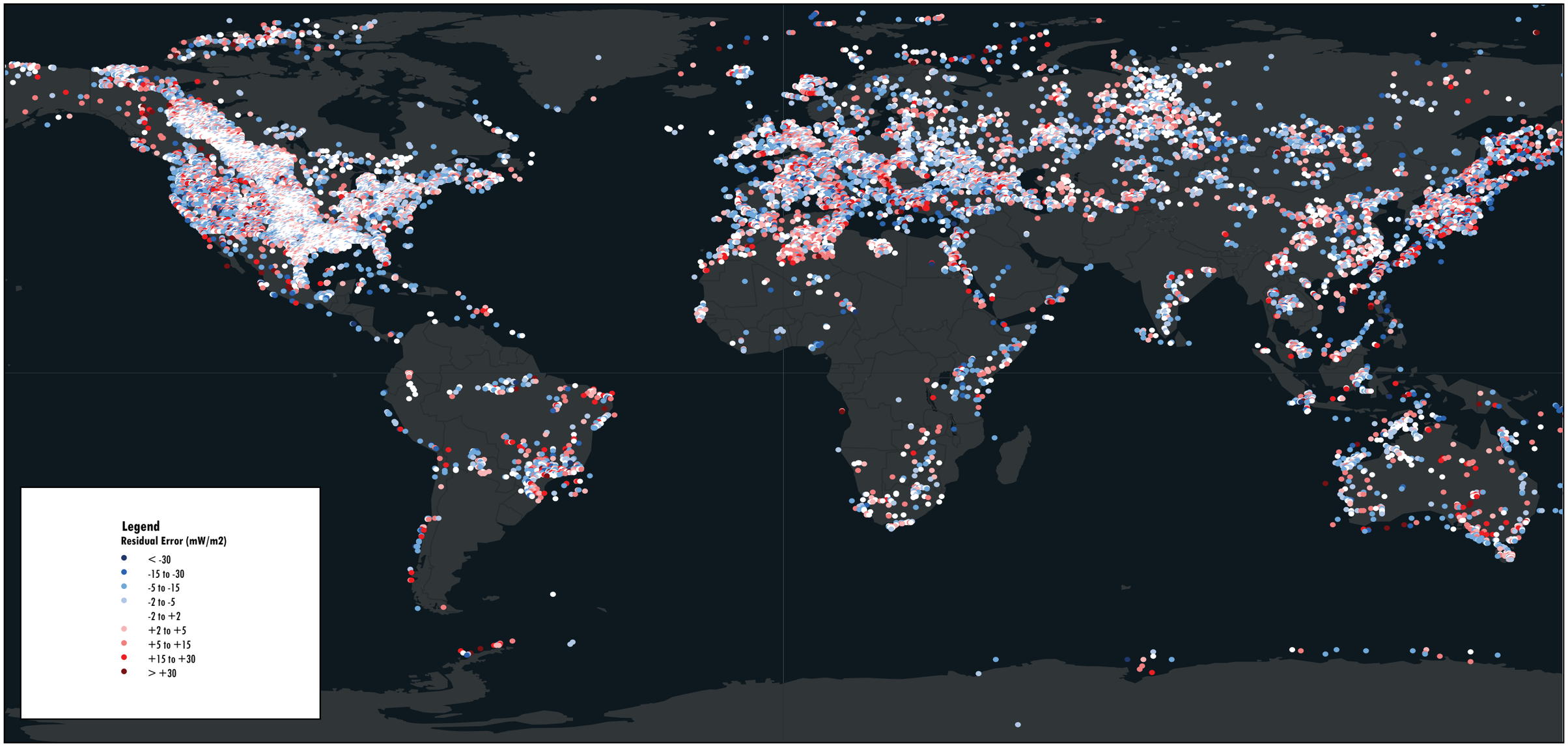

Figure 8.3.2. Residual error for the trained data.

Global Extent

Figure 8.3.3 below shows the global prediction data from model 020, which is the model trained on all global heat flow measurements and predicted globally on a 0.25° grid. Points are displayed using the same colour ramp as the training data. The prediction is somewhat conservative and predicts fewer extreme high and low values, so the colour scale is less saturated than in Figure 8.3.1.

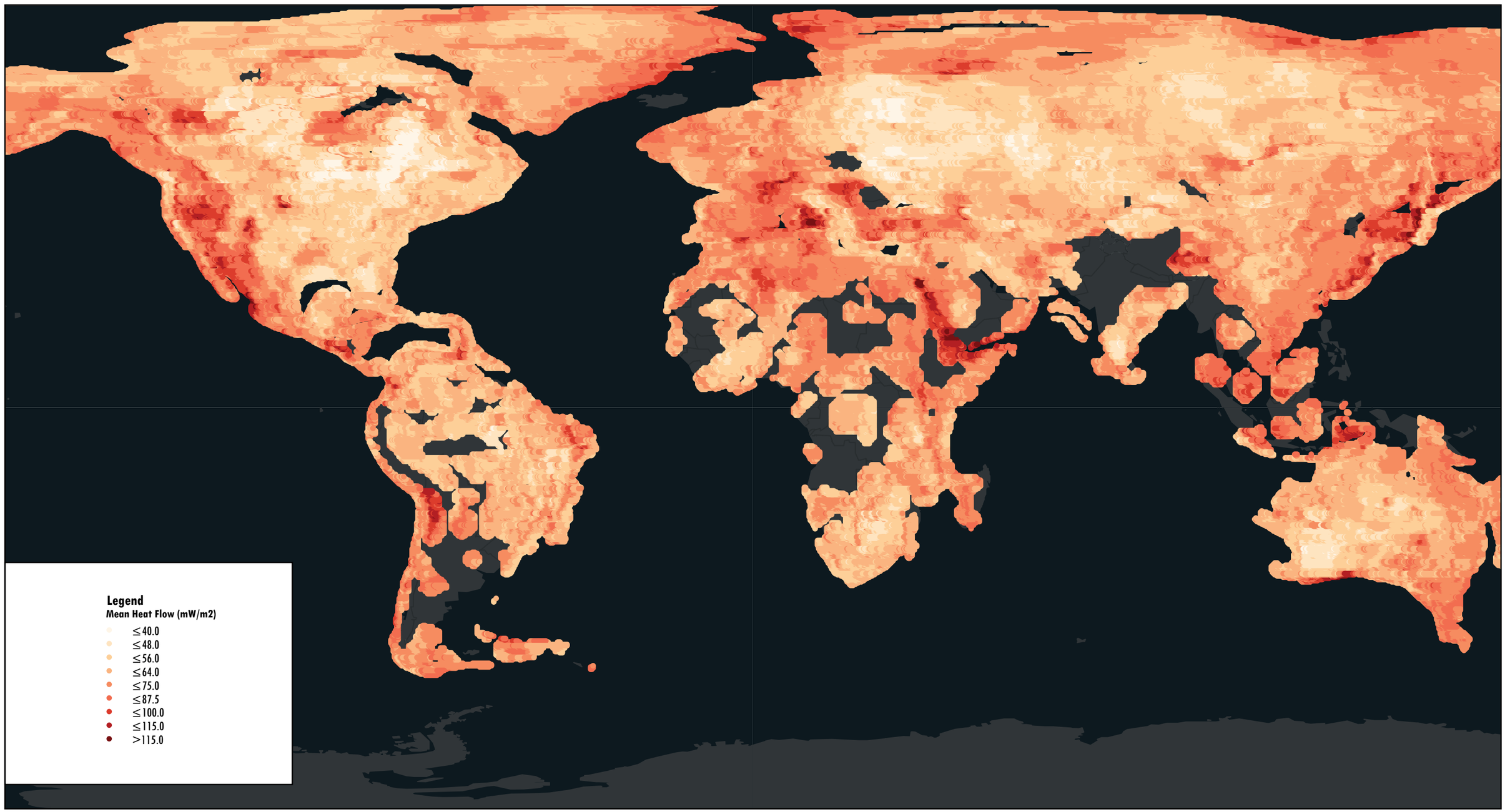

Figure 8.3.3. Random forest predictions of heat flow, displayed globally and calculated using all available heat flow data for training and testing the algorithm

Global Extent

A second global prediction, this model combines our preferred results for the continent by continent random forest models (displayed on upcoming slides). Each continent is treated individually, with local heat flow measurements used for training, for continents with sparser data, the local data is supplemented with additional data for a continent with similar crustal make up. The preferred model for each continent is used to predict heat flow on a 0.25° grid for that continent.

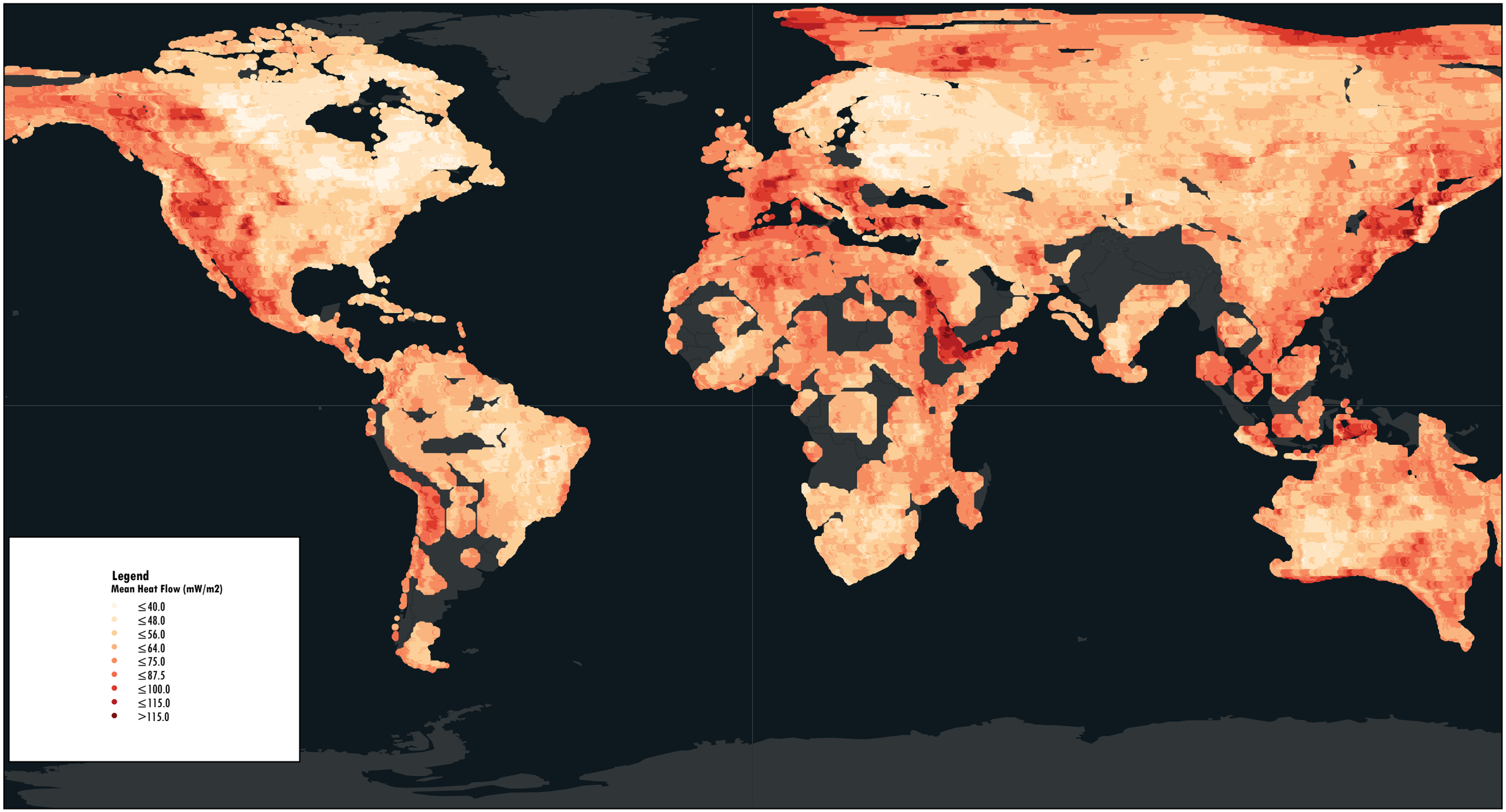

Figure 8.3.4. Random forest predictions of heat flow, displayed globally but compiled from continent by continent predictions.

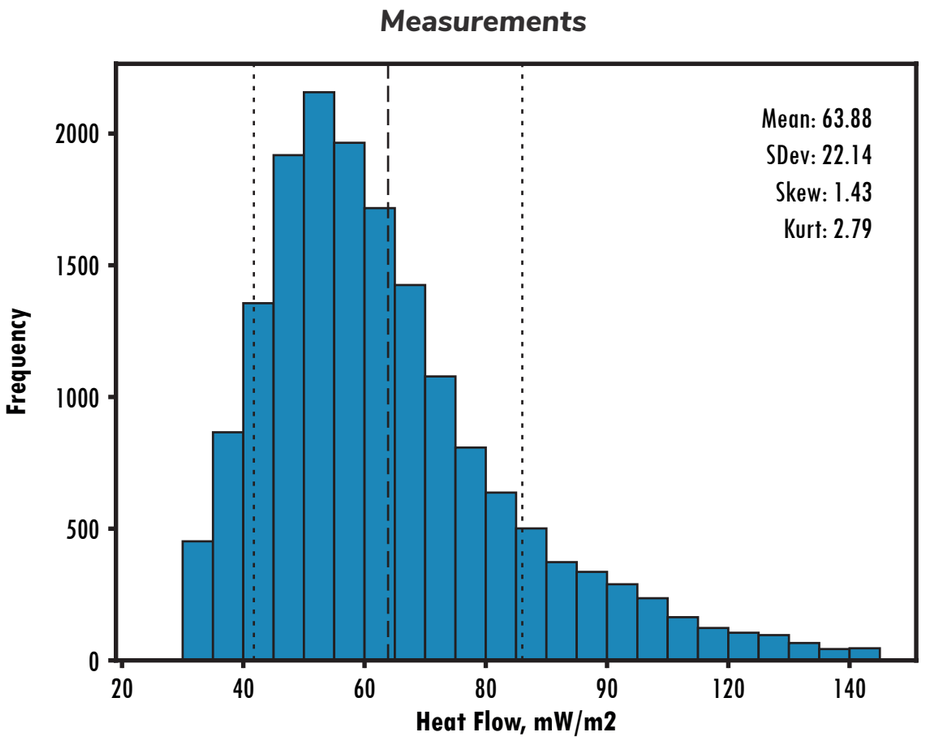

Global Extent

The histograms on Figure 8.3.5 show the distribution of heat flow measurements and predictions for Model 020. This uses the global extent data for both training and prediction.

- Measurements are heat flow data taken from Getech's interpreted heat flow database
- Training are random forest predictions for points where a heat flow measurement is known
- Prediction are random forest predictions for every point on a 0.25° grid.
- Error is the absolute value of (Measurement – Prediction), where we have both an observation and prediction.

Figure 8.3.5. Histograms showing data distributions for a. Getech's interpreted heat flow database (training data), b. the random forest model after training, c. the random forest model after prediction and d. the absolute error obtained by comparing the trained output with the real data.

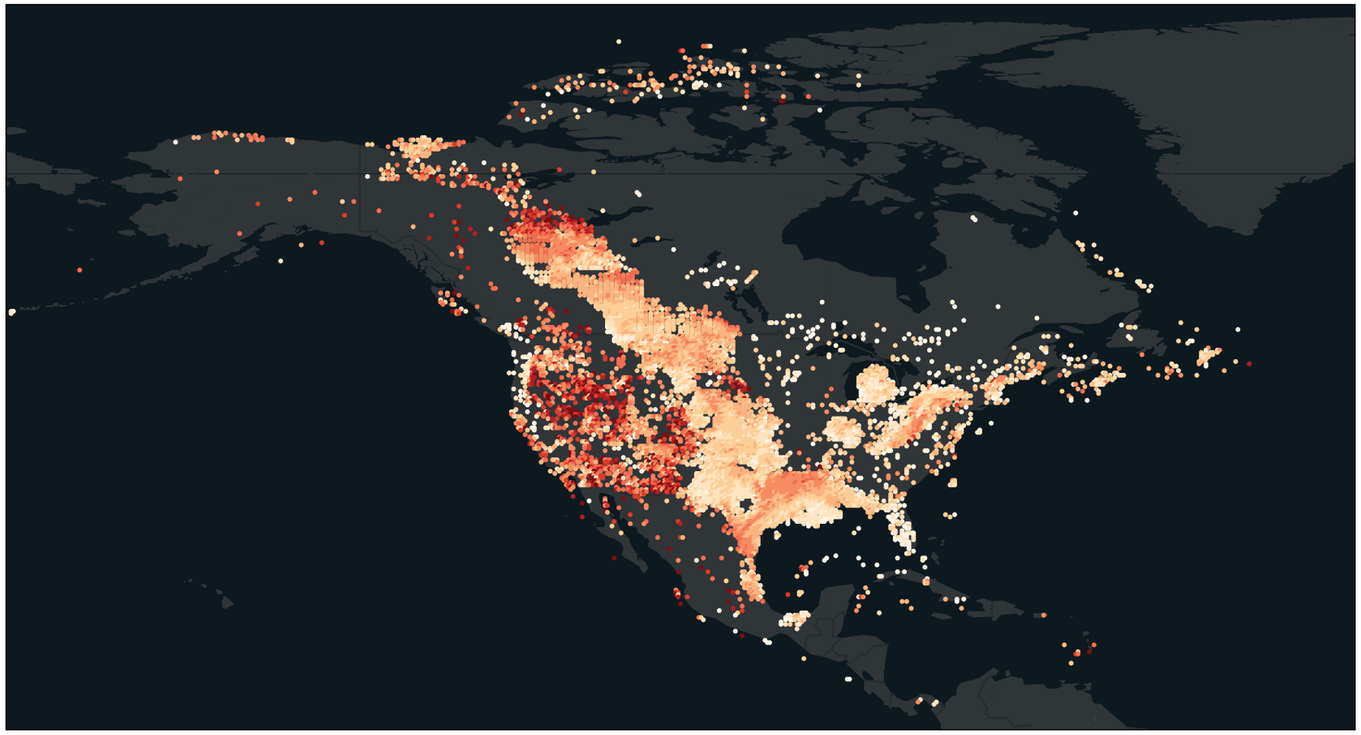

Figure 8.3.6a: Training data (heat flow measurements) from Getech's interpreted heat flow database, shown on global extent.

North America

Figure 8.3.6 shows the actual (8.3.6a) and trained (8.3.6b) data for model 008. Measurements taken from Getech's interpreted heat flow database and symbolised using a 9-class method, with roughly even number of records in each class.

Figure 8.3.6b (below): Random forest regression predicted heat flow for the same set of points (trained data).

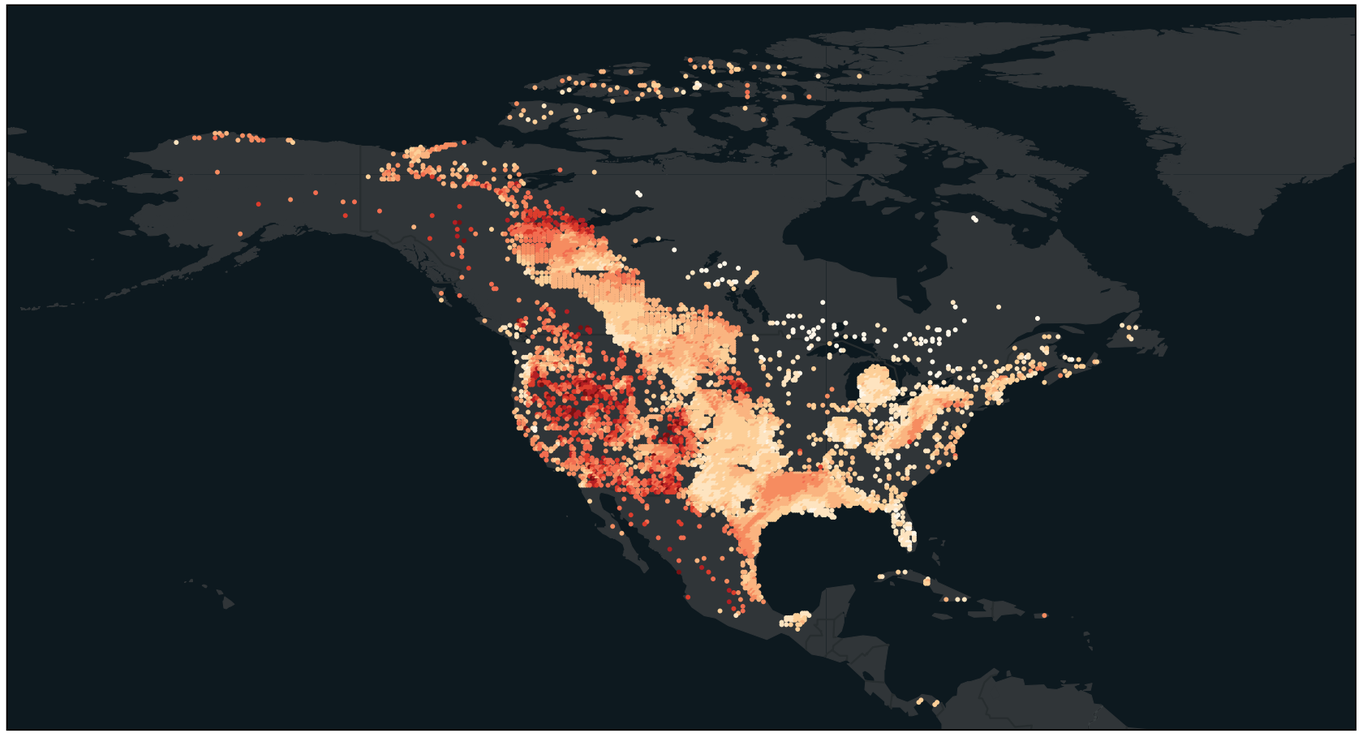

North America

The signed error (residual error) is calculated by subtracting the random forest prediction from the observed heat flow. Figure 8.3.7 shows the signed error for the global train and test data. Red points are underpredictions by the algorithm and blue points are overpredictions of the algorithm.

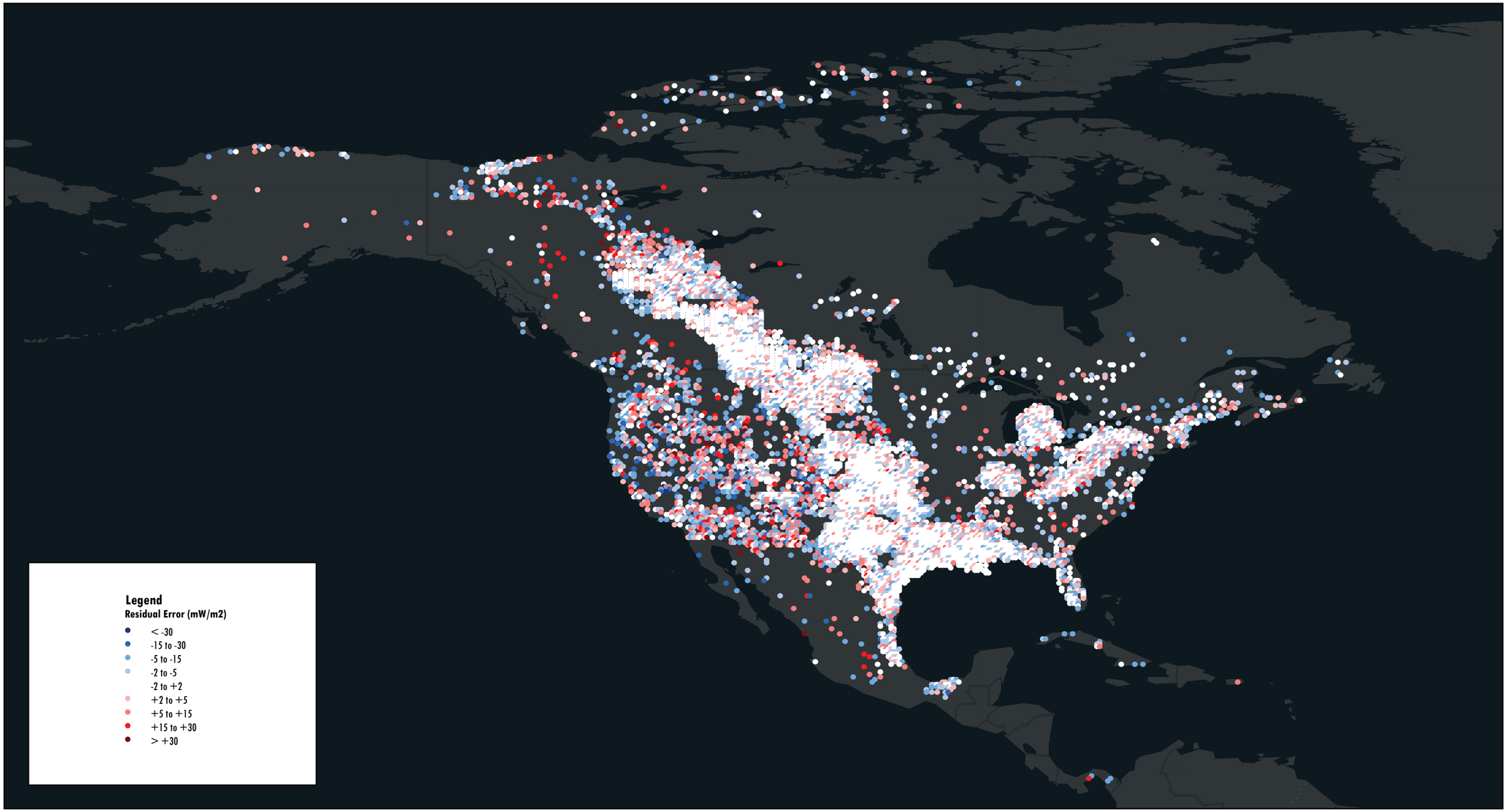

Figure 8.3.7. Residual error of the random forest prediction for North America.

North America

Figure 8.3.8 shows the prediction from model 008, the model trained on all North America heat flow measurements and predicted on a 0.25° grid. Points are displayed using the same colour ramp as the training data.

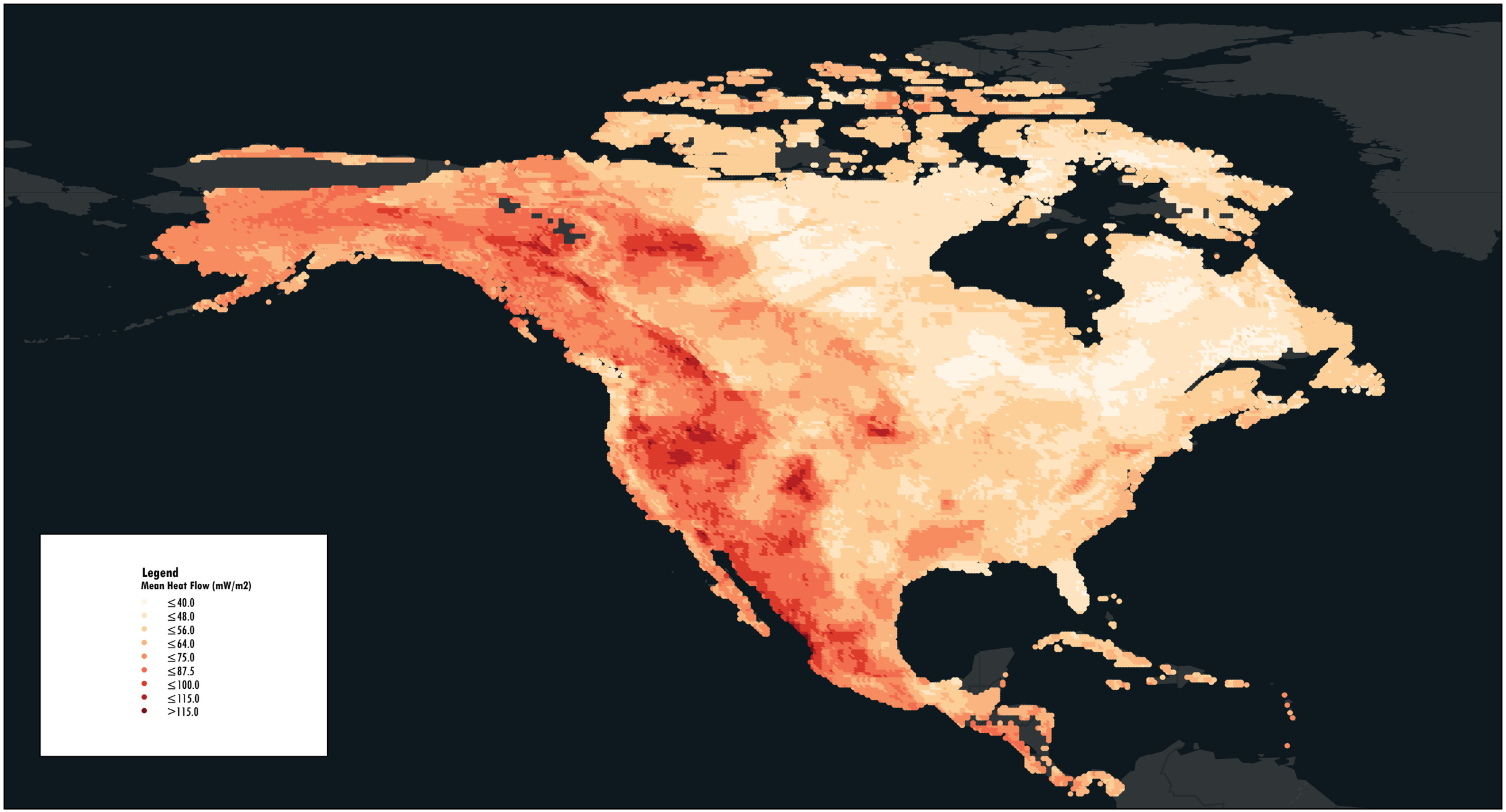

Figure 8.3.8. Random forest predictions of heat flow, predicted for North America by a random forest algorithm trained using North American data.

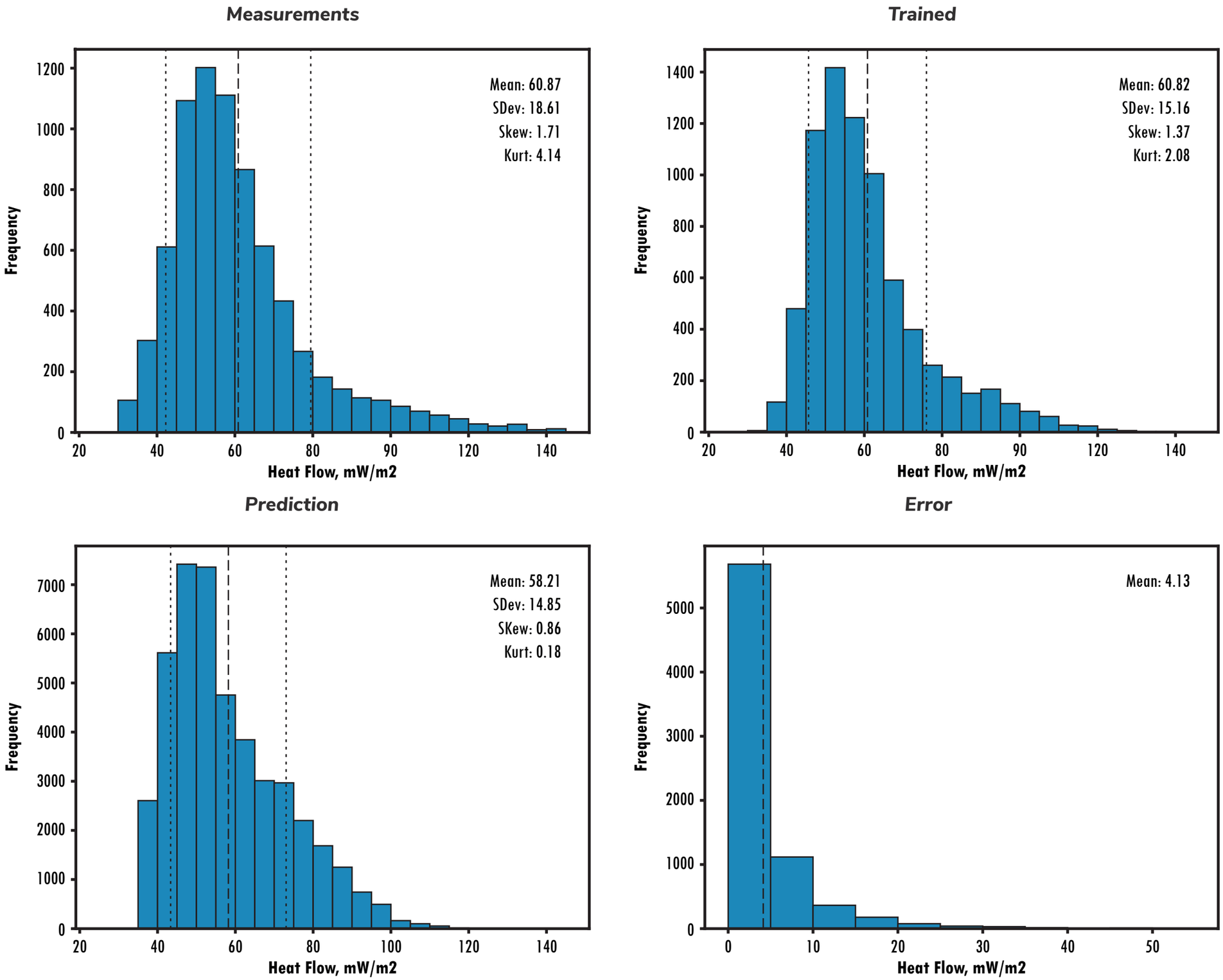

North America

The histograms on Figure 8.3.9 show the distribution of heat flow measurements and predictions for Model 008. This uses North America data for both training and prediction.

- Measurements are heat flow data taken from Getech's interpreted heat flow database
- Training are random forest predictions for points where a heat flow measurement is known
- Prediction are random forest predictions for every point on a 0.25° grid.
- Error is the absolute value of (Measurement – Prediction) where we have both an observation and prediction.

Figure 8.3.9. Histograms showing data distributions for a. Getech's interpreted heat flow database (training data), b. the random forest model after training, c. the random forest model after prediction and d. the absolute error obtained by comparing the trained output with the real data.

Figure 8.3.10a: Training data (heatflow measurements) from Getech's interpreted heat flow database, shown on global extent.

South America

Figure 8.3.10 shows the actual (8.3.10a) and trained (8.3.10b) data for model 011. Measurements taken from Getech's interpreted heat flow database and symbolised using a 9-class method, with roughly even number of records in each class.

Figure 8.3.10a (left): ***Training data (heatflow measurements) from Getech's interpreted heat flow database, shown on global extent.***

South America

The signed error (residual error) is calculated by subtracting the random forest prediction from the observed heat flow. Figure 8.3.11 shows the signed error for the global train and test data. Red points are underpredictions by the algorithm and blue points are overpredictions of the algorithm.

Figure 8.3.11. Residual error of the random forest training prediction for South America.

South America

Figure 8.3.12 shows the prediction from Model 011, the model trained on all South America heat flow measurements and predicted on a 0.25° grid. Points are displayed using the same colour ramp as the training data.

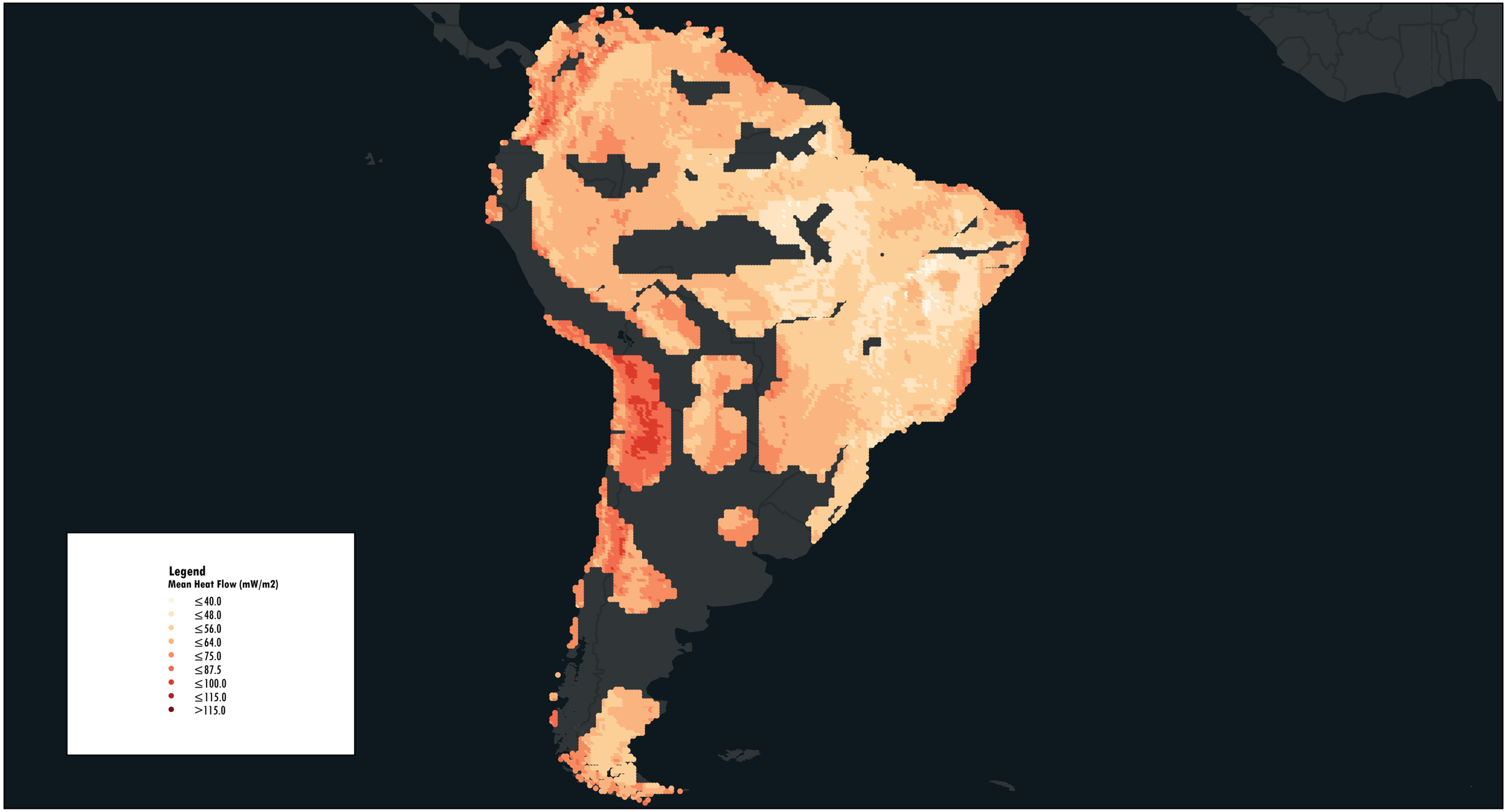

Figure 8.3.12. Random forest predictions of heat flow, predicted for North America by a random forest algorithm trained using North American data.

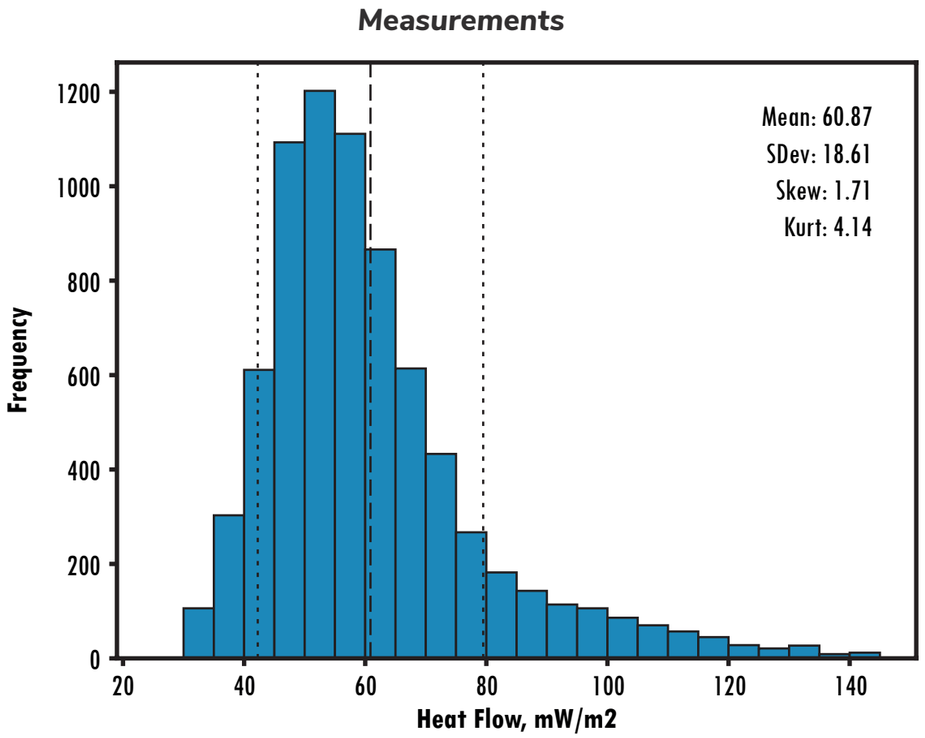

South America

The histograms on Figure 8.1.13 show the distribution of heat flow measurements and predictions for Model 011. This uses South America data for both training and prediction. The training data are supplemented with measurements from North America.

- Measurements are heat flow data taken from Getech's interpreted heat flow database
- Training are random forest predictions for points where a heat flow measurement is known
- Prediction are random forest predictions for every point on a 0.25° grid.
- Error is the absolute value of (Measurement – Prediction) where we have both an observation and prediction.

Figure 8.3.13. Histograms showing data distributions for a. Getech's interpreted heat flow database (training data), b. the random forest model after training, c. the random forest model after prediction and d. the absolute error obtained by comparing the trained output with the real data.

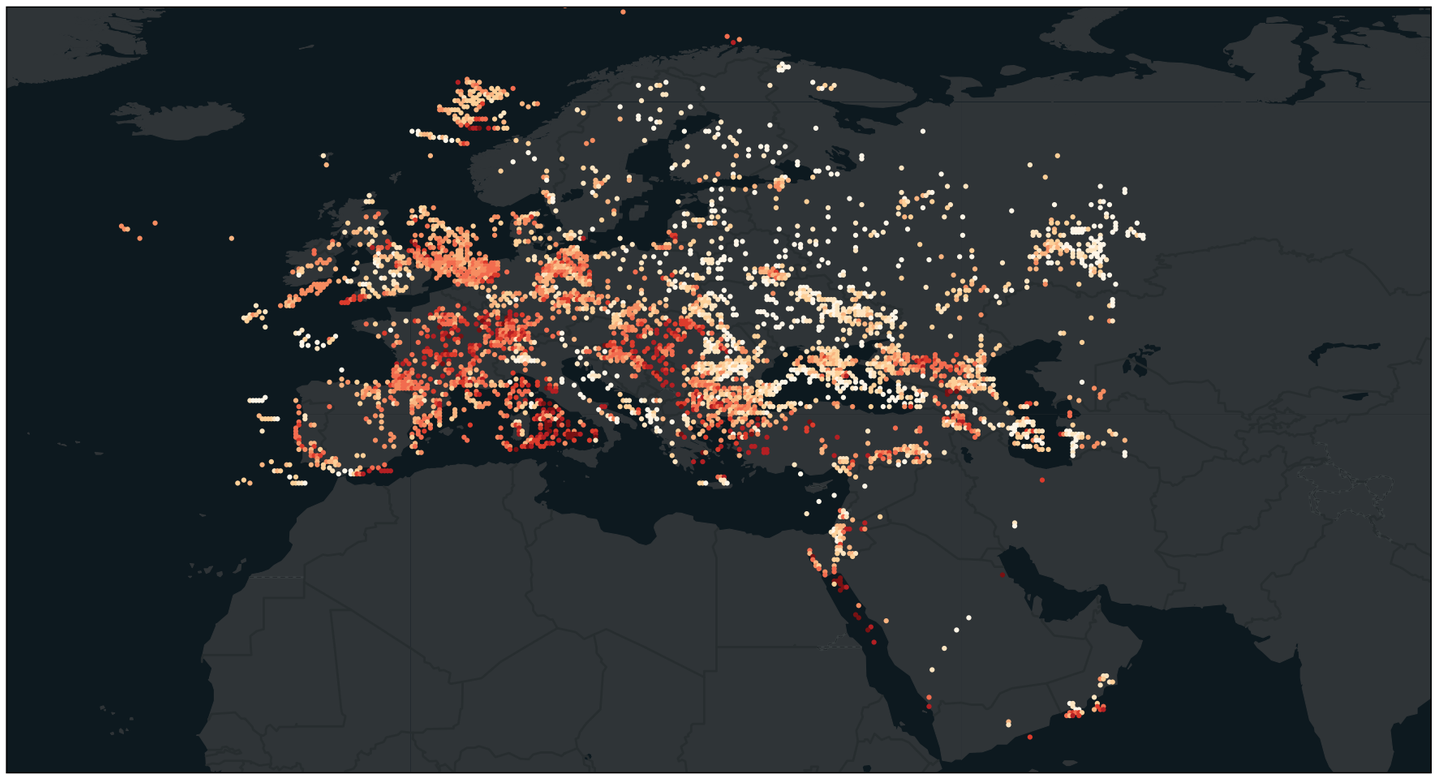

Figure 8.3.14a: Training data (heat flow measurements) from Getech's interpreted heat flow database, shown on global extent.

Europe

The actual (Figure 8.3.14a) and trained (8.3.14b) data for model 009. Measurements taken from Getech's interpreted heat flow database and symbolised using a 9-class method with roughly even number of records in each class.

Figure 8.3.14b (below): ***Random forest regression predicted heat flow for the same set of points (trained data).***

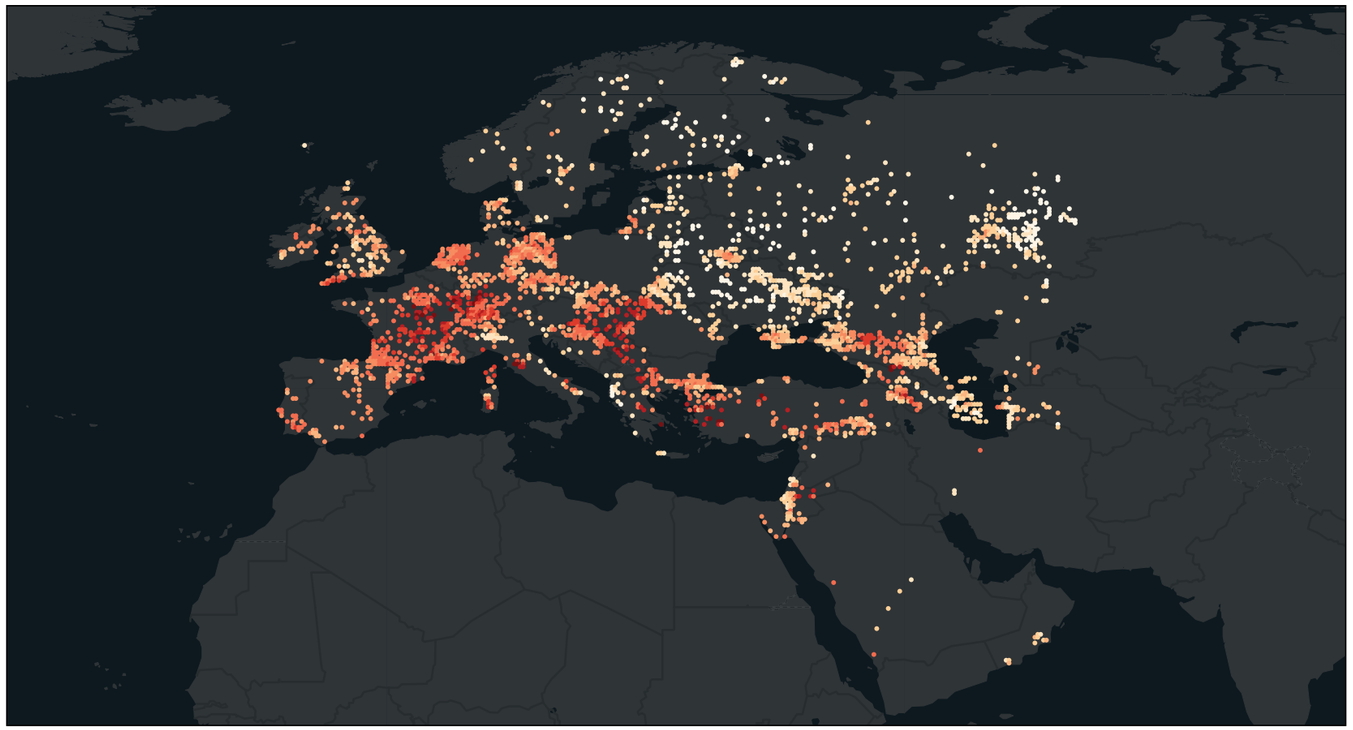

Europe

The signed error (residual error) is calculated by subtracting the random forest prediction from the observed heat flow. Figure 8.3.15 shows the signed error for the global train and test data. Red points are underpredictions by the algorithm and blue points are overpredictions of the algorithm.

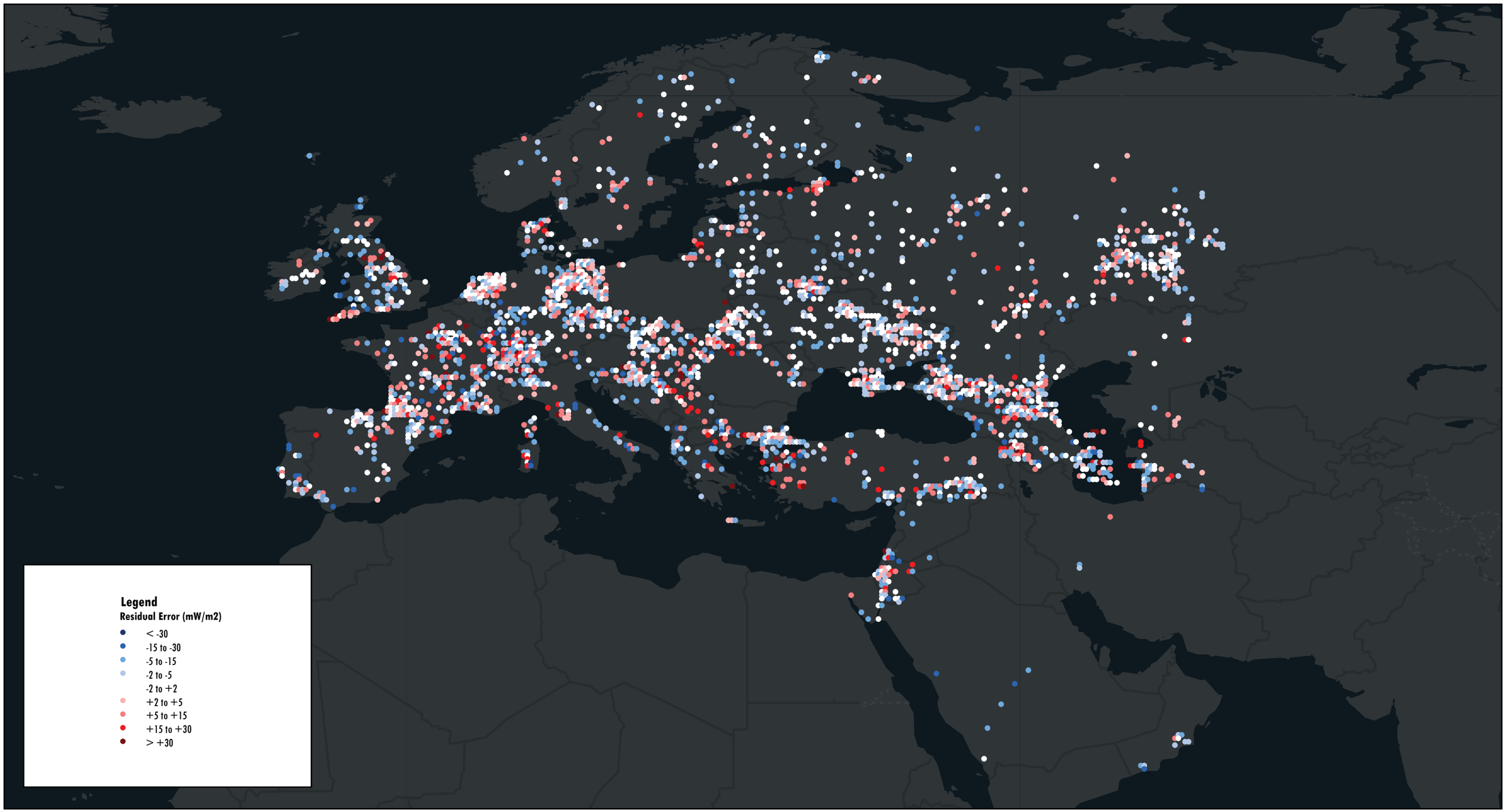

Figure 8.3.15. Residual error of the random forest training prediction for Europe.

Europe

Figure 8.3.16 shows the prediction from model 008, the model trained on all South America heat flow measurements and predicted on a 0.25° grid. Points are displayed using the same colour ramp as the training data.

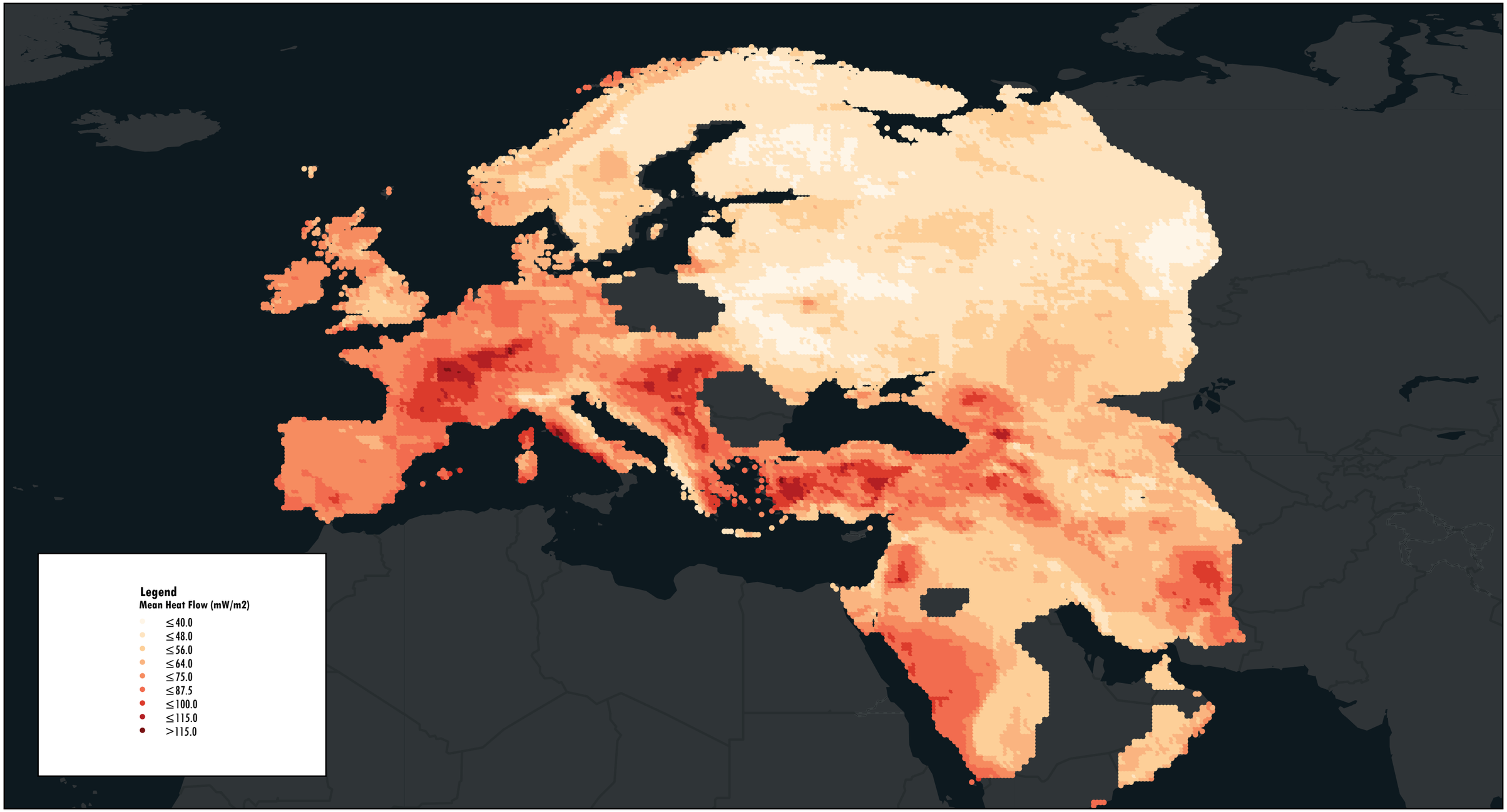

Figure 8.3.16. Random forest predictions of heat flow, predicted for Europe by a random forest algorithm trained using European data.

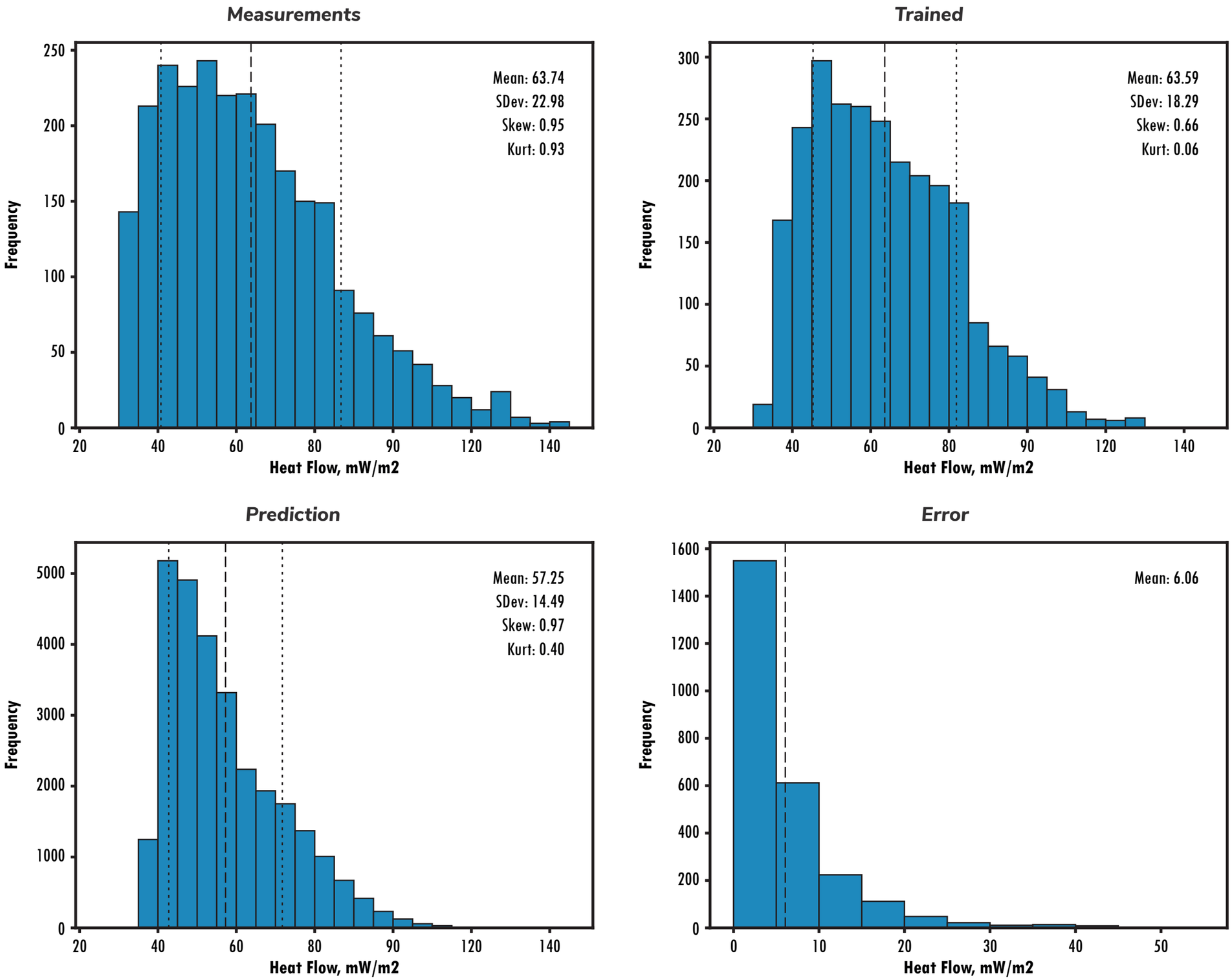

Europe

The histograms on Figure 8.3.17 show the distribution of heat flow measurements and predictions for Model 009. This uses European data for both training and prediction.

- Measurements are heat flow data taken from Getech's interpreted heat flow database
- Training are random forest predictions for points where a heat flow measurement is known
- Prediction are random forest predictions for every point on a 0.25° grid.
- Error is the absolute value of (Measurement – Prediction) where we have both an observation and prediction.

Figure 8.3.17. Histograms showing data distributions for a. Getech's interpreted heat flow database (training data), b. the random forest model after training, c. the random forest model after prediction and d. the absolute error obtained by comparing the trained output with the real data.

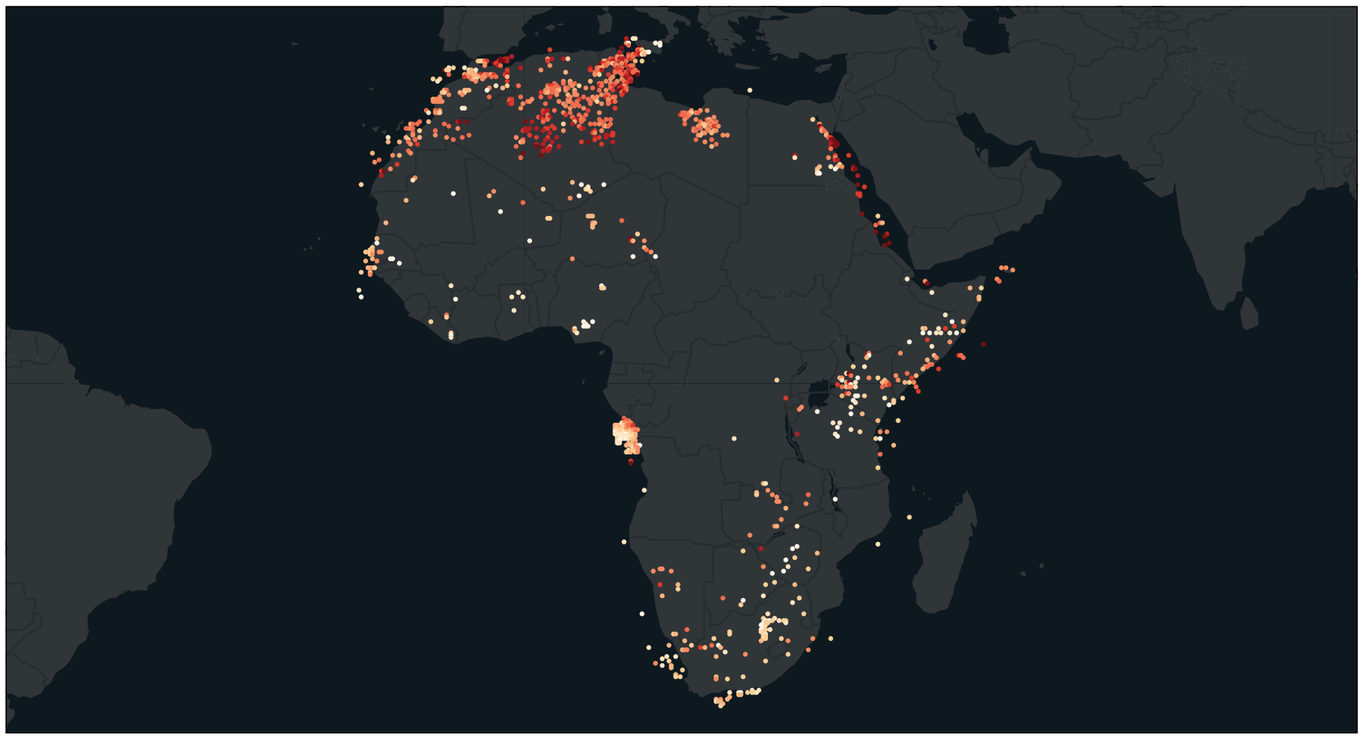

Figure 8.3.18a: Training data (heatflow measurements) from Getech's interpreted heat flow database, shown on global extent.

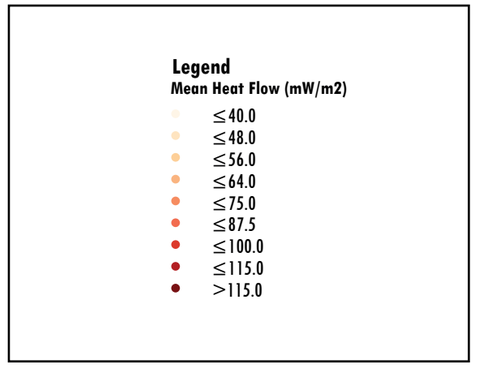

Africa

The actual (Figure 8.3.18a) and trained (8.3.18b) data for Model 014. Measurements taken from Getech's interpreted heat flow database and symbolised using a 9-class method with roughly even number of records in each class.

Figure 8.3.18b (below): ***Random forest regression predicted heat flow for the same set of points (trained data).***

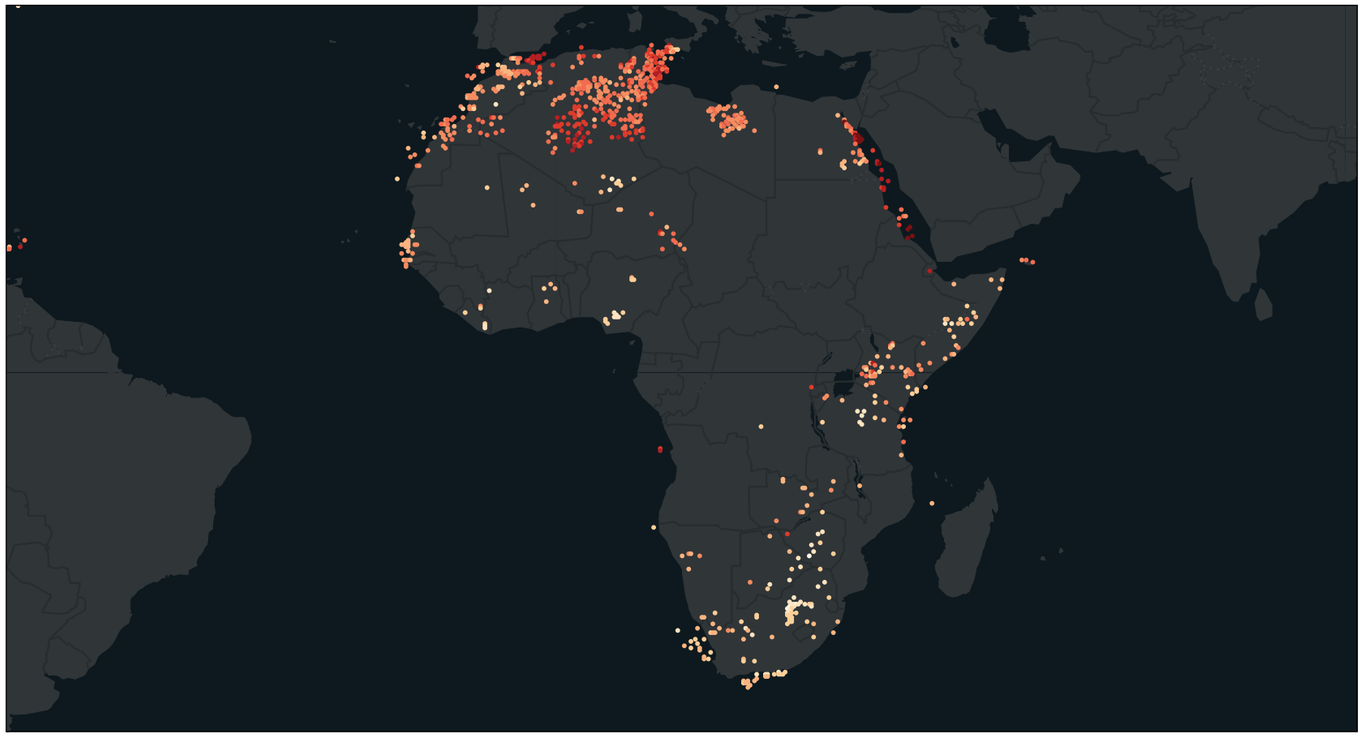

Africa

The signed error (residual error) is calculated by subtracting the random forest prediction from the observed heat flow. Figure 8.3.19 shows the signed error for the global train and test data. Red points are underpredictions by the algorithm and blue points are overpredictions of the algorithm.

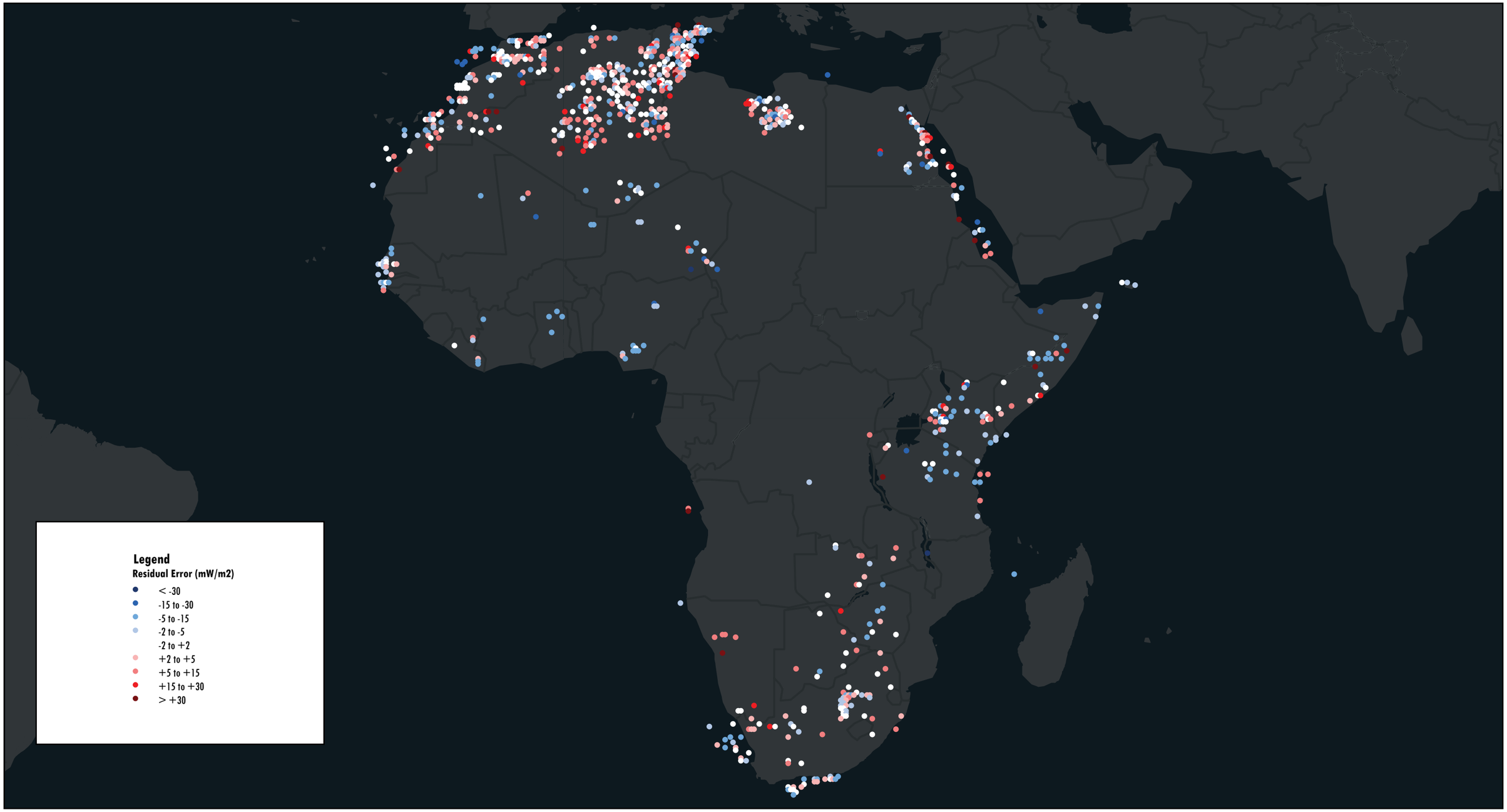

Figure 8.3.19. Residual error of the random forest training prediction for Africa.

Africa

Figure 8.3.20 shows the prediction from Model 014, the model trained on all South America heat flow measurements and predicted on a 0.25° grid. Points are displayed using the same colour ramp as the training data.

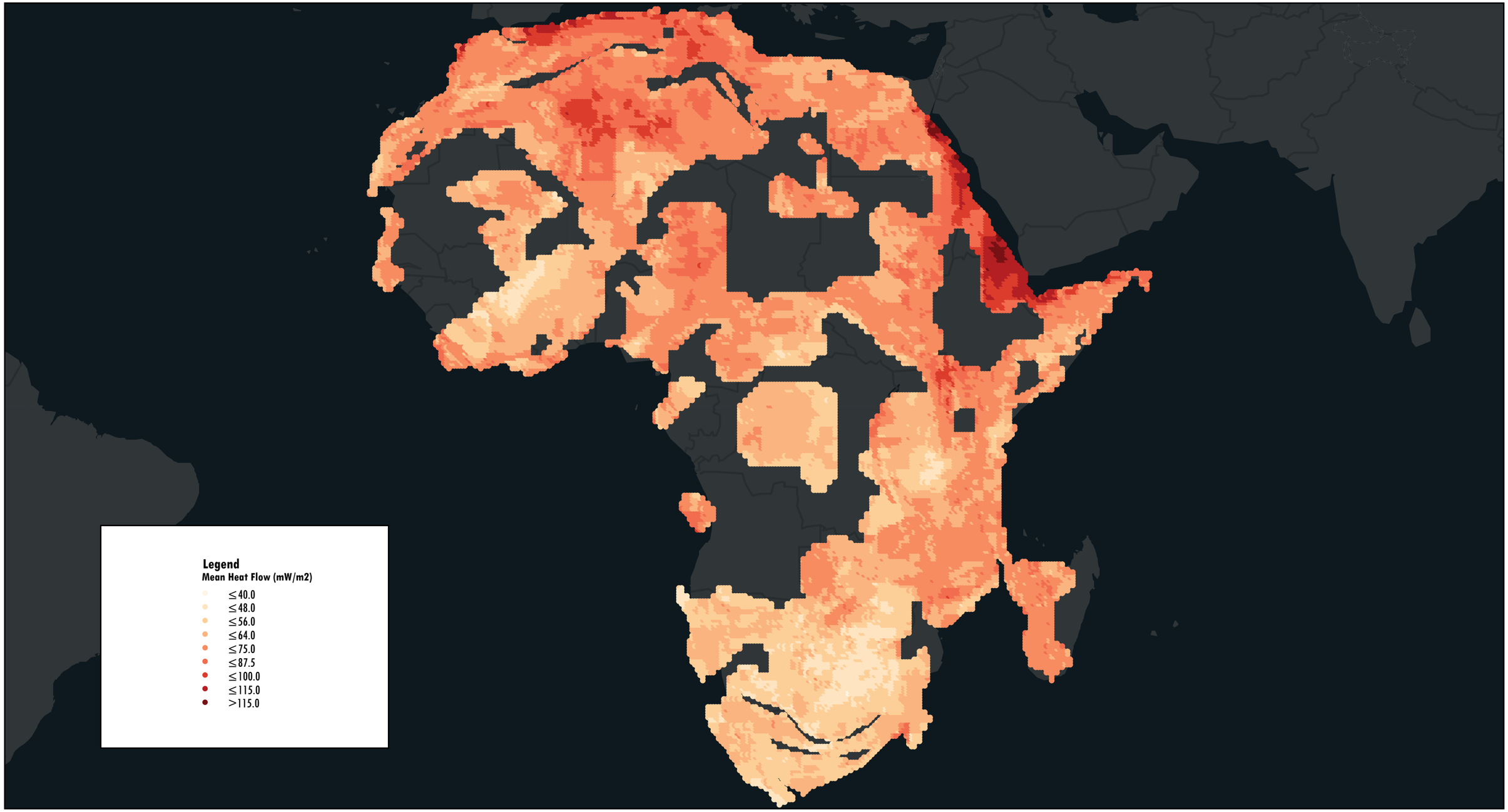

Figure 8.3.20. Random forest predictions of heat flow, predicted for Africa by a random forest algorithm trained using African and North American data.

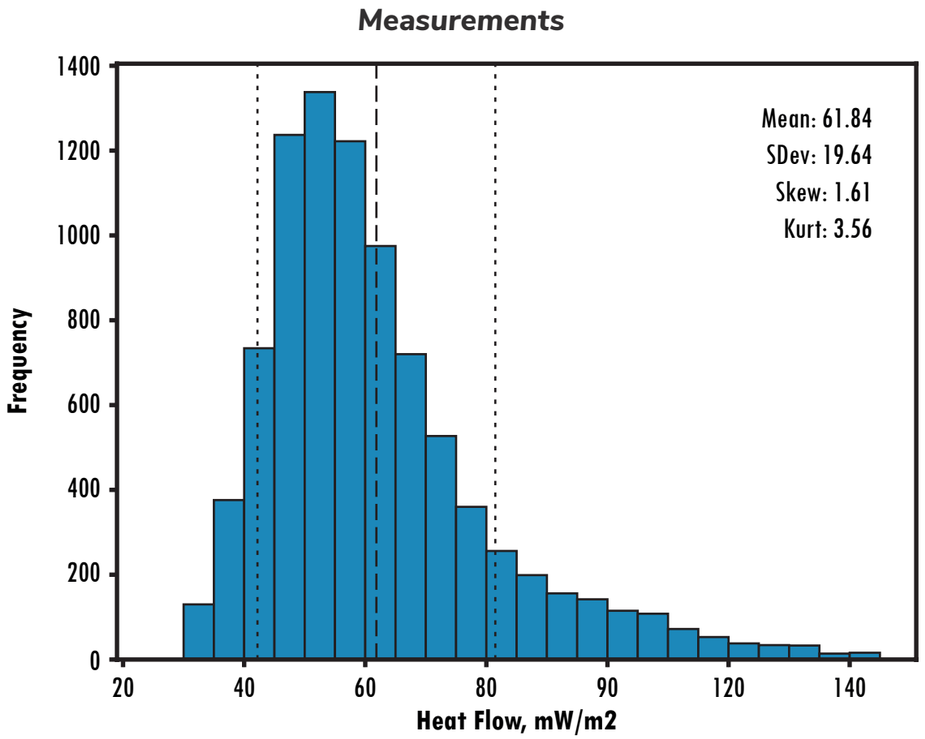

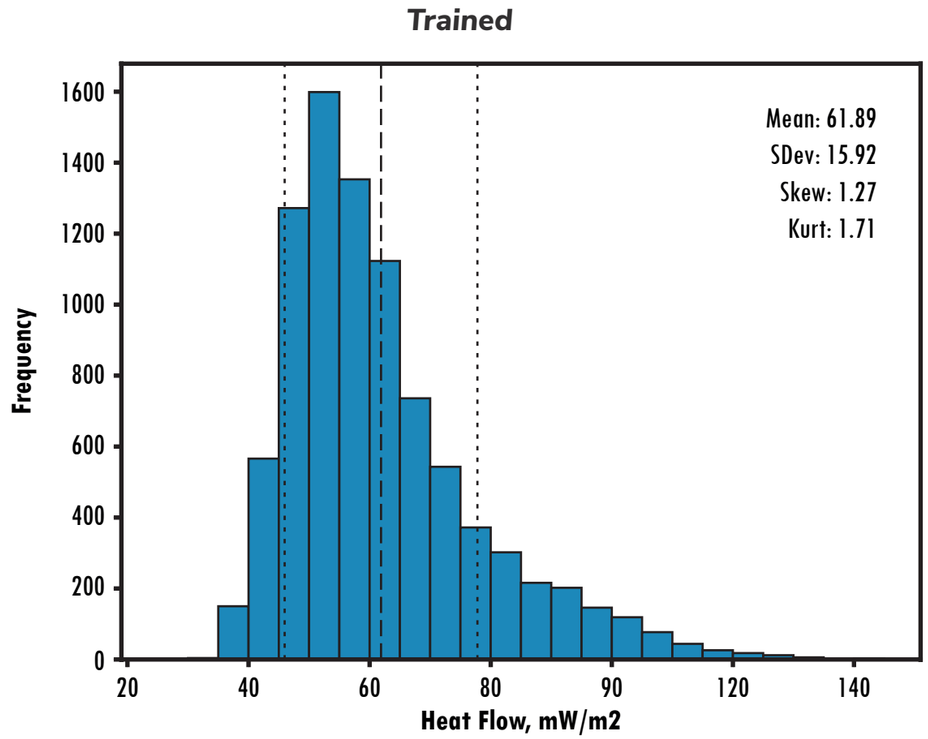

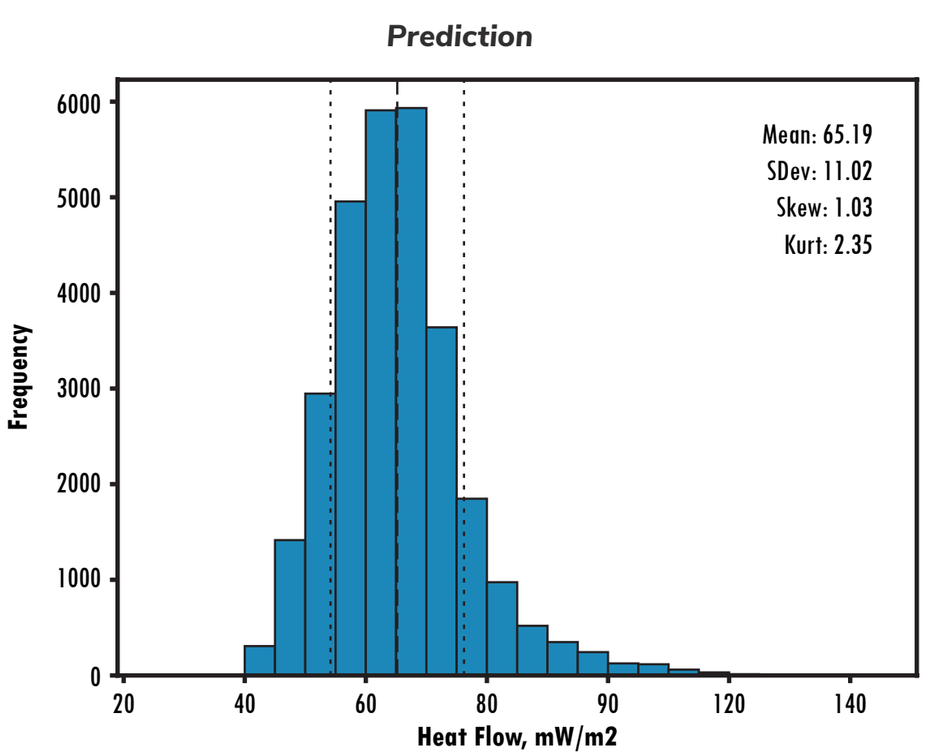

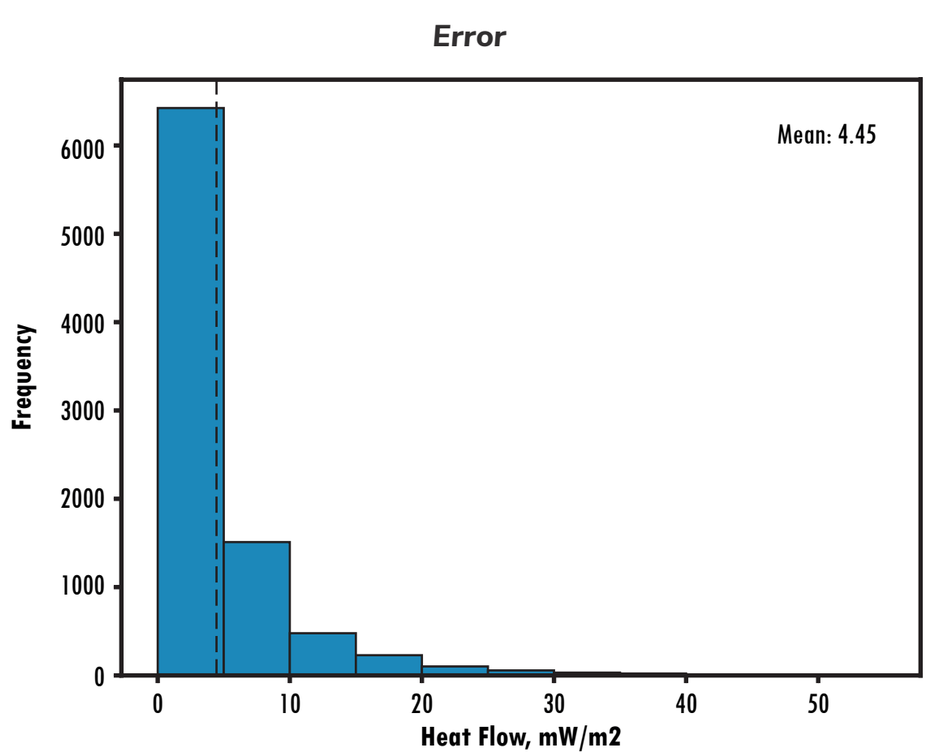

Africa

The histograms on Figure 8.3.21 show the distribution of heat flow measurements and predictions for Model 014. This uses African data for both training and prediction. The training data are supplemented with measurements from North America.

- Measurements are heat flow data taken from Getech's interpreted heat flow database
- Training are random forest predictions for points where a heat flow measurement is known
- Prediction are random forest predictions for every point on a 0.25° grid.
- Error is the absolute value of (Measurement – Prediction) where we have both an observation and prediction.

Figure 8.3.21. Histograms showing data distributions for a. Getech's interpreted heat flow database (training data), b. the random forest model after training, c. the random forest model after prediction and d. the absolute error obtained by comparing the trained output with the real data.

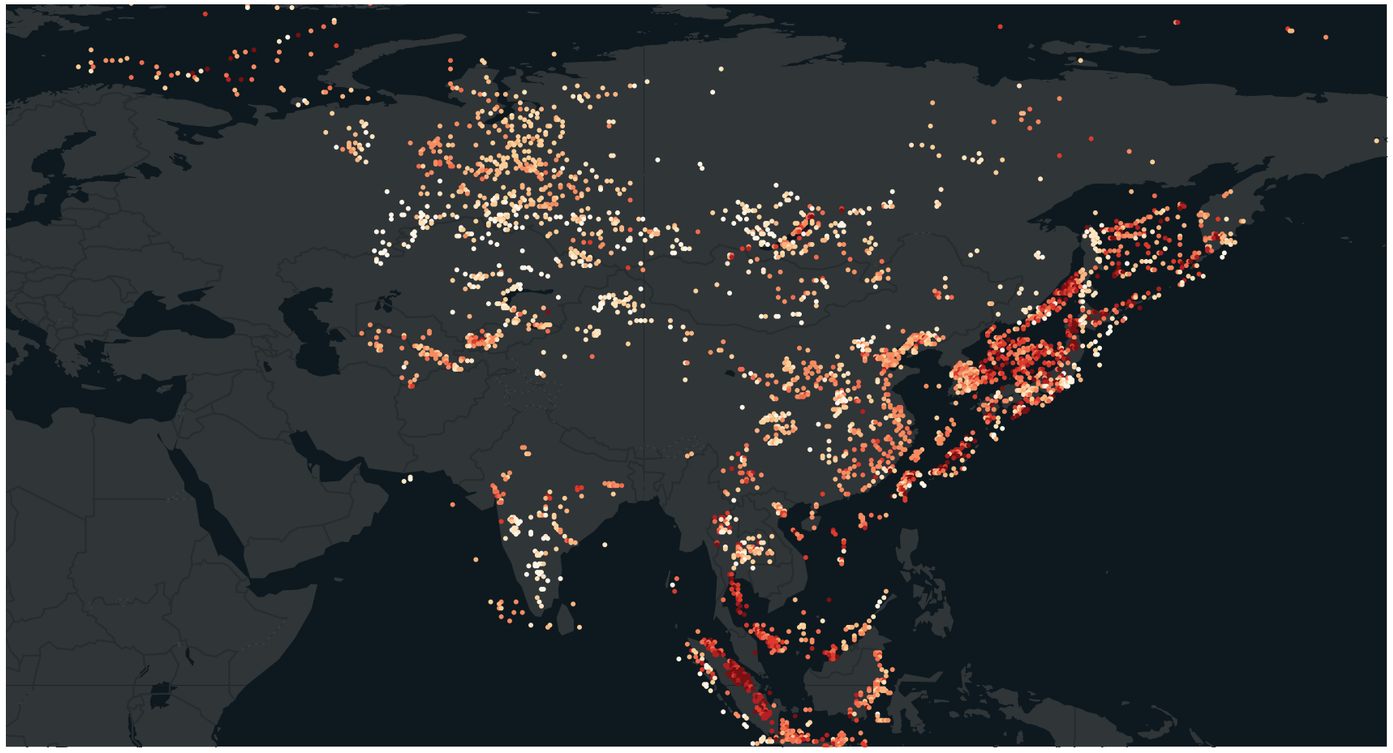

Figure 8.3.22a: Training data (heatflow measurements) from Getech's interpreted heat flow database, shown on global extent.

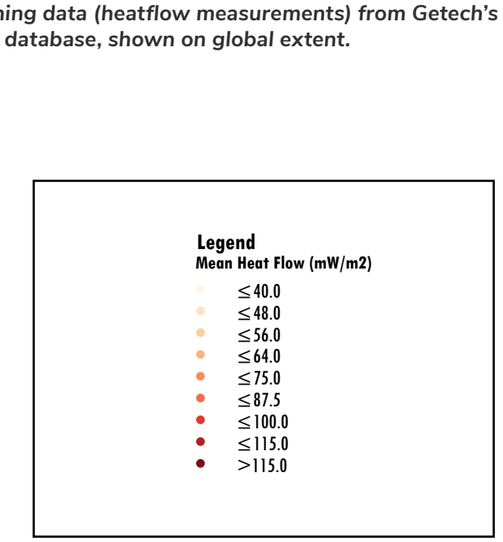

Asia

The actual (Figure 8.3.22a) and trained (8.3.22b) data for Model 015. Measurements taken from Getech's interpreted heat flow database and symbolised using a 9-class method with roughly even number of records in each class.

Figure 8.3.22b (below): Random forest regression predicted heat flow for the same set of points (trained data).

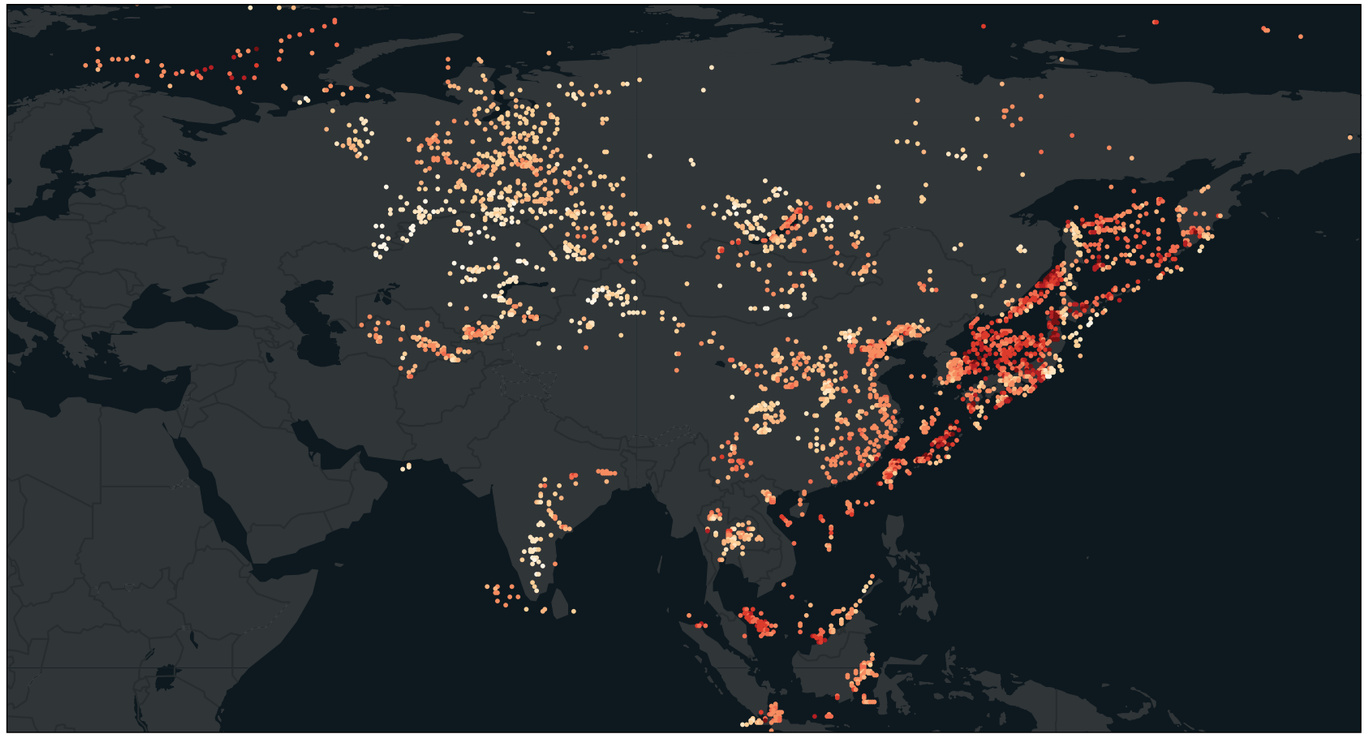

Asia

The signed error (residual error) is calculated by subtracting the random forest prediction from the observed heat flow. Figure 8.3.23 shows the signed error for the global train and test data. Red points are underpredictions by the algorithm and blue points are overpredictions of the algorithm.

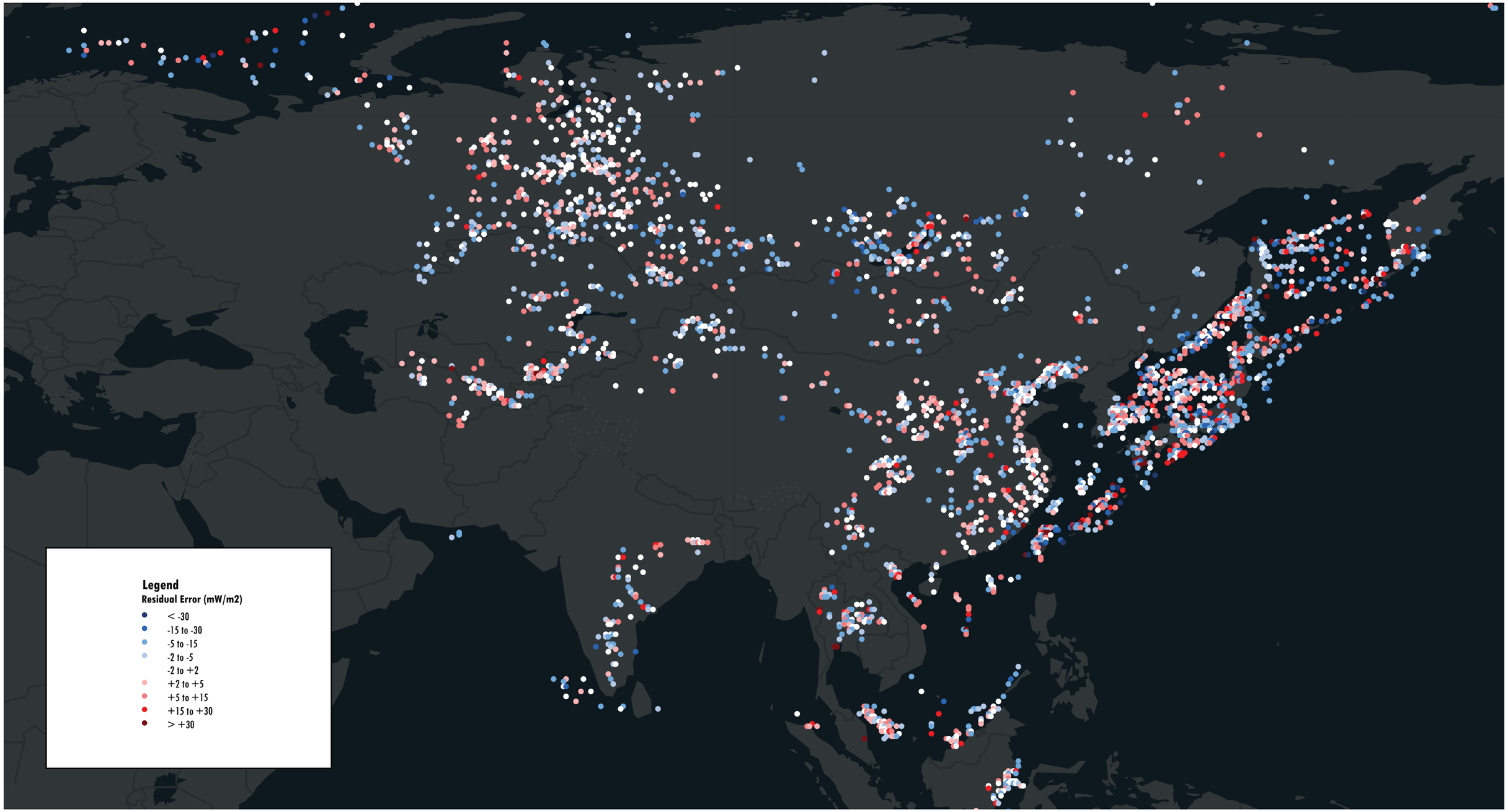

Figure 8.3.23. Residual error of the random forest training prediction for Asia.

Asia

Figure 8.3.24 shows the prediction from model 015, the model trained on all South America heat flow measurements and predicted on a 0.25° grid. Points are displayed using the same colour ramp as the training data.

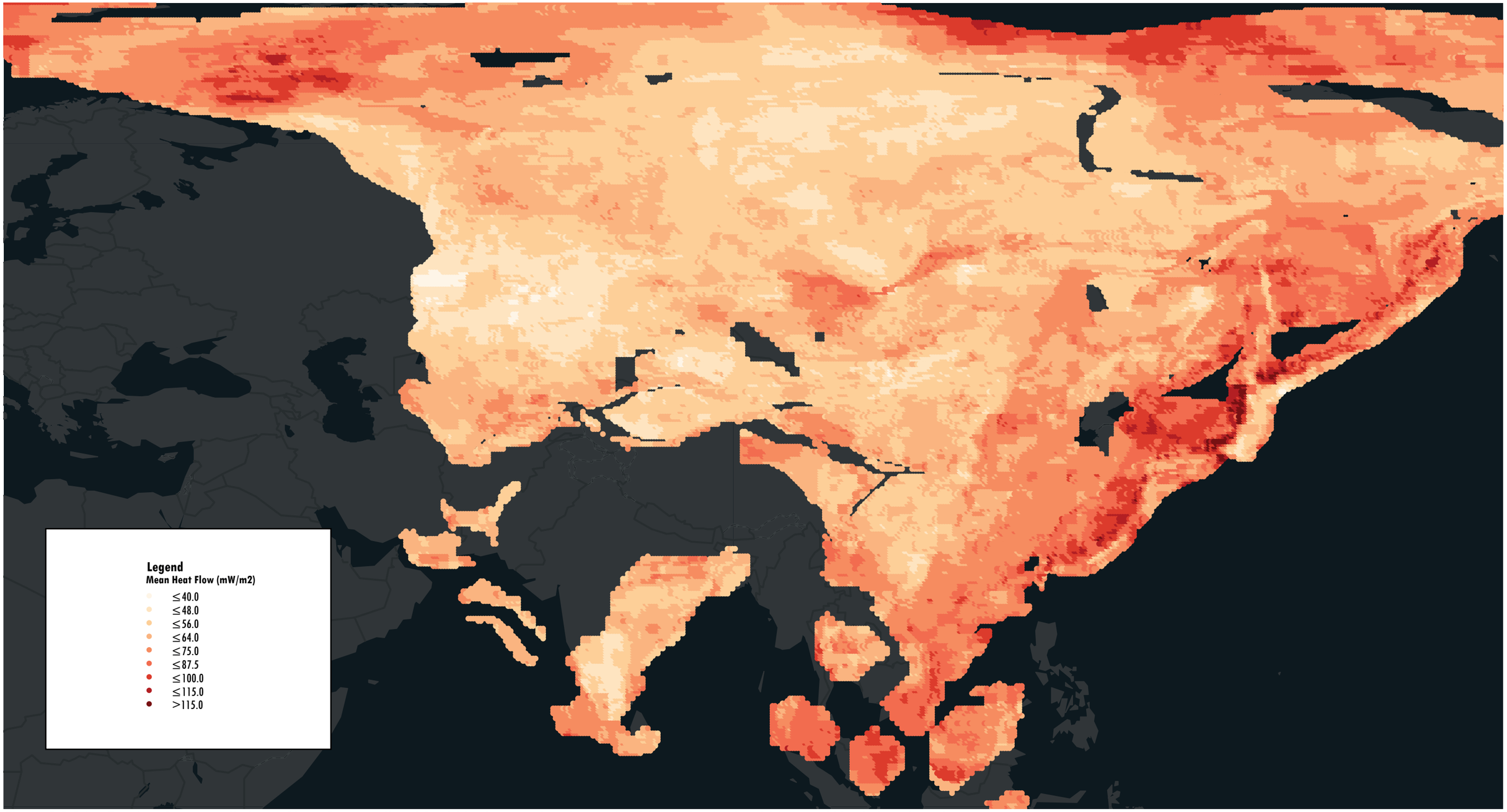

Figure 8.3.24. Random forest predictions of heat flow, predicted for Africa by a random forest algorithm trained using African and North American data.

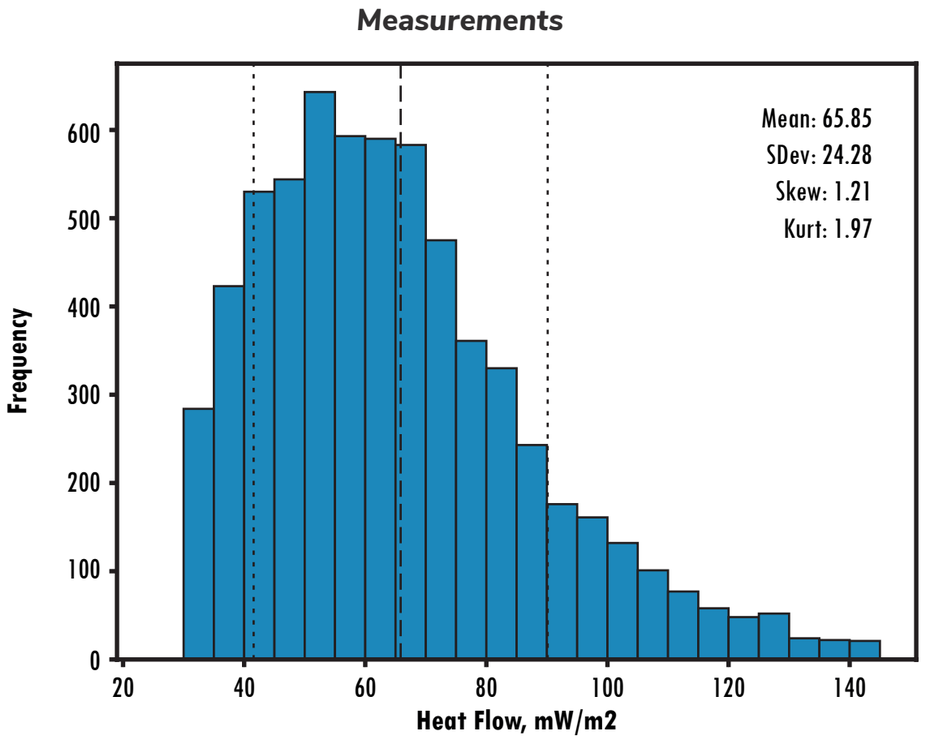

Asia

The histograms on Figure 8.3.25 show the distribution of heat flow measurements and predictions for Model 015. This uses Asian data for both training and prediction. The training data are supplemented with measurements from North America.

- Measurements are heat flow data taken from Getech's interpreted heat flow database
- Training are random forest predictions for points where a heat flow measurement is known
- Prediction are random forest predictions for every point on a 0.25° grid.
- Error is the absolute value of (Measurement – Prediction) where we have both an observation and prediction.

Figure 8.3.25. Histograms showing data distributions for a. Getech's interpreted heat flow database (training data), b. the random forest model after training, c. the random forest model after prediction and d. the absolute error obtained by comparing the trained output with the real data.

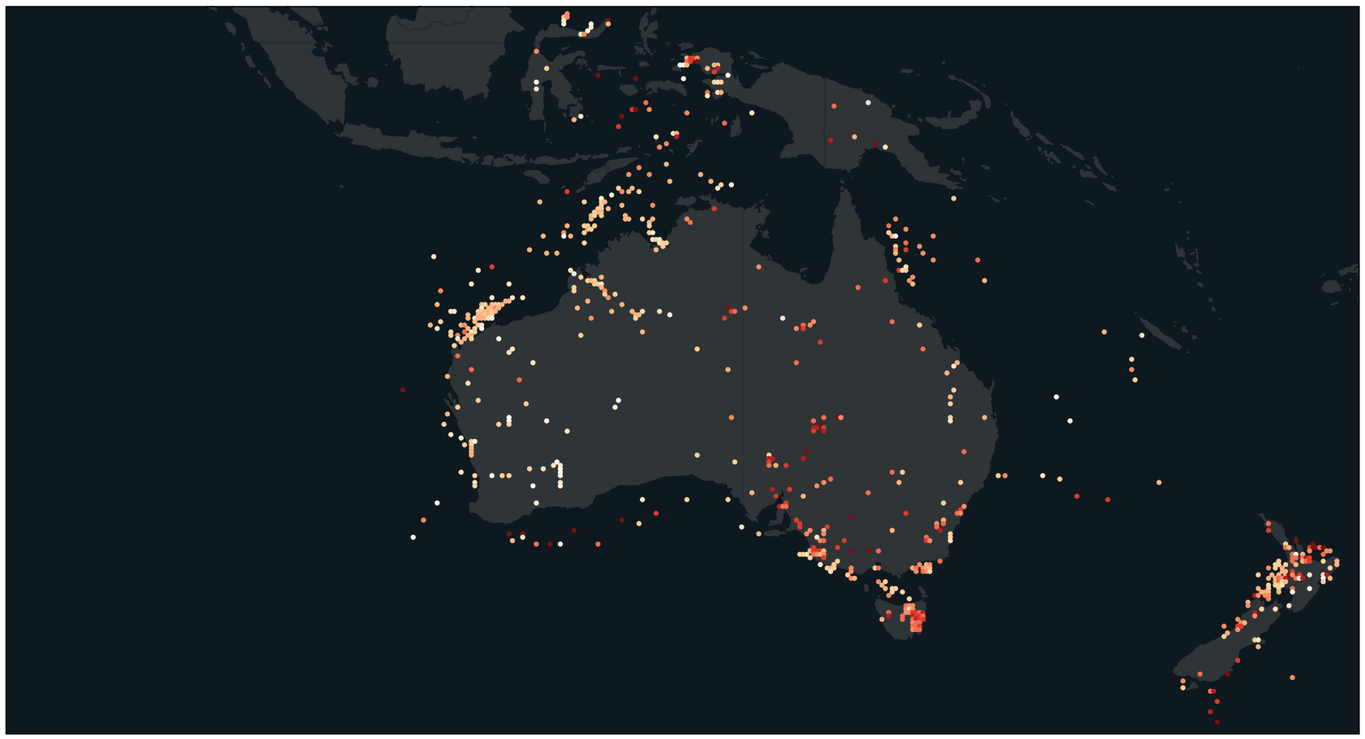

Figure 8.3.26a: Training data (heatflow measurements) from Getech's interpreted heat flow database, shown on global extent.

Australia

The actual (Figure 8.3.26a) and trained (8.3.26b) data for Model 019. Measurements taken from Getech's interpreted heat flow database and symbolised using a 9-class method with roughly even number of records in each class.

Figure 8.3.26b (below): ***Random forest regression predicted heat flow for the same set of points (trained data).***

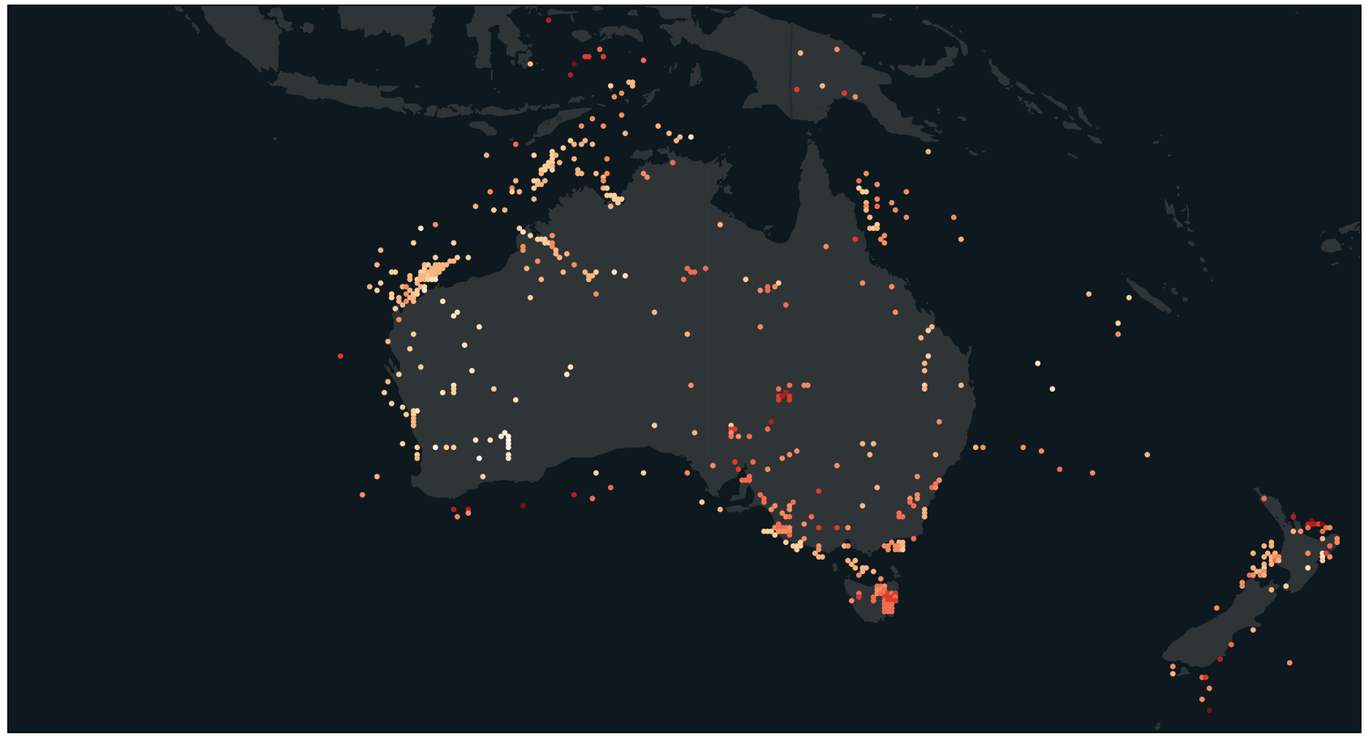

Australia

The signed error (residual error) is calculated by subtracting the random forest prediction from the observed heat flow. Figure 8.3.27 shows the signed error for the global train and test data. Red points are underpredictions by the algorithm and blue points are overpredictions of the algorithm.

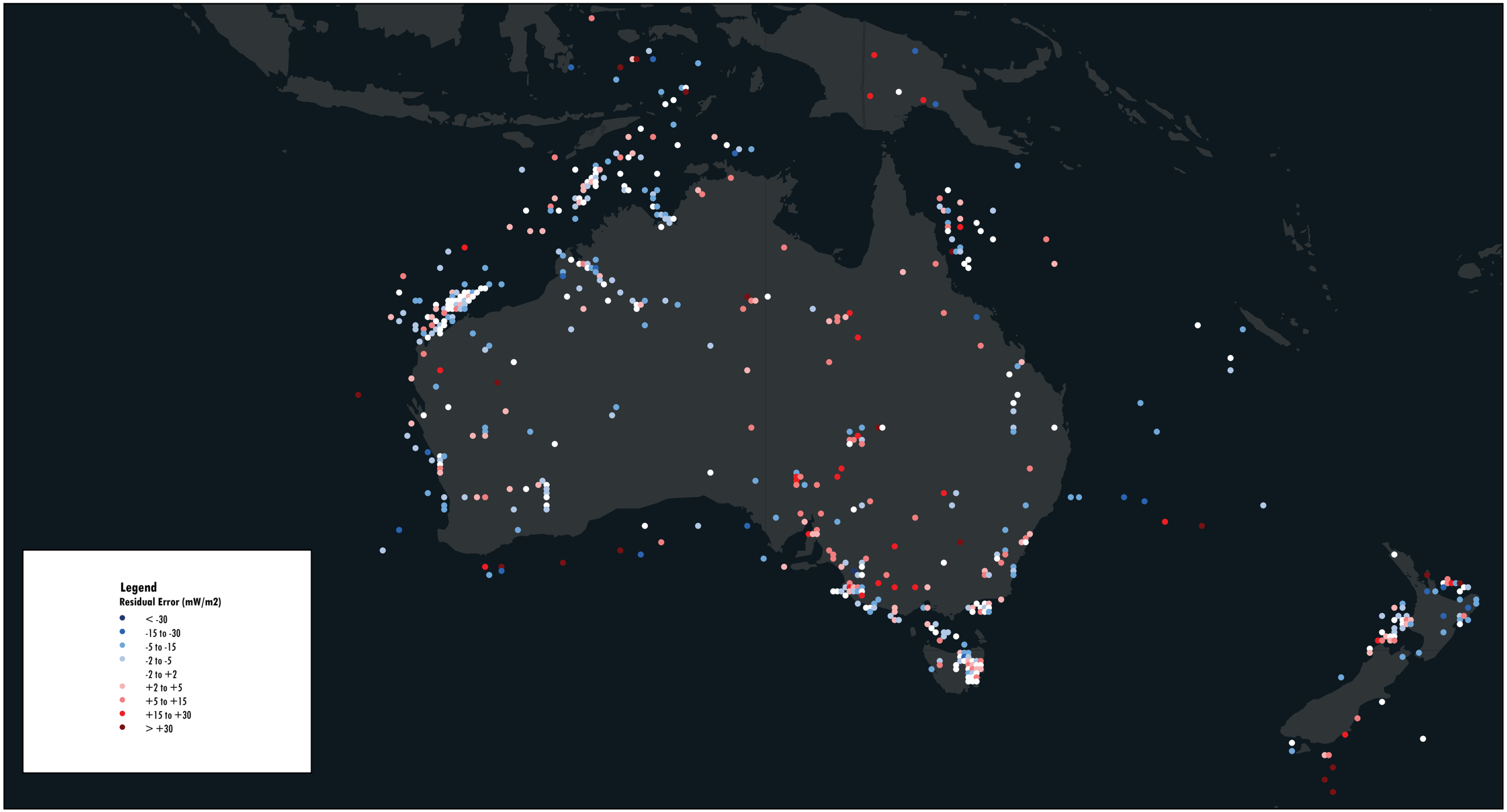

Figure 8.3.27. Residual error of the random forest training prediction for Asia.

Australia

Figure 8.3.28 shows the prediction from model 015, the model trained on all South America heat flow measurements and predicted on a 0.25° grid. Points are displayed using the same colour ramp as the training data.

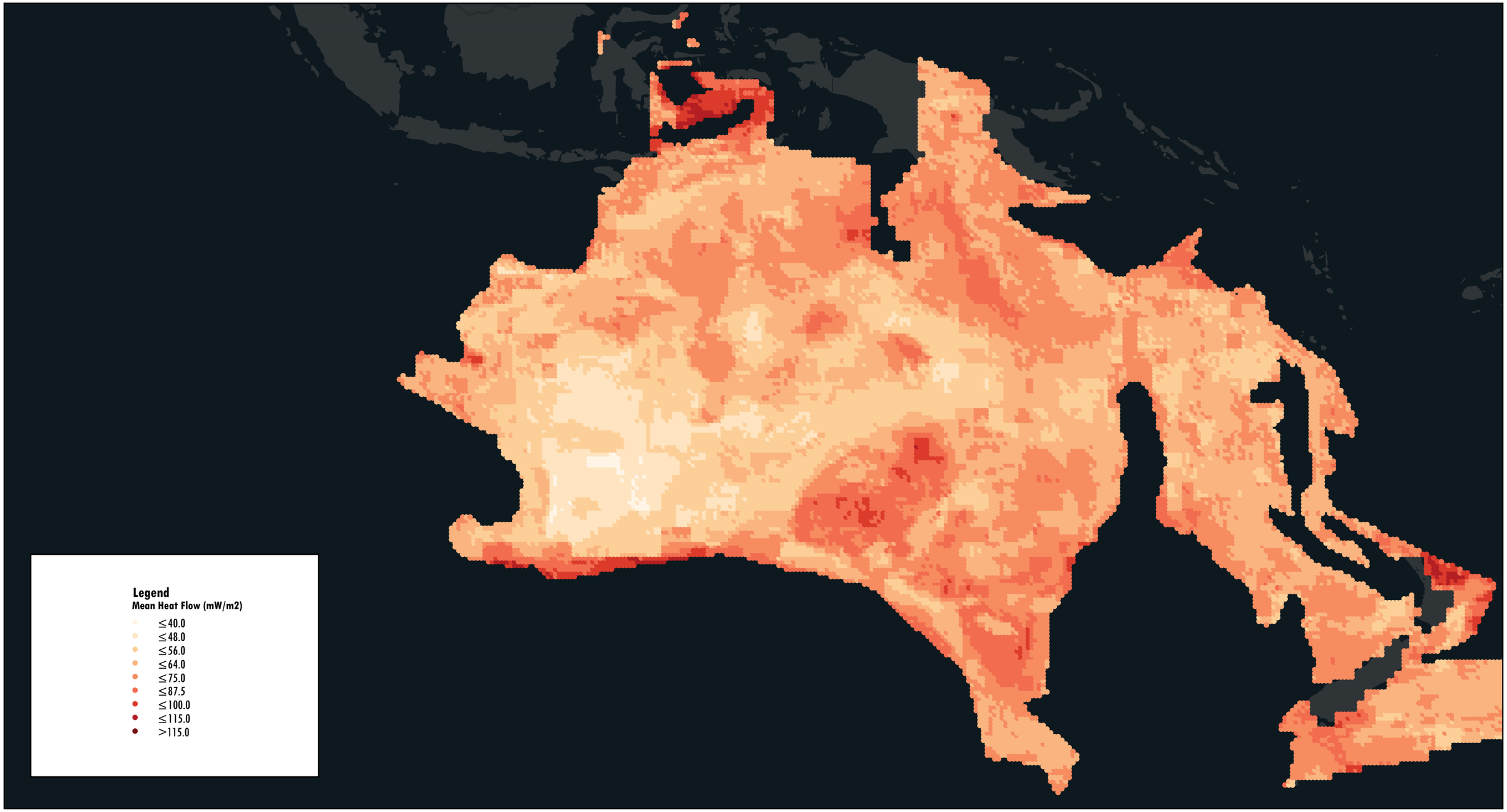

Figure 8.3.28. Random forest predictions of heat flow, predicted for Africa by a random forest algorithm trained using African and North American data.

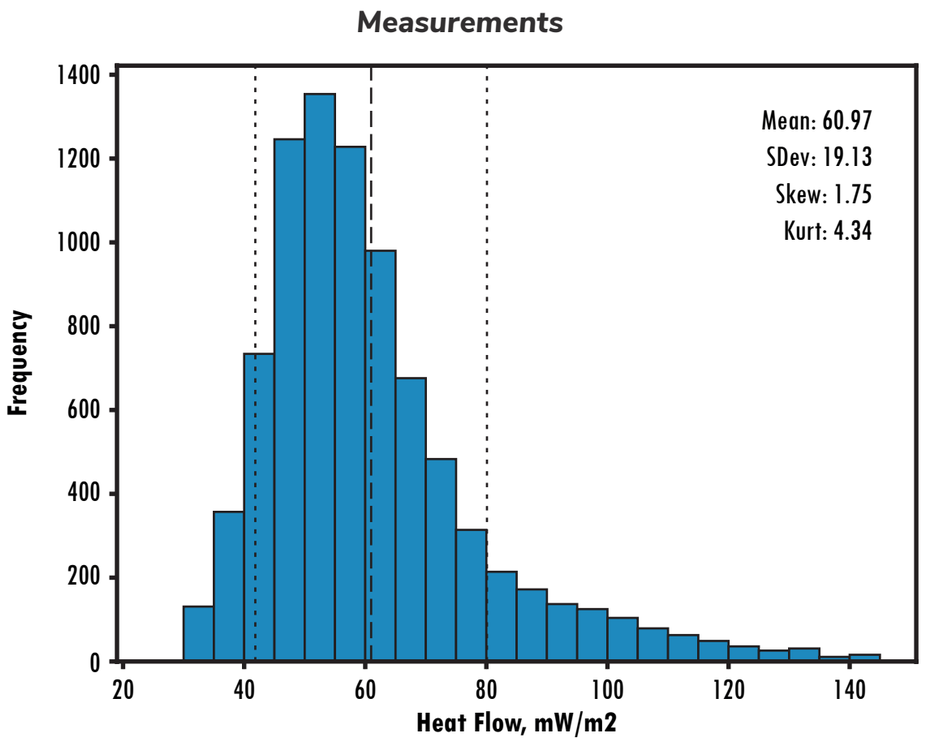

Australia

The histograms on Figure 8.329 show the distribution of heat flow measurements and predictions for Model 019. This uses Australian data for both training and prediction.
The training data are supplemented with measurements from North America.

- Measurements are heat flow data taken from Getech's interpreted heat flow database
- Training are random forest predictions for points where a heat flow measurement is known
- Prediction are random forest predictions for every point on a 0.25° grid.
- Error is the absolute value of (Measurement – Prediction) where we have both an observation and prediction.

Figure 8.3.29: Histograms showing data distributions for a. Getech's interpreted heat flow database (training data), b. the random forest model after training, c. the random forest model after prediction and d. the absolute error obtained by comparing the trained output with the real data.

8.4. Machine Learning: Results

The final set of deliverables this year involve deriving a series of temperature at depth and temperature at specific surfaces. We followed the same method to calculate temperature at depth as we described in Section 6.3, but rather than using Getech's heat flow database as the input heat flow points, we used the prediction from the preferred random forest algorithm (the version with a combination of six models for six different continents)

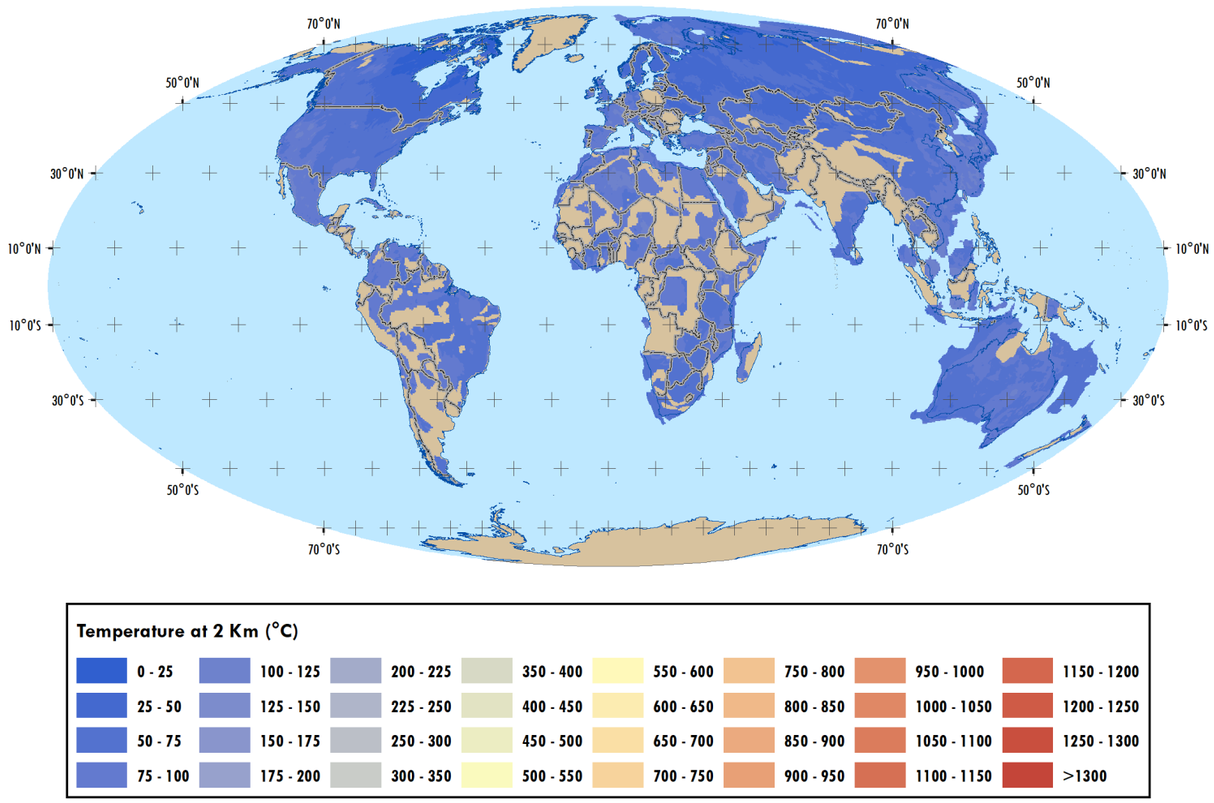

Figure 8.4.1. Temperature at 2 km depth, as predicted from machine learning data

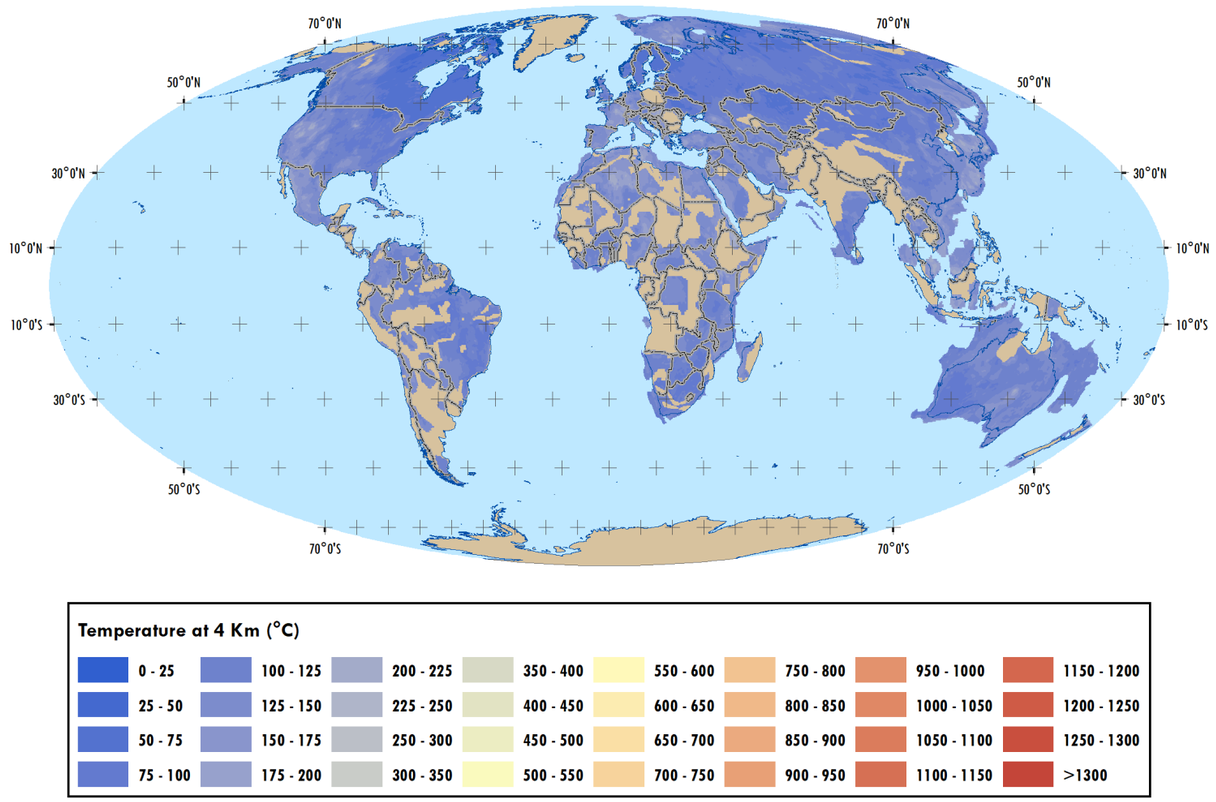

Figure 8.4.2. Temperature at 4km depth, as predicted from machine learning data

Figure 8.4.3. Temperature at 6 km depth, as predicted from machine learning data

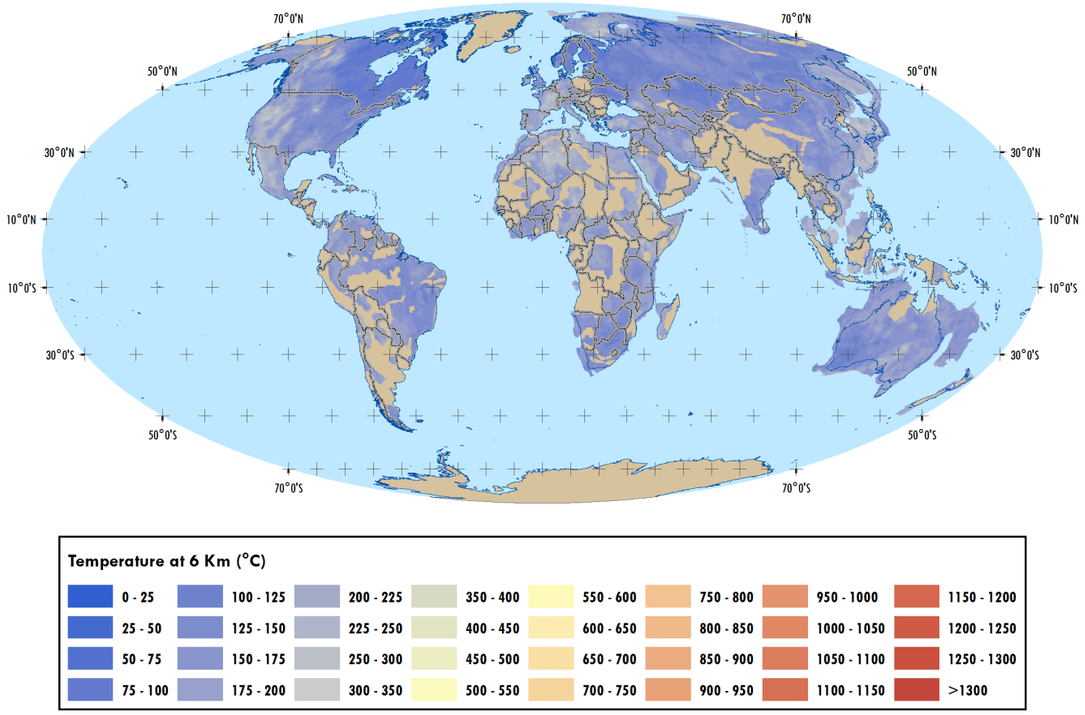

Figure 8.4.4. Temperature at 8 km depth, as predicted from machine learning data

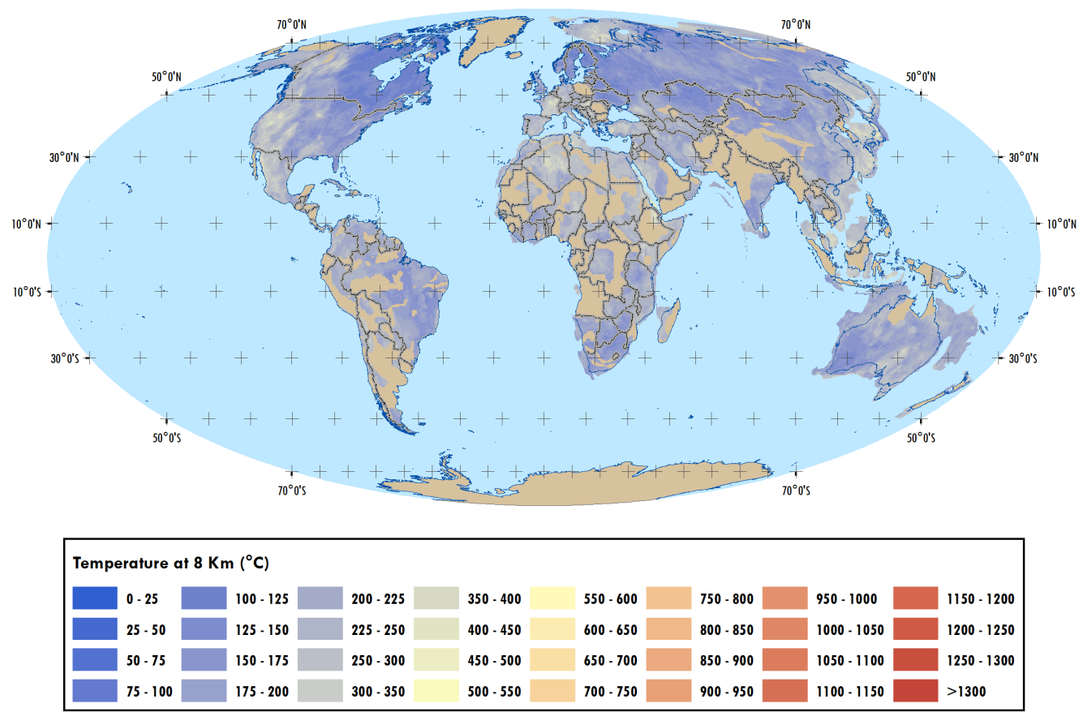

Figure 8.4.5. Temperature at 10 km depth, as predicted from machine learning data

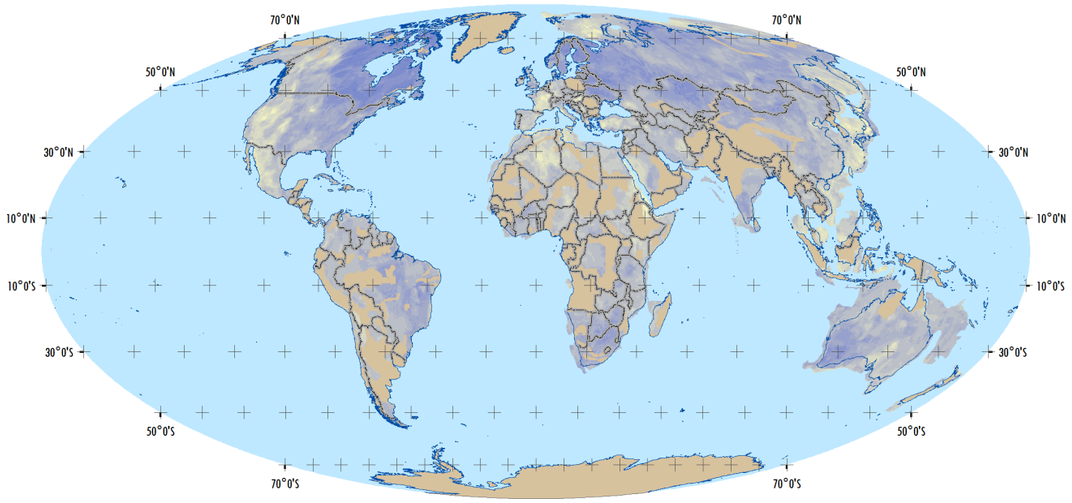

Figure 8.4.6. Temperature at 15 km depth, as predicted from machine learning data

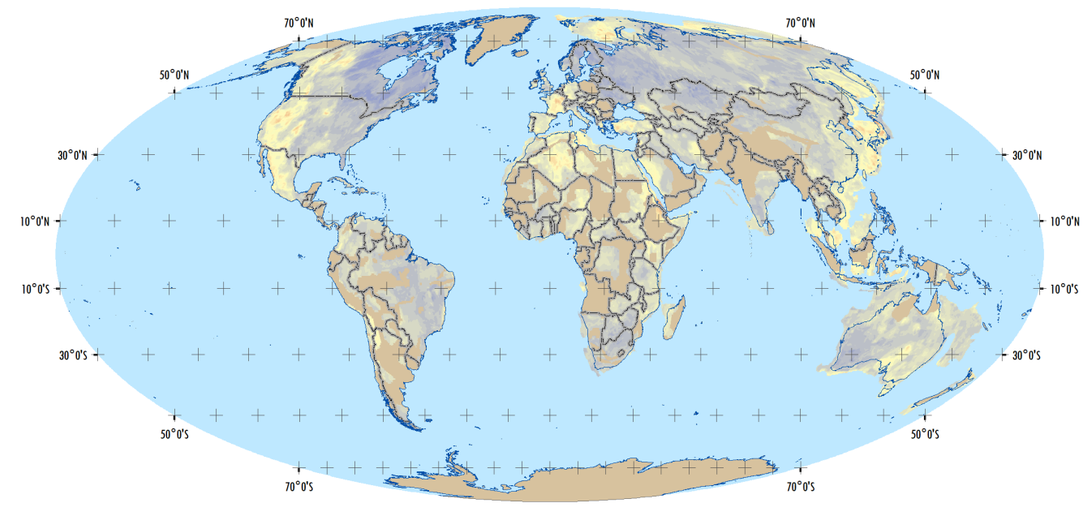

Figure 8.4.7. Temperature at 20 km depth, as predicted from machine learning data

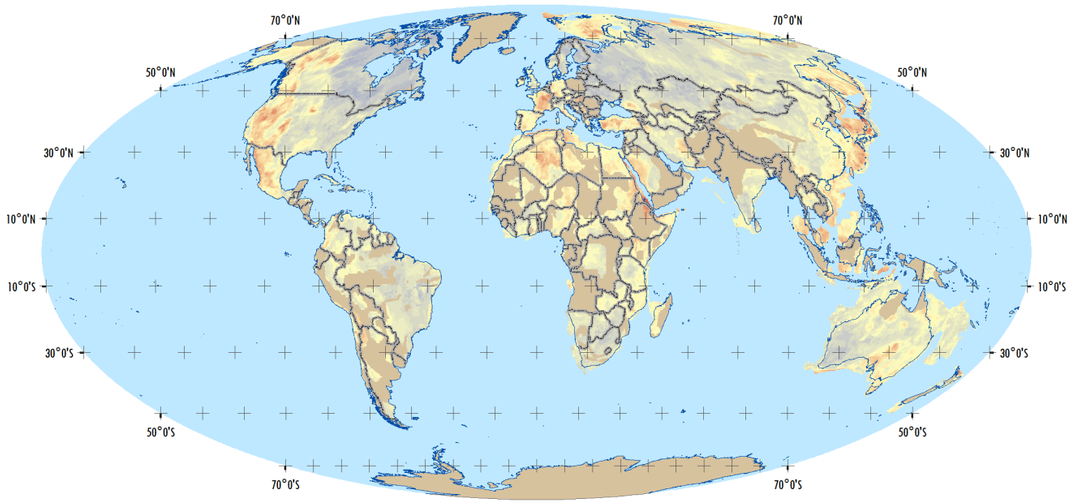

Figure 8.4.8. Temperature at 25 km depth, as predicted from machine learning data

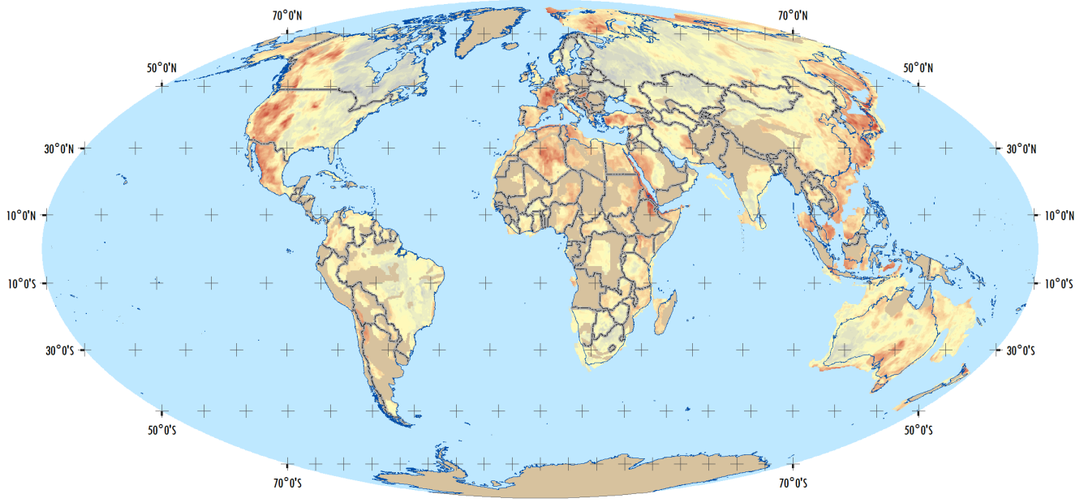

Figure 8.4.9. Temperature at 30 km depth, as predicted from machine learning data

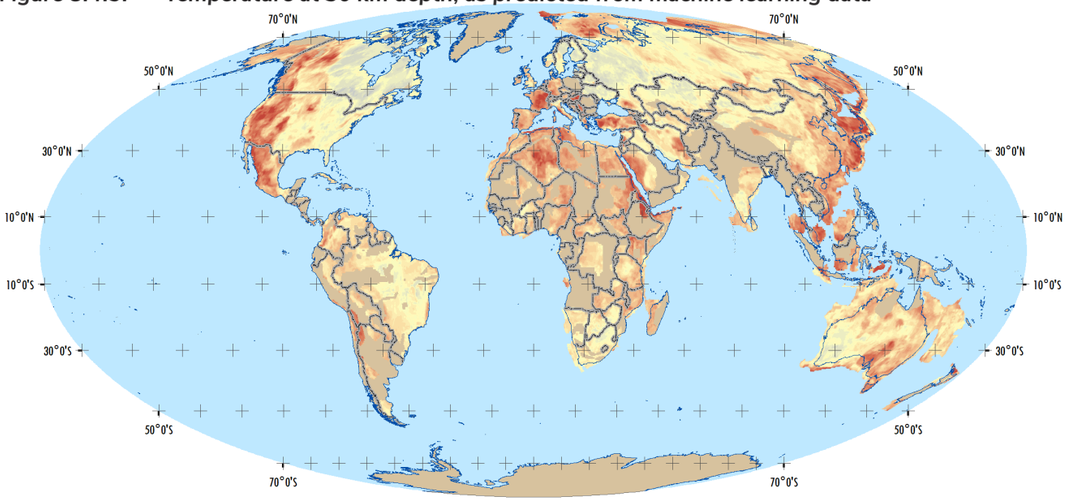

Figure 8.4.10. Temperature at 35 km depth, as predicted from machine learning data

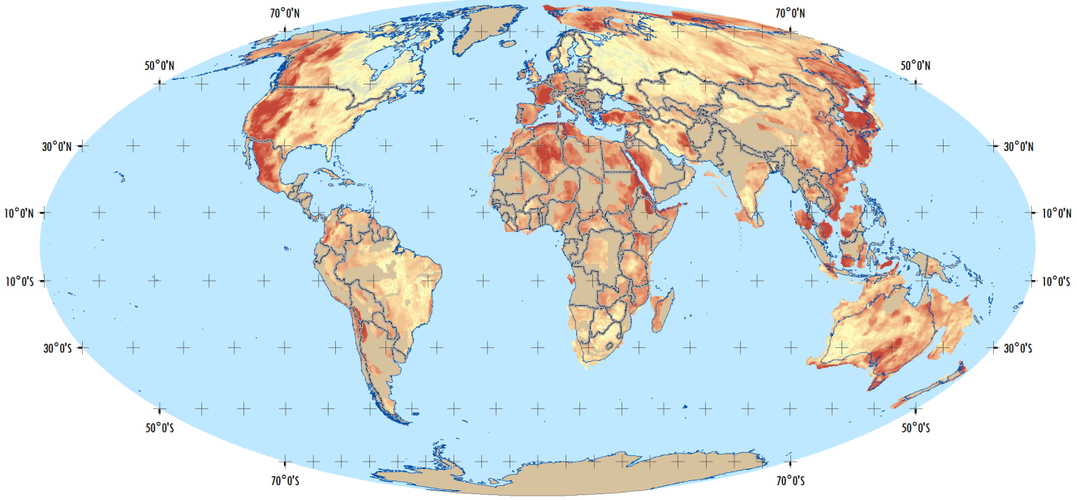

9. Deliverables

The Present Day Thermal Mapping layer collection (Figure 9.1.1) contains the following GIS deliverables:

- Heat flow database
- Interpreted heat flow (Updated, 2021)
- CTD (integrated) (Updated, 2021)
- CTD (heat flow and confidence) (Updated, 2021)
- CTD (terrestrial magnetics and confidence)
- CTD (satellite magnetics)
- CTD (depth sources) (Updated, 2021)
- Temperature-depth grids (Updated, 2021)
- Heat flow & temperature at basement (Updated, 2021) (D2B subscribers)
- CTD (100 km windows)
- CTD (200 km windows)
- CTD (300 km windows)
- Fractal index
- Surface temperature
- Surface heat flow grid (Updated, 2021)
- Heat production (basement) (Updated, 2021)
- Machine Learning data layers (New, 2021):
  - Heat flow training data (points)
  - Global heat flow prediction (points)
  - Regionally compiled heat flow prediction (points)
  - Regionally compiled heat flow prediction (grid)
  - Surface heat flow confidence polygons
  - Heat flow & temperature at basement (D2B subscribers)
  - Temperature-depth grids

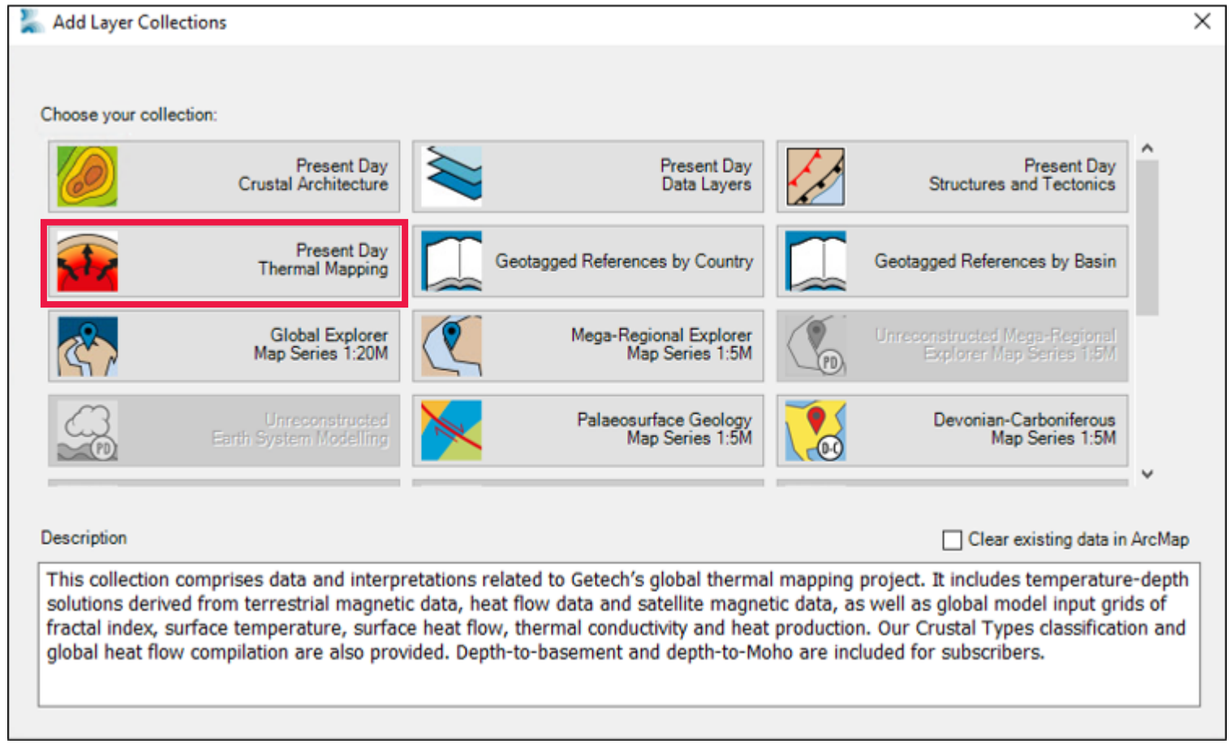

Figure 9.1.1: ***The Present Day Thermal Mapping Layer Collection can be accessed through the Globe Layer Collections toolbar***

10. References

Blakely, R. (1996). Potential Theory in Gravity and Magnetic Applications. Cambridge University Press.

Connard, G., Couch, R. & Gemperle, M. (1983). Analysis of aeromagnetic measurements from the Cascade Range in central Oregon. Geophysics 48 (3), pp. 376-390.

Ferré, E. C., Friedman, S. A., Martín-Hernández, F., Feinberg, J. M., Till, J. L., Ionov, D. A. & Conder, J. A. (2014). Tectonophysics 624-625, pp. 3-14.

Fox Maule, C., Purucker, M. E., Olsen, N. & Mosegaard, K. (2005). Heat Flux Anomalies in Antarctica Revealed by Satellite Magnetic Data. Science 309 (5733), pp. 464-467.

Hamza, V. M. & Vieira, F. P. (2012). Global distribution of the lithosphere-asthenosphere boundary: a new look. Solid Earth 3, pp. 199-212.

Hasterok, D., Chapman, D. S. & Davis, E. E. (2011). Oceanic heat flow: Implications for global heat loss. Earth and Planetary Science Letters 311, pp. 386-395.

Jaupart, C. & Mareschal, J. C. (2011). Heat Generation and Transport in the Earth, Cambridge University Press.Jaupart, C., Mareschal, J. C. & Iarotsky, L. (2016). Radiogenic heat production in the continental crust. Lithos 262, pp. 398-427.

Li, C. F., Lu, Y. & Wang, J. (2017). A global reference model of Curie-point depths based on EMAG2. Scientific Reports 7.

Maus, S. & Haak, V. (2002). Is the Long Wavelength Crustal Magnetic Field dominated by induced or by remanent magnetisation? Journal of Indian Geophysical Union 6 (1), pp. 1-5.

Olsen, N., Ravat, D., Finlay, C. C. & Kother, L. K. (2017). LCS-1: a high-resolution global model of the lithospheric magnetic field derived from CHAMP and Swarm satellite observations. Geophysical Journal International 211 (3), pp. 1461-1477.
Pilkington, M., Gregotski, M. E. & Todoeschuck, J. P. (1994). Using fractal crustal magnetization models in magnetic interpretation. Geophysical Prospecting 42 (6), pp. 677-692.

Salem, A., Green, C., Ravat, D., Singh, K. H., East, P. J., Fairhead, J. D., Mogren, S. & Biegert, E. (2014). Depth to Curie temperature across the central Red Sea from magnetic data using the de-fractal method. Tectonophysics 624-625, pp. 75-86.

Sekiguchi, K. (1984). A method for determining terrestrial heat flow in oil basinal areas. Tectonophysics 103, pp. 67-79.

Spector, A. & Grant, F. S. (1970). Statistical models for interpreting aeromagnetic data. Geophysics 35 (2), pp. 293-302.Stein, C. & Stein, S. (1992). A model for the global variation in oceanic depth and heat flow with lithospheric age. Nature 359, pp. 123-129.

Tanaka, A., Okubo, Y. & Matsubayashi, O. (1999). Curie point depth based on spectrum analysis of the magnetic anomaly data in East and Southeast Asia. Tectonophysics 306 (3-4), pp. 461-470.

Von Herzen, R. P. & Uyeda, S. (1963). Heat flow through the eastern Pacific Ocean floor. Journal of Geophysical Research 68 (14), pp. 4219-4250.

Wasilewski, P. J., Thomas, H. H., Thomas, H. H. & Mayhew, M. A. (1979). The Moho as a magnetic boundary. Geophysical Research Letters 6 (7), pp. 541-544.